Surface Studies of Model Systems relevant for Pd and Ag Catalysts

Martin, Natalia

2014

Citation for published version (APA):
Martin, N. (2014). *Surface Studies of Model Systems relevant for Pd and Ag Catalysts*. Division of Synchrotron Radiation Research, Dept. of Physics, Lund University.

Total number of authors:
1

Surface Studies of Model Systems Relevant for Pd and Ag Catalysts

Natalia Mihaela Martin

Division of Synchrotron Radiation Research

LUND
UNIVERSITY

DOCTORAL DISSERTATION

Front cover illustration:
The PdO(101) surface as a model catalyst

Division of Synchrotron Radiation Research
Department of Physics, Lund University
ISBN: 978-91-7473-860-5
ISB(N+1): 978-91-7473-861-2

Printed in Sweden by Media-Tryck, Lund University
Lund, February 2014

I would like to dedicate this thesis to my loving parents …

Abstract

This PhD thesis reports on investigations of the atomic scale structure of model catalysts relevant for the catalytic oxidation of CO and methane over Pd, and NO_x reduction over silver-alumina, important reactions in automotive catalysts. By using complementary experimental techniques such as X-ray Photoelectron Spectroscopy, High Pressure X-ray Photoelectron Spectroscopy, Surface X-ray Diffraction, Low Energy Electron Diffraction, Infrared Spectroscopy, and Scanning Tunneling Microscopy, combined with theoretical calculations, the work presented in this thesis aims at an atomistic characterization of the active sites for silver-alumina and Pd model catalysts which may help to the design of new and improved catalysts. The results highlight the complexity of the different structures that may form upon oxygen interaction with Ag and Pd single crystal surfaces.

The gas adsorption studies (CO, NO) on clean and oxidized silver surfaces give insights into the chemical properties of the surfaces, information important for the understanding of the reaction mechanism for the NO_x reduction. We have been able to propose models for the adsorption sites for CO and NO on oxidized Ag surface and to propose a model system for the NO_x reduction over silver-alumina.

A particular surface orientation of bulk Pd oxide, the PdO(101) was found to be active for the oxidation of methane. Our studies allow us to reveal the active sites on the surface, information important for the design of better catalysts. Moreover, the results from the CO oxidation over Pd(100) give new insights into the reaction mechanism. The active phase switches between a surface with chemisorbed oxygen to a surface oxide when the oxygen partial pressure is increased.

Populärvetenskaplig Sammanfattning

Katalys är en nyckelteknik inom kemisk industri och spelar en förvånansvärt viktig roll i vårt moderna samhälle. Många av de produkter och kemikalier som används i vårt dagliga liv produceras faktiskt med hjälp av katalysatorer. En annan mycket viktig tillämpning är att avlägsna giftiga ämnen från fordonsavgaser. Det mest fantastiska är att en katalysator snabbar på och förenklar en reaktion utan att själv förbrukas under reaktionen! I heterogen katalys, där reaktanterna är i gasfas och katalysatorn ett fast material, sker reaktionen på ytan av katalysatorn, men förståelsen av denna process på atomär nivå är mycket begränsad. För att öka förståelsen och därmed möjliggöra en mer rationell utveckling av framtida katalysatorer har jag, i den här avhandlingen, undersökt ytstrukturen av katalytiskt aktiva material i kontakt med reaktionsgaser.

Industriella katalysatorer är oftast mycket komplexa materialsystem och består av aktiva metallpartiklar utspridda på en porös metalloxid, vilket gör dem svåra att karakterisera på atomär nivå. Därför skapar man istället modellsystem som är lättare att studera. I den här avhandlingen har vi använt modellsystem bestående av enkristallina katalytiskt aktiva metallytor som med hjälp av yt-känsliga experimentella tekniker kan karakteriseras på en atomär nivå. Speciellt har vi studerat katalytisk oxidering av CH_4 och CO över palladium, och reducering av NO_x över silver-aluminiumoxid på en atomär nivå. Dessa reaktioner är bland de viktigaste i en katalysator i ett modernt fordon.

Vi har undersökt hur silver- och palladiumytor växelverkar med gaser såsom CO, CH_4, NO eller H_2 i en omgivning av höga mängder syre. För detta ändamål har vi använt en kombination av experimentella tekniker och teori och resultaten har gett en ny förståelse för hur dessa gaser växelverkar med dessa ytor. De komplexa syrestrukturer som bildas på palladium och silver vid höga syretryck, visar mycket annorlunda adsorptionsegenskaper än de rena ytorna, information som kan visa sig vara viktig i mer realistiska miljöer. Med hjälp av högupplöst fotoelekronspektroskopi har vi kunnat visa hur dessa gaser adsorberar på den syretäckta silverytan, och föreslår vidare ett modellsystem för att i detalj kunna studera NO_x reducering över silver-aluminiumoxid.

I avhandlingen visas också att en speciell palladiumoxid yta, PdO(101) är mycket aktiv för oxidering av både kolmonoxid och metan. Våra mätningar tillåter oss att avslöja de aktiva sätena på ytan och ny information om reaktionsmekanismen, information som är viktig för utvecklingen av bättre katalysatorer.

Preface

About four years ago I entered the arena of surface science and catalysis with the goal to build a logical understanding of the main catalytic phenomena associated with automobile exhausts catalysis. During my years as a PhD student I have investigated the surface structure of complex catalytic materials and their function at conditions approaching real industrial working conditions of the catalyst and the results are presented in this thesis. The overall aim of my work was an improved understanding of the connections between surface reactivity and structure on the atomic scale. The studies were performed at large scale synchrotron radiation facilities (MAX IV- Sweden, Bessy-Germany, Anka-Germany, ESRF-France, ALS-USA), at the University of Florida and in our home laboratories. The calculations presented in this thesis were performed at the University of Vienna and Chalmers University of Technology.

The thesis starts with an introduction to the research field, some theoretical aspects of reaction kinetics and the methods used. The results are summarized in the following papers, which are included in the second part of the thesis:

I *High-resolution core-level spectroscopy study of the ultrathin aluminum oxide film on NiAl (110),*
N. M. Martin, J. Knudsen, S. Blomberg, J. Gustafson, J. N. Andersen, E. Lundgren, H. Härelind Ingelsten, P.-A. Carlsson, M. Skoglundh, A. Stierle, G. Kresse,
Phys. Rev. B **83**, 125417 (2011)
I planned the experiment, took part in the Photoelectron Spectroscopy measurements, analyzed the data and wrote the manuscript.

II *High-coverage oxygen-induced surface structures on Ag(111),*
N. M. Martin, S. Klacar, H. Grönbeck, J. Knudsen, J. Schnadt, S. Blomberg, J. Gustafson, and E. Lundgren,
submitted (2014)
I planned and took part in the Photoelectron Spectroscopy measurements. I have been responsible for analyzing the spectroscopy data and wrote the manuscript.

III *Mechanism for reversed photoemission core-level shifts of oxidized Ag,*
H. Grönbeck, S. Klacar, **N. M. Martin**, A. Hellman, E. Lundgren, J. N. Andersen,
Phys. Rev. B. **85**, 115445 (2012)
I took part in the Photoelectron Spectroscopy measurements and the discussions about the manuscript.

IV *Carbonate formation on p(4 × 4)-O/Ag(111),*
J. Knudsen, **N. M. Martin**, E. Grånäs, S. Blomberg, J. Gustafson, J. N. Andersen, E. Lundgren, S. Klacar, A. Hellman, H. Grönbeck,
Phys. Rev. B **84**, 115430 (2011)
I took part in the measurements, analyzed part of the data, and took part in the discussion regarding the manuscript.

V *Facile NO_x interconversion over preoxidized Ag(111),*
S. Klacar, **N. M. Martin**, J. Gustafson, S. Blomberg, Z. Liu, S. Axnanda, R. Chang, E. Lundgren, H. Grönbeck,
Surf. Sci. **617**, 167 (2013)
I planned and took part in the Photoelectron Spectroscopy measurements. I have been responsible for analyzing the spectroscopy data and wrote part of the manuscript.

VI *Toward a silver-alumina model system for NO_x reduction catalysis,*
N. M. Martin, E. Erdogan, A. Mikkelsen, H. Grönbeck, J. Gustafson, and E. Lundgren,
in manuscript
I planned the experiment, took part in the measurements, performed the analysis of the results and wrote the manuscript.

VII *Dissociative adsorption of Hydrogen on PdO(101) studied by HRCLS and DFT,*
N. M. Martin, M. Van den Bossche, H. Grönbeck, C. Hakanoglu, J. Gustafson, S. Blomberg, M. A. Arman, A. Antony, R. Rai, A. Asthagiri, J. F. Weaver, and E. Lundgren,
J. Phys. Chem. C, **117 (26)**, 13510 (2013)
I planned and took part in the Photoelectron Spectroscopy measurements, analyzed the spectroscopy data and wrote the manuscript.

VIII *Oxidation and reduction of Pd(100) and aerosol-deposited Pd nanoparticles,*
R Westerström, M. E. Messing, S. Blomberg, A. Hellman, H. Grönbeck, J. Gustafson, **N. M. Martin**, O. Balmes, R. van Rijn, J. N. Andersen, K. Deppert, H. Bluhm, Z. Liu, M. E. Grass, M. Hävecker, E. Lundgren,
Phys. Rev. B. **83**, 115440 (2011)
I participated in the High Pressure X-ray Photoelectron Spectroscopy measurements and in the discussions regarding the results.

IX *CO adsorption on clean and oxidized Pd(111),*
N. M. Martin, M. Van den Bossche, H. Grönbeck, C. Hakanoglu, F. Zhang, T. Li, J. Gustafson,

J. F. Weaver, and E. Lundgren,
J. Phys. Chem. C, **118**, 1118 (2014)
I planned and took part in the Photoelectron Spectroscopy measurements, analyzed the spectroscopy data and wrote the manuscript.

X *Effects of non-local exchange on core-level shifts for gas-phase and adsorbed molecules,*
M. Van den Bossche, **N. M. Martin**, J. Gustafson, C. Hakanoglu, J. F. Weaver, E. Lundgren, H. Grönbeck,
in manuscript
I planned and took part in the Photoelectron Spectroscopy measurements, analyzed the spectroscopy data and participated in the discussions regarding the manuscript.

XI *The active phase of Palladium during methane oxidation,*
A. Hellman, A. Resta, **N. M. Martin**, J. Gustafson, A. Trinichero, P.-A. Carlsson, O. Balmes, R. Felici, R. van Rijn, J. W. M. Frenken, J. N. Andersen, E. Lundgren, H. Grönbeck,
J. Phys. Chem. Lett. **3**, 678 (2012)
I took part in the Surface X-ray Diffraction measurements and took part in the discussions regarding the results.

XII *Oxide thickness dependent ligand effect,*
N. M. Martin, M. Van den Bossche, A. Hellman, H. Grönbeck, C. Hakanoglu, J. Gustafson, S. Blomberg, N. Johanson, Z. Liu, S. Axnanda, J. F. Weaver, and E. Lundgren,
submitted (2014)
I planned the experiment, took part in the measurements, analyzed the spectroscopy data and wrote the manuscript.

XIII *In situ X-ray Photoelectron Spectroscopy of model catalysts: At the edge of the gap,*
S. Blomberg, M. J. Hoffmann, J. Gustafson, **N. M. Martin**, V. R. Fernandes, A. Borg, Z. Liu, R. Chang, S. Matera, K. Reuter, and E. Lundgren,
Phys. Rev. Lett. **110**, 117601 (2013)
I participated in the High Pressure X-ray Photoelectron Spectroscopy measurements and in the discussions regarding the results.

Papers that I have contributed to and are not included in this thesis:

XIV *Stable cation inversion at the $MgAl_2O_4$(100) surface,*
M. R. Rasmussen, A. S. Foster, B. Hinnemann, F. F. Canova, S. Helveg, K. Meinander, **N. M. Martin**, J. Knudsen, A. Vlad, E. Lundgren, A. Stierle, F. Basenbacher, J. V. Lauritsen,
Phys. Rev. Lett. **107**, 036102 (2011)

XV *Structure of the Rh_2O_3(0001) surface,*
S. Blomberg, E. Lundgren, R. Westerström, E. Erdogan, **N. M. Martin**, A. Mikkelsen, J. N. Andersen, F. Mittendorfer and J. Gustafson,
Surf. Sci. **606**, 1416 (2012)

XVI *Generation and oxidation of aerosol deposited PdAg nanoparticles,*
S. Blomberg, J. Gustafson, **N. M. Martin**, M. E. Messing, K. Deppert, Z. Liu, R. Chang, V. Fernandes, A. Borg, H. Grönbeck, E. Lundgren,
Surf. Sci. **616**, 13510 (2013)

XVII *A High Pressure X-ray Photoelectron Spectroscopy study of CO oxidation over Rh(100),*
J. Gustafson, S. Blomberg, **N. M. Martin**, V. Fernandes, A. Borg, Z. Liu, R. Chang, E. Lundgren,
J. Phys.: Condens. Matter **26**, 055003 (2014)

Contents

1

Introduction

1.1 Background and research motivation

Catalysis is a key technology in chemical industry and plays a vital role in our modern society. Most of the products and chemicals used in our daily life are produced by the use of catalysis at one stage or another. Catalysts are widely used in the pharmaceutical industry, in the production of fuels and plastics and in solving air and water pollution problems [1]. As almost every aspect of modern living is dependent on catalysis, this subject is well worth studying and understanding [2, 3] and therefore a significant amount of research is devoted to improve catalysts.

The birth of the field of catalysis took place in 1836, when J. J. Berzelius defined the phenomenon of catalysis in order to explain different transformation reactions [4]. Some years later, in 1895, W. Ostwald proposed a definition for a catalytic material (Nobel Prize 1909) that is still valid today: *"A catalyst is a substance, which affects the rate of a chemical reaction without being part of its end products."* [5] During the reaction, the catalyst forms bonds with the reactants, which may result in intermediate species to form and react, at a much lower energy cost than in the absence of a catalyst. This is schematically illustrated in Fig. 1.1. By introducing a catalyst, the energy barrier between reactants and products is reduced by providing an alternative reaction path consisting of steps with lower activation energy than for the uncatalyzed reaction. This will be discussed further in Chapter 5.

One of the first applications of catalysis was the synthesis of ammonia (NH_3), an important ingredient for making fertilizers, realized in 1909 by F. Haber (Nobel Prize 1919) using an osmium catalyst [6]. Later, C. Bosch (Nobel Prize 1931) transformed the process to industrial scale producing the first plant in 1913. The technology has later been applied worldwide using iron or copper catalysts, which enabled engineers to carry out the reactions at more ambient temperatures. During the 20th century catalysis has been the subject of extensive research, new techniques allowing insights into the atomic scale properties of different surfaces have been developed, enabling scientists to move a step further towards understanding catalysis on the atomic scale [7]. It became possible to study the catalytic mechanisms when the Langmuir-Hinshelwood kinetics became available in the mid 1920s. The devel-

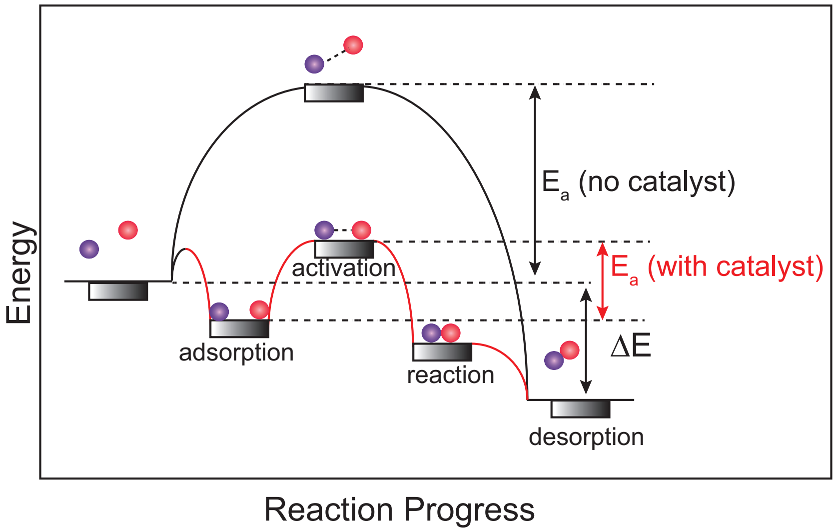

Figure 1.1: Comparison of the activation energy barriers of an uncatalyzed reaction and the same reaction with a catalyst. A substantial energy barrier has to be overcome in the uncatalyzed reaction and, therefore, has a slower rate. The catalyst lowers the energy barrier but does not affect the actual energies of the reactants or products.

opment of the surface science field and vacuum technology in the second half of the 20th century has contributed significantly to our understanding of catalysis. A recent Nobel Prize in Chemistry to surface scientist Gerhard Ertl (2007) in the field of catalysis emphasizes the importance of surface science research in this field [8]. Aside from the experimental methods, theoretical studies utilizing density functional theory (DFT) calculations have also contributed to a better understanding of the reaction mechanisms on different surfaces.

Catalysis can be divided into two categories: homogeneous and heterogeneous catalysis. This thesis deals with heterogeneous catalysis, where the reactants and the catalyst are in different phases. Usually the catalyst is a solid and the reactants are either gases or liquids [9]. Many industrially important reactions are catalyzed by the surfaces of solids. Heterogeneous catalysts are often composed of metals and metal oxides. The initial step in heterogeneous catalysis is usually the adsorption of reactants. The steps involved during a catalytic reaction will be described in Chapters 4 and 5.

One important application of heterogeneous catalysis concerns protection of the environment through removal of toxic substances from automotive exhaust. A good example is the catalytic converter found in the car exhaust gas systems. Most modern cars are equipped with a catalytic converter removing most of the toxic exhaust gases from the processes in a combustion engine. Its function is to reduce harmful emissions from entering the atmosphere. Due to incomplete combustion, the exhaust gas contains a mixture of different gases such as CO and unburned hydrocarbons, together with NO_x, which are harmful to the environment. The catalytic converter used in most combustion gasoline engines is the so-called Three Way Catalyst (TWC) [10, 11] introduced in the 1970s. It consists of noble metal particles (Pt, Rh, Pd) supported on a ceramic monolith and is able to reduce the emissions of NO_x, CO and unburned hydrocarbons (HC) with high efficiency.

Surprisingly, many catalysts used today are designed by a trial-and-error approach. This is because many of the catalytic processes are not understood on a fundamental level, motivating an impressive amount of work in this field in the last decades. Despite these efforts, many essential questions about catalytic reactions remain unanswered. An atomic scale understanding of the reaction mechanisms is needed for the design of better catalysts that can keep up with our developing world. The work presented in this thesis aims at understanding a part of the fascinating and indispensable phenomenon of catalysis and answering some questions related to the activity and the active phase.

1.2 This work

The aim of the work presented in this thesis is to generate fundamental atomic scale insights of the catalytic oxidation of CH_4 and CO over Pd, as well as NO_x reduction over silver-alumina, among the most important reactions in automotive catalysts. This thesis is structured as the following: the thesis starts with an introduction to the surface science approach to catalysis (Chapter 2) and the structure of surfaces (Chapter 3). Then, concepts of gas-surface interaction such as adsorption of gases, chemisorption, the *d*-band model and chemical reactions are presented in Chapters 4 and 5. The description of the experimental techniques used in this work is presented in Chapter 6 and the results are summarized in Chapter 7 and presented in Papers I to XIII.

In the first part of the results presented in the present thesis (Papers I-VI) we have initiated a study to understand the silver-alumina model catalyst used for lean NO_x reduction. In order to reduce fuel consumption and thereby CO_2 production, it is desirable to use diesel and lean-burn engines with a high air-to-fuel ratio. The TWC has a disadvantage, though, namely that it can only efficiently reduce NO_x, while oxidizing CO and HC simultaneously, in a very narrow air-to-fuel ratio. Using lean-burn and diesel engines, the air-to-fuel ratio is too high for the TWC to efficiently reduce NO_x. The CO and unburned HC found in the exhausts of engines running at stoichiometric conditions are needed to reduce NO_x over the TWC [12], but the high oxygen content in the lean-burn exhaust may also form inactive oxides [13]. Therefore, a different approach to reduce NO_x in oxygen excess atmosphere is needed. Among other material systems, it has been observed that a catalyst based on aluminum oxide impregnated with Ag is effective in reducing NO_x [14, 15] when using an additional hydrocarbon, such as ethylene as a reducing agent. The exact structure of this catalyst is unknown, and the role of the Ag is not clear. However, owing to the presence of oxygen during the lean NO_x reduction, it is not unlikely that the Ag is highly coordinated to oxygen or even oxidized. The starting point in understanding the silver-alumina catalyst was to investigate the role of the Ag in the catalyst. We have studied the oxidation of a silver single crystal surface and showed that a set of different oxygen-induced surface structures may form. Moreover, the interaction of silver oxide with CO and NO was also investigated. In this way we have been able to propose models for the adsorption sites of CO and NO on an oxidized Ag surface, information important for the understanding of the reaction pathway of the catalytic reduction of NO_x to N_2. Furthermore, we have studied the structure of the aluminum oxide film grown on NiAl(110) (γ-alumina) that serves as a model support for the bulk alumina and have developed a model system for facilitating studies of NO_x reduction over silver-alumina.

The second half of the thesis focuses on the understanding of Pd catalysts used for methane and CO oxidation reactions (Papers VII-XIII). Methane is the main component in natural gas with the highest hydrogen-to-carbon ratio and therefore containing a high amount of energy. It is used in natural-gas engines for automotives, and it is expected that the use of methane fueled engines will increase in the nearby future. The exhaust gases from natural-gas (methane) engines contain hydrocarbons consisting mostly of unburned methane. Since this gas is a significant greenhouse gas (a greenhouse factor of 20 compared to CO_2), it is important to remove it from the exhaust gas using a catalyst. Palladium is known to be an important catalyst for the cleaning of automotive exhausts as well as in methane combustion. At the moment very little work is available for natural-gas engine exhaust which contains excess oxygen. It is however believed that Pd is even more active for methane oxidation at excess oxygen when a bulk-like Pd oxide may form. The aim of this work was to understand how methane is oxidized using Pd as a catalyst under realistic conditions. As previous work suggested a bulk-like PdO as responsible for the increased activity of this catalyst, we have studied the oxidation of Pd in ultra-high vacuum conditions following the preparations methods described in the literature to produce a high quality Pd oxide film (Paper VII). The gas adsorption measurements (Papers VII-IX) on the PdO film confirmed the assignment of the undercoordinated metal atoms at the surface of the oxide and therefore we concluded that the PdO film grown on Pd(100) and Pd(111) exposes the (101) orientation. Armed with this information we have studied the methane oxidation over Pd using high pressure X-ray Photoelectron Spectroscopy and Surface X-ray Diffraction. The measurements strongly suggest that there is an increased methane oxidation over Pd when PdO(101) is formed and that the reaction proceeds over the 3-fold coordinated Pd atoms at the surface of the oxide (Papers XI-XII). This information is a key for an atomic-scale understanding of the methane interaction and oxidation over Pd in an oxygen rich environment in close to realistic environments.

2

The Surface Science Approach to Catalysis

The aim of the surface science approach to catalysis is to obtain an atomic level understanding of the catalyst and preferably to pinpoint the location of the active sites on the surface [16]. An industrial catalyst consists of active metal nanoparticles dispersed on an oxide support to maximize the surface area and to reduce the amount of catalyst needed. Atomic scale surface characterization of this kind of systems, under working conditions, is very difficult, if not impossible. Thus, our ability to relate the observed effects in reactivity to the atomic scale is limited and attention has been turned into studying simplified systems as already suggested by I. Langmuir in 1922 (Nobel Prize 1932): *"In order to simplify our theoretical consideration of reactions at surfaces, let us confine our attention to reactions on plane surfaces. If the principles in this case are well understood, it should then be possible to extend the theory to the case of porous bodies"* [17].

Since then, scientists have made considerable progress in understanding the catalytic reaction mechanisms by studying metal single crystal surfaces in ultra-high vacuum (UHV) conditions [18, 19, 20, 21, 22, 23, 24, 25, 26, 27, 28, 29, 30] culminating with the Nobel Prize in Chemistry awarded to Gerhard Ertl in 2007 for his ground-breaking surface science studies of catalysts [8]. To emphasize the importance of the surface science approach to catalysis, the mechanism of some catalytic reactions has been elucidated from UHV measurements as for example ammonia synthesis [31].

2.1 Single crystal surfaces as model catalysts

Model catalysts are systems that are easier to study than real catalysts and they can be used to correlate the observed activity effects to particular sites on the surface. The model catalysts traditionally studied in surface science, and in the present work, consist of well-ordered single crystal surfaces of catalytic materials that are prepared under UHV. The surface structure of the materials used in this work will be presented in more detail in Chapter 3. Using surface science techniques the atomic structure, electronic and chemical properties can be investigated. Then the reaction on model catalysts can be compared to reactions on more realistic catalysts [32].

2.2 Pressure and materials gap

Although several studies have reported a good agreement, the UHV methodology used in surface science differs from the real world catalysis, with elevated pressures and high surface area materials introducing the so-called pressure and materials gaps between applied catalysis and the surface science community [8]. The pressure gap refers to the difference in pressure between the UHV surface science experiments ($P < 10^{-6}$ mbar) and the atmospheric or elevated pressure at which real catalysts operate (up to 100 bar), while the materials gap refers to the structural difference between the single crystal model catalysts and the metal nanoparticles dispersed on an oxide support in a real catalyst.

During the last years significant research has been conducted to close these gaps. Recently, new developments in experimental techniques capable of *in situ* studies under elevated pressure conditions have been added to the arsenal of surface science techniques [29, 33, 34, 35, 36, 37, 38, 39]. In this thesis techniques such as Surface X-ray Diffraction and high-pressure X-ray Photoelectron Spectroscopy have been used to investigate the NO_x reduction, CO and methane oxidation reactions under conditions closer to real application conditions as reported in Papers V, VIII, XI-XIII. Increasing the complexity of the model systems, for example by growing the active catalyst material as nanoclusters on a specific facet of a relevant metal oxide support [40, 41, 42, 43], is one way to bridge the materials gap. In the work presented in this study the complexity of the model systems investigated was gradually increased from single crystals to dispersed metal nanoparticles on oxide support (Papers VI, VIII).

3

Surface Structures

One of the major properties of the catalyst is the surface structure [44]. Therefore, understanding the basics of surface structure is essential to understand catalysis. A surface can be defined as an abrupt termination of the bulk where the atoms do not have neighboring atoms in the direction out of the surface. This undercoordination results in free bonds at the surface that are available for interaction with incoming molecules. Most surfaces consist of a mixture of flat regions and defects, with a different local distribution of atoms at each of these surface sites.

3.1 Crystal structure

In order to study surfaces, the basics of crystal structure must first be understood. A crystal consists of atoms arranged in a pattern that repeats periodically in three dimensions. The smallest unit from which the whole crystal can be constructed by translational displacements is called the primitive unit cell [45]. A crystal, inside which all unit cells are aligned with the same orientation is called a single crystal. A material which consists of crystallites with different orientations is called polycrystalline. In this thesis single crystal surfaces were mostly studied and the focus will therefore be on the geometry of single crystals.

To describe crystalline solids, the position of each atom in the unit cell needs to be specified. This is usually referred to as the basis. Most metals can be described by a cubic unit cell (see Fig. 3.1). By placing an atom at each corner of the cube the simple cubic (*sc*) structure is obtained. Adding an atom in the center of the cube will result in the body centered cubic unit cell (*bcc*) and by placing an atom at the center of each face of the cube will result in the face centered cubic unit cell (*fcc*). Relevant for this thesis are the *fcc* and *bcc* lattices, described in the next section.

A single crystal is grown from a molten metal and by cutting its surface along a desired orientation the surface is created. Laue X-ray diffraction is used to check for accuracy of the orientation and the surface is later mechanically polished. Generally, it is difficult to cut a crystal to exactly the required surface and therefore the surface usually presents steps relating to the angle of the cut ($\approx 0.5^\circ$ off the indicated plane). Different single crystal surfaces

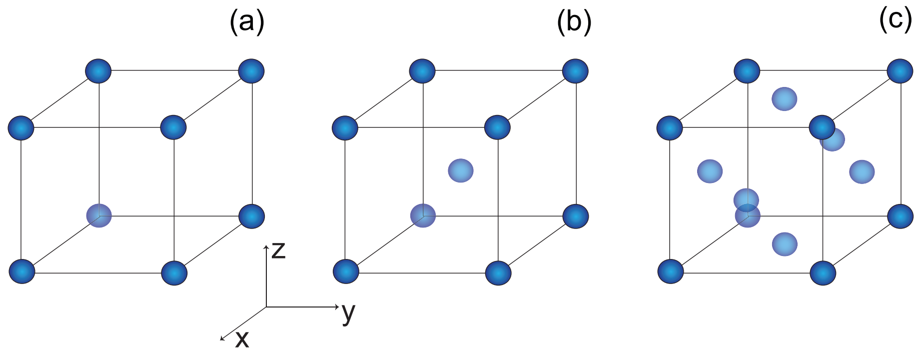

Figure 3.1: Crystal unit cells. a) Simple cubic (*sc*), b) body centered cubic (*bcc*), c) face centered cubic (*fcc*). The atoms are represented by the blue spheres.

were used in this thesis, NiAl(110), Ag(111), Pd(111) and Pd(100) and their surface structure can be described by the *bcc* (NiAl) and *fcc* (Ag, Pd) lattices, respectively.

3.2 Surfaces

As surfaces with certain orientations have been studied in this work, it is important to distinguish between different surface orientations. This is done by using the so-called Miller indices, which is a way to describe planes within a unit cell of a crystal. If these planes are extended within the crystal they will include atoms arranged in a periodic fashion. These planes are defined by their intersection points with the coordinate system but written as reciprocal values (the inverse distance from the origin to the intersection). For cubic structures, these Miller indices are also referred to as *(hkl)*. The notation *[hkl]* denotes the vector perpendicular to the *(hkl)* surface. If the Miller indices are 0 or 1 the planes are called low index planes.

In this thesis the low index surface orientations of Pd, Ag (both described by a *fcc* lattice) and NiAl (described by a *bcc* lattice) single crystal surfaces are studied in more detail. Fig. 3.2 and Fig. 3.3 show the structures of the (100), (110) and (111) surfaces for the *fcc* and *bcc* structures, respectively. The coordination of the atoms in each of these surface planes is different. The (100) surface forms a squared periodicity on the surface, while a hexagonal periodicity is observed for the (111) plane. For a *fcc* lattice (see Fig. 3.2) each atom in the surface plane has 6 neighbors for the most closed packed (111) surface, 4 for the (100) and only 2 neighbors for the (110) surface. Coordination has a significant effect on the reactivity as surfaces with lower coordination atoms have the highest surface free energy (see Section 3.5) and from a thermodynamic point of view there will be a tendency to minimize this energy by bonding with other molecules. This is also important for the equilibrium shape of nanoparticles which, according to Wulff construction (section 3.6.2), expose the common low surface-energy facets.

3.2.1 Clean surfaces

The cleanliness and chemical composition of surfaces can be determined experimentally using surface science techniques described in Chapter 6. In Fig. 3.4 the Low Energy Electron Diffraction (LEED) patterns and X-ray Photoelectron spectra from the clean Ag(111), NiAl(110), and Pd(100), some of the single crystal surfaces used in the present work, are presented.

Ag is a noble metal crystallizing in the *fcc* structure with a lattice constant of a=4.0853 Å and a melting temperature of almost 1235 K [46]. The electronic configuration for Ag is $4d^{10}s^1$. The (111) surface is a so-called "closed packed" surface. The surface unit cell is hexagonal, with an atomic distance of $a/\sqrt{2}$=2.88 Å as illustrated by the LEED pattern shown in Fig. 3.4 (a). The Ag $3d_{5/2}$ spectrum recorded at normal emission with a photon energy of 430 eV shows a single peak at a binding energy of 368.16 eV corresponding to bulk Ag.

The NiAl(110) surface serves as a substrate on which an aluminum oxide film may be grown. NiAl is one of several ordered nickel-aluminum alloys [47]. It has a *bcc* structure with Ni atoms at the corners of the cube and an Al atoms in the center, similar to CsCl with a lattice constant a=2.89 Å and high melting point of 1911 K. The high melting point of the alloy allows for high preparation temperatures. The (110) surface has a rectangular unit cell with sides of $a\sqrt{2}$=4.08 Å and a, respectively as illustrated in Fig. 3.3 (b). The LEED pattern in Fig. 3.4 (b) shows a rectangular lattice. The Al $2p$ X-ray Photoelectron spectrum is decomposed using 2 components that are each split into two peaks separated by 0.4 eV due to the spin-orbit splitting and with an intensity ratio of 1:2. The blue component is assigned to Al atoms in the bulk of the NiAl and the red component shifted 0.1 eV towards lower binding energy to the surface Al atoms [48]. Similar shift has been observed for some other alloy systems [49, 50].

Pd is a transition metal crystallizing in the *fcc* structure with a lattice constant a=3.89 Å [51] and a melting point of 1828 K. In the (100) orientation, the surface unit cell (see Fig. 3.2 (c)) is squared with a lattice constant of $a/\sqrt{2}$=2.75 Å. The LEED pattern in Fig. 3.4 (c) shows a squared (1 × 1) lattice. The Pd $3d$ spectrum shows a bulk Pd component at about 335 eV (black) and a surface component (shifted -0.3 eV with respect to bulk Pd) from the Pd atoms located in the surface layer (brown).

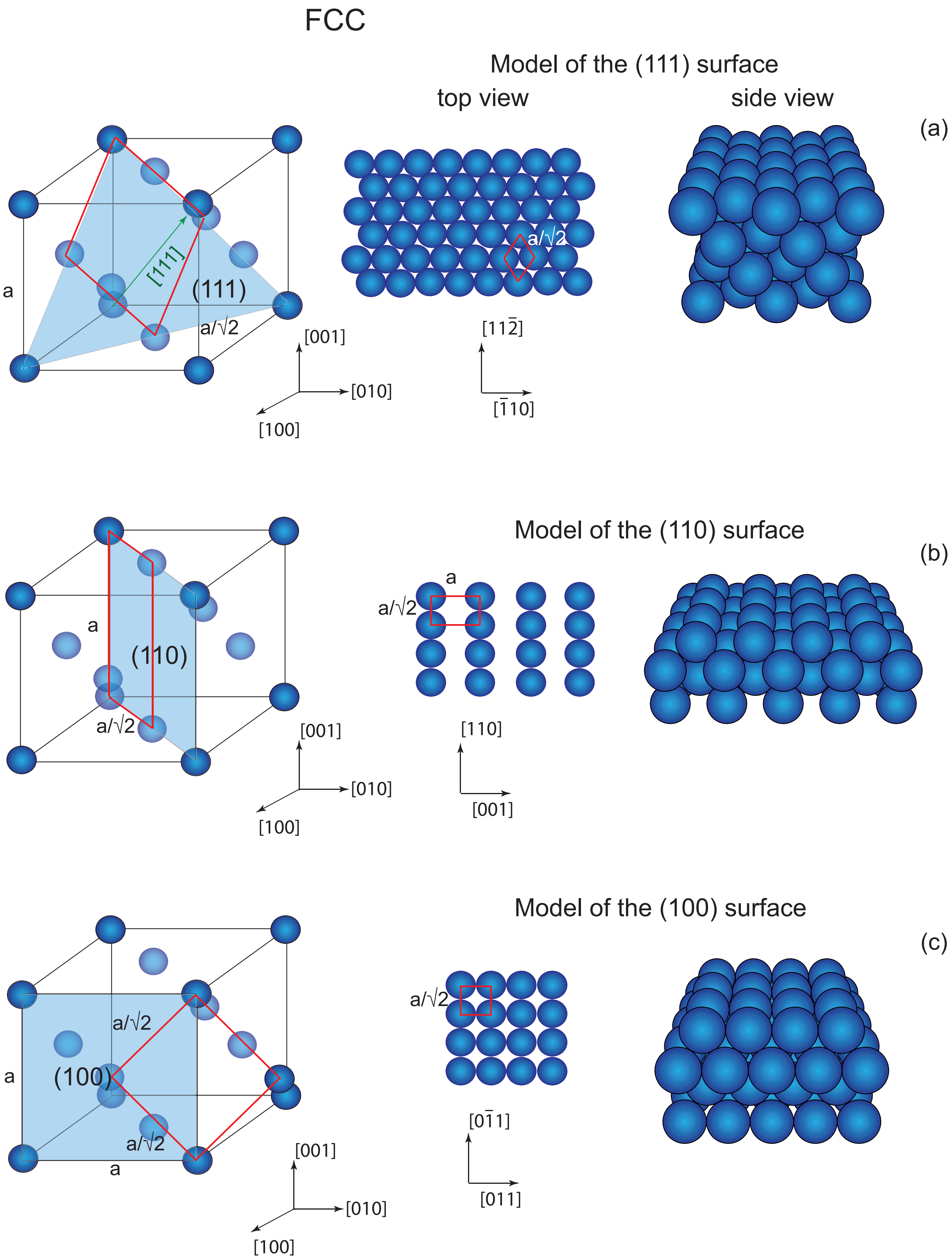

Figure 3.2: The unit cell and the low index (111), (110) and (100) planes ((a),(b) and (c)) with the corresponding cut surfaces for a *fcc* lattice.

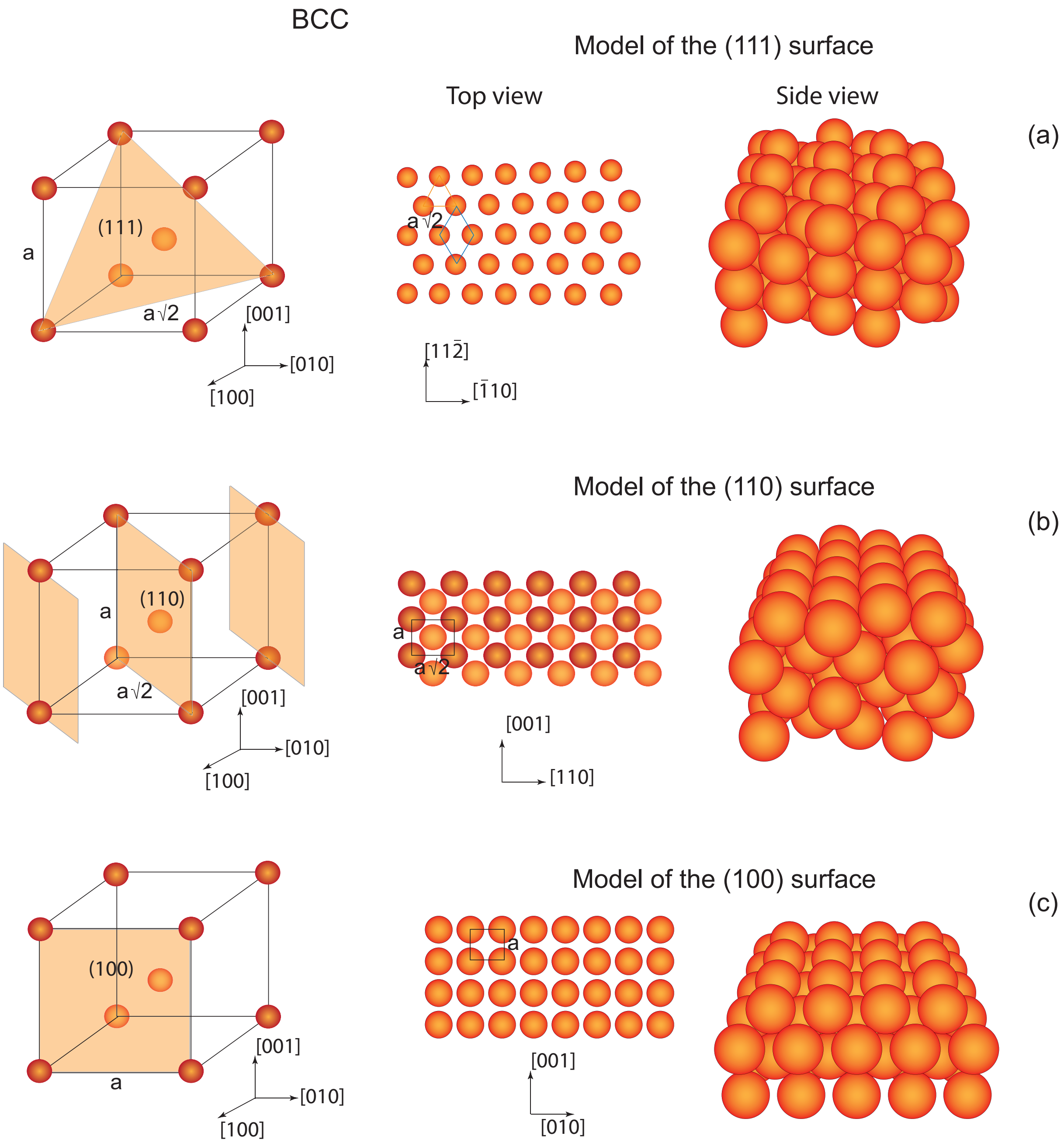

Figure 3.3: The unit cell and the low index (111), (110) and (100) planes ((a),(b) and (c)) with the corresponding cut surfaces for a *bcc* lattice.

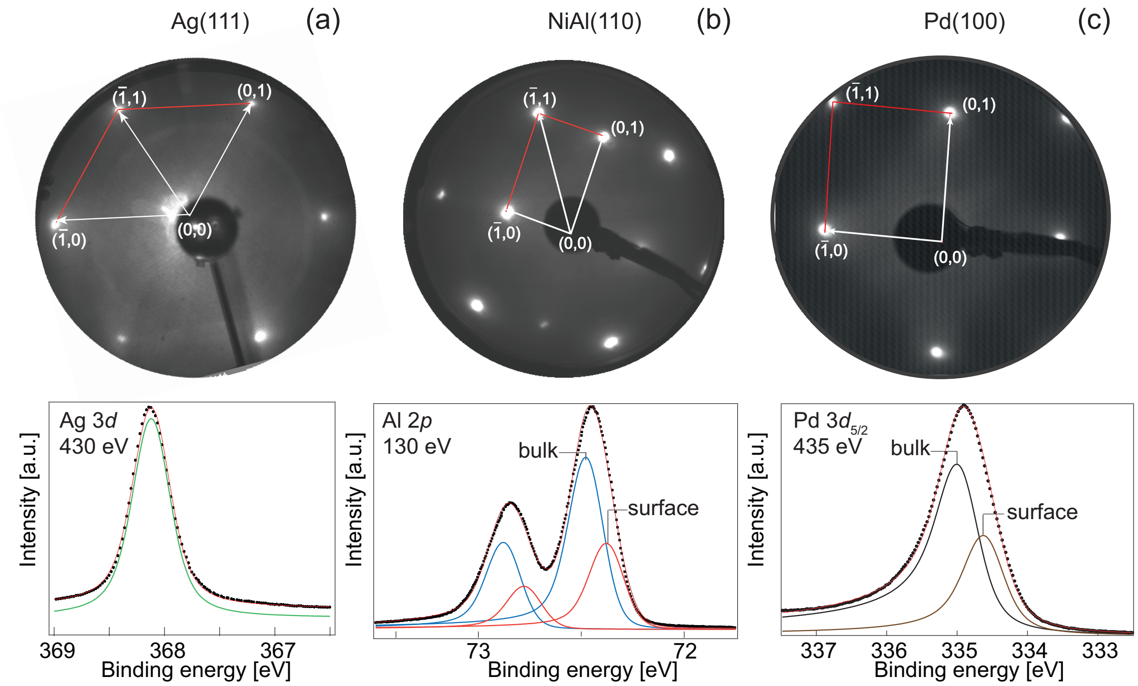

Figure 3.4: The LEED patterns and the corresponding X-ray Photoelectron spectra from the clean (a) Ag(111), (b) NiAl(110) and (c) Pd(100) samples. The electron and photon energies used were: (a) 120 eV, 430 eV, (b) 60 eV, 130 eV, (c) 60 eV and 435 eV, respectively.

3.3 Surface reconstructions

Because of the missing neighbors in the direction out of the surface, a surface exhibits different properties as compared to the bulk of a crystal. For many surfaces, a rearrangement of the atoms can occur in order to minimize the surface energy [52]. Two kinds of rearrangements may occur when surfaces are created: relaxations and surface reconstructions.

Relaxation refers to a small rearrangement of the surface layers but with no changes in the periodicity parallel to the surface or in the symmetry of the surface. The reconstruction of surfaces, on the other hand, involve a change in the periodicity of the surface structure and even a change in surface symmetry, with large displacements of the surface atoms. Most often a new surface unit cell, different from the bulk unit cell, is formed. The clean surfaces used in this thesis (Pd(111), Pd(100), Ag(111), NiAl(110)) do not reconstruct in UHV conditions.

3.3.1 Adsorbate-induced reconstructions

The adsorption of atoms or molecules on a surface leads to the formation of bonds between the adsorbate and the substrate (see Chapter 4). The most common on-surface adsorption

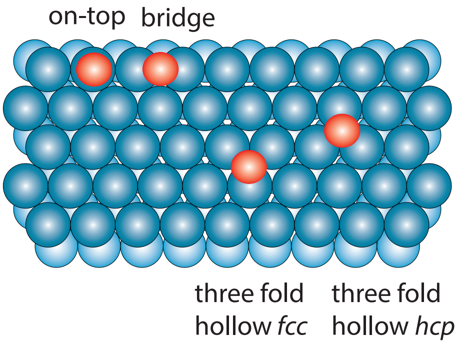

Figure 3.5: Possible adsorption sites on a hexagonal lattice: on-top, bridge and three-fold hollow.

sites on a hexagonal lattice are shown in Fig. 3.5. The difference between the *fcc* and *hcp* sites is that in the former case the adsorbate molecule is located above a metal atom of the third layer, while it is located above the metal atom of the second layer for the latter case. A useful notion when describing adsorbate structures is the coverage. Usually the coverage is expressed in MonoLayers (ML), where 1 ML corresponds to the number of substrate atoms in the surface layer.

In order to minimize the surface energy, the adsorbate will often arrange in well-ordered structures. Adsorbate structures are described in relation to the unit cell of the substrate. This is done by using the Woods notation (see Fig. 3.6), which is a way of describing ordered surface structures as reconstructions or adsorbate arrangements. The unit cell of the adsorbed gas molecule, defined by the two vectors $\mathbf{b}_1$ and $\mathbf{b}_2$, is usually referred to the units of the bulk terminated surface of the substrate [53, 54]. Wood's notation first involves specifying the lengths of the two overlayer vectors, $\mathbf{b}_1$ and $\mathbf{b}_2$, in terms of the surface vectors $\mathbf{a}_1$ and $\mathbf{a}_2$, respectively. This is then written in the format :

$$c/p(\frac{b_1}{a_1} \times \frac{b_2}{a_2})R\theta - X, \tag{3.1}$$

where c, p denotes centered or primitive cell, a, b are the unit vectors, θ is the angle of rotation between the adsorbate and the substrate lattices, and X represents the adsorbed molecule.

Fig. 3.6 shows different adsorbate structures of CO adsorption on a clean Pd(111) surface for different CO coverages. The initial exposure of Pd(111) to CO results in the formation of $(\sqrt{3} \times \sqrt{3})R30°$ and $c(4 \times 2)$-2CO structures with coverages of 0.33 and 0.5 ML, respectively, while at higher coverages a (2×2)-3CO structure can form with CO occupying the 3-fold hollow, bridge and atop sites [55]. The $c(4 \times 2)$-2CO structure is further discussed in Paper IX.

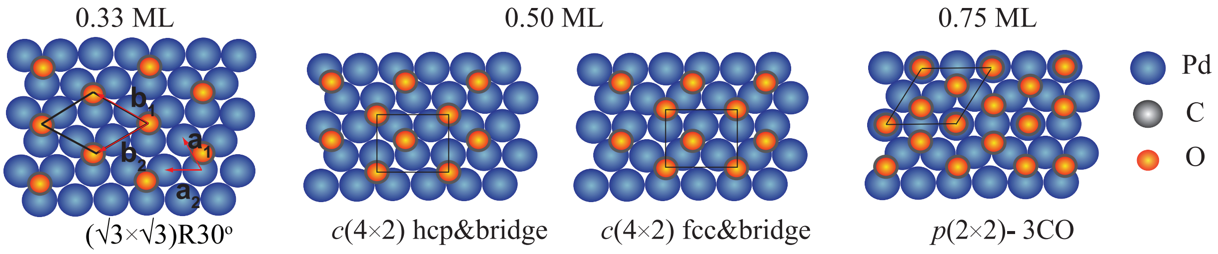

Figure 3.6: Wood's notation for different adsorbate structures formed upon CO adsorption on Pd(111).

Adsorption of gases on a metal surface may also be accompanied by a reconstruction of the surface atoms. For instance, the O_2 adsorption is usually dissociative and most often, at higher oxygen pressures, the surfaces tend to reconstruct forming different oxide structures.

3.4 Oxidation

Metals are generally unstable when exposed to an oxidative environment and most of them are forming metal oxides. In general, the oxidation can be defined as the reaction between a metal and oxygen atoms, with the oxygen atoms mixing with the metal atoms forming a new compound. In an initial stage of oxygen interaction with the metal surface, the oxygen can be chemisorbed on the surface. The chemisorption process will be described in more detail in Chapter 4. If one continues to dose oxygen onto a metal surface, the oxygen coverage will increase up to a critical value where the repulsive interaction between the O ad-atoms prevents adsorption on the nearest neighbor site and it becomes energetically more favorable for the oxygen atoms to start penetrating the metal surface and form an oxide [56].

3.4.1 Oxide growth

Generally the oxidation process of metal surfaces is discussed within a nucleation and growth model. In a first step, stable oxide nuclei are formed on the metal surface from which the film may grow. Oxide growth can be described by the growth models described in Section 3.6.1. In order for the oxidation to proceed the oxygen molecule needs to dissociate on the surface and a charge transfer between the metal and oxygen occurs. The oxidation kinetics is dictated by both the supply of metal atoms, which have to detach from the metallic network, and by the atomic surface oxygen species which have to be formed by dissociation of molecular oxygen from the gas phase. Also, the transport of at least one reactant through the product is important. In order to replace a metal-metal bonding with a metal-oxygen bonding, energy is needed which is usually accomplished by increasing the temperature.

Metal oxides represent an interesting class of materials with a wide range of applications. In this work several types of oxides have been studied at the atomic scale to understand and eventually to improve the physical and chemical properties of their surfaces. Below the structures formed upon oxidation of Ag and Pd are discussed.

3.4.2 Oxidation of Ag(111)

When exposed to oxygen, the Ag(111) surface displays a range of reconstructions depending on the oxygen coverage. Due to the importance of Ag oxides in various applications, these structures have been studied intensively since the 1970s [57, 58, 59, 60, 61, 62, 63]. Despite over 40 years of research, a detailed understanding of many of these structures is still missing and recent studies indicate that the oxidation of Ag(111) is more complicated than previously believed [64]. This may have implications for the understanding of the catalytic processes over Ag.

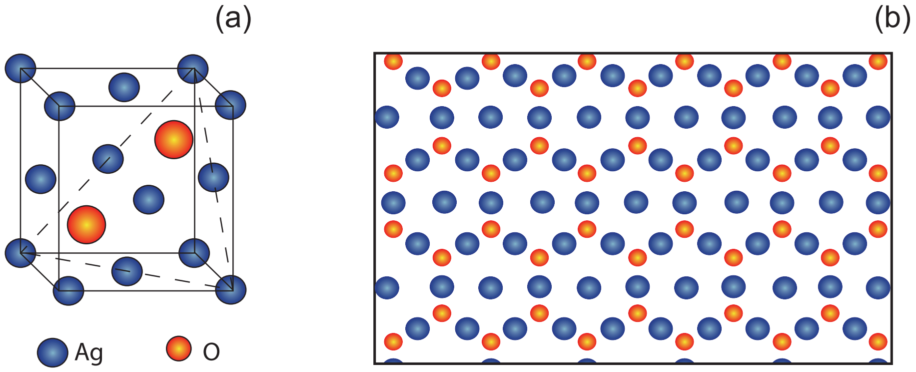

Figure 3.7: (a) The unit cell of the Ag_2O. The (111) plane is indicated by the dashed line. The one layer model of the (111) orientation of Ag_2O is shown in (b).

The first observed oxygen-induced structure on Ag(111) is the $p(4 \times 4)$ structure. This surface structure was observed in 1972 by G. Rovida *et al.* [63]. A structural model based on a Ag-O-Ag three layer slab of bulk oxide Ag_2O in (111) orientation rotated by 30° was proposed (see Fig. 3.7 (b)). Since then different techniques have been used to solve the structure and different models have been proposed [65, 66, 67, 68, 69, 70, 71]. A more convincing model based on several experimental techniques combined with theoretical simulations was presented by Schmid [72] and Schnadt [73] in 2006. The reported model was found to have no resemblance to bulk silver oxide, instead a structure composed of a triangular arrangement of six Ag atoms was proposed. The Ag atoms in the triangles are placed in either *fcc* or *hcp* sites as illustrated in Fig. 3.8. Each pair of Ag triangles is connected by two O atoms, resulting in six oxygen atoms per unit cell.

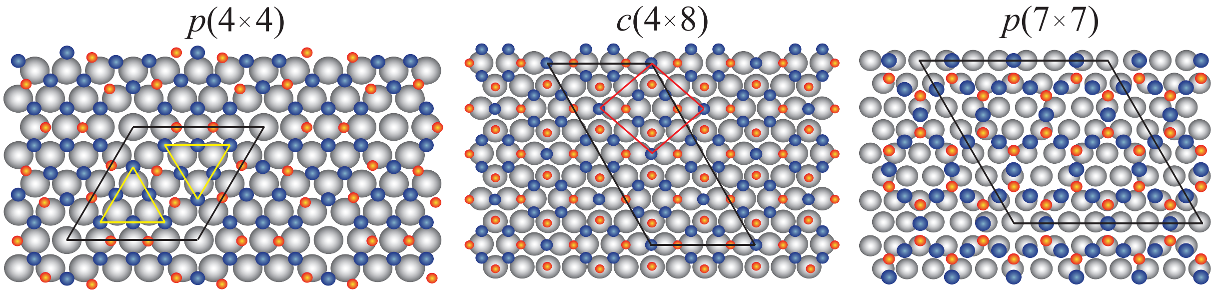

Figure 3.8: Oxygen-induced surface structures on Ag(111): $p(4\times4)$, $c(4\times8)$ and $p(7\times7)$. The red spheres represent the O atoms, the gray spheres the Ag(111) substrate atoms and blue spheres the overlayer Ag atoms. The unit cells are indicated by the black lines and the yellow lines indicate the Ag_6 building blocks.

In addition to the $p(4\times4)$ structure, a number of other oxygen-induced structures on Ag(111) have been reported. The $p(4\times5\sqrt{3})$rect and $c(3\times5\sqrt{3})$rect structures have similar O coverage (0.375 ML for the $p(4\times4)$ and $p(4\times5\sqrt{3})$rect phases and 0.4 ML for the $c(3\times5\sqrt{3})$rect phase) and are composed of triangular arrangements of Ag atoms [64].

In paper II we have studied the oxidation of Ag(111) with atomic oxygen. The results show the formation of more oxidized silver surfaces as compared to the $p(4\times4)$ phase for higher oxygen exposure, namely the $c(4\times8)$ and Ag_2O like phases. The proposed model for the $c(4\times8)$ phase is shown in Fig. 3.8. The Ag atoms occupy both bridge and hollow sites and the O atoms are located in bridge or on-top positions. Above 0.5 ML, bulk-like Ag_2O islands start to form on the Ag(111) surface. The bulk silver oxide, Ag_2O was found to grow in a Stranski-Krastanov growth mode on Ag(111) [74]. A model based on a hexagonal arrangement with a $p(7\times7)$ periodicity was proposed for a single-layer Ag_2O bulk-like oxide as shown in Fig. 3.8. It consists of hexagonal rings structures of Ag atoms coordinated to two O atoms where the bonding of the oxide layer to the substrate is mediated by O atoms sitting on bridge, three-fold and on-top sites.

In this work we have studied the interaction of silver oxides with CO and NO and found that CO/NO may react with the adsorbed oxygen on the $p(4\times4)$ structure and form carbonates (CO_3) or nitrates (NO_3). The results are presented in Papers IV-V.

3.4.3 Pd oxidation

The interaction of Pd with oxygen has extensively been studied in the literature [75, 76, 77, 78, 79, 80, 81]. The oxidation of Pd(100) results in first the formation of two ordered overlayers in UHV, the $p(2\times2)$ and $c(2\times2)$ with coverages of 0.25 and 0.5 ML, respectively where oxygen atoms occupy the 4-fold hollow sites as illustrated in Fig. 3.9 [82, 83]. These chemisorbed structures were also observed during CO oxidation in a 1:1 ratio of CO and O_2 below 450° C

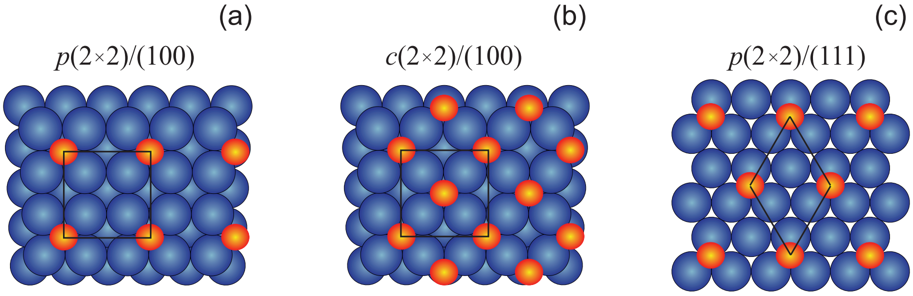

Figure 3.9: Schematic representation of the $p(2\times2)$ (a) and $c(2\times2)$ (b) adlayer structures on Pd(100) and $p(2\times2)$ (c) structure on Pd(111). The blue spheres represent Pd atoms while the small red spheres are O atoms.

(Paper XIII). A similar chemisorbed overlayer has also been observed to form on Pd(111) [84] ($p(2\times2)$, 0.25 ML as shown in Fig. 3.9 (c)).

At higher oxygen coverages a surface oxide forms with a $(\sqrt{5}\times\sqrt{5})$R27° in plane periodicity and a coverage of 0.8 ML, accompanied with a reconstruction of the topmost Pd layer as illustrated in Fig. 3.10 (a). We found that a similar surface oxide also forms on Pd nanoparticles (Paper VIII). As reported earlier [78], this surface oxide can be described by a bulk-like PdO(101) overlayer on top of Pd(100) where the Pd atoms are coordinated to 2 or 4 O atoms and the O atoms are coordinated to 3 or 4 Pd atoms. Every second row of oxygen atoms is located slightly below the surface as it can be seen in the side view image in Fig. 3.10 (a).

In contrast, the resemblance to the bulk oxide is lost when a surface oxide forms on the more closed surface of Pd, the (111) surface. The surface oxide that forms on Pd(111) has a "persian carpet" like structure in STM with a $(\sqrt{6}\times\sqrt{6})$ periodicity, a coverage of 0.67 ML and a Pd_5O_4 stoichiometry [80]. The Pd atoms occupy bridge or hollow sites and are coordinated to 2 or 4 O atoms as shown in Fig. 3.10 (b). Similar to the $(\sqrt{5}\times\sqrt{5})$R27°/Pd(100), the $(\sqrt{6}\times\sqrt{6})$/Pd(111) presents a buckling of the O lattice: half of the O atoms are sitting at the interface between the surface oxide and the substrate and are also coordinated to the subsurface Pd atoms.

By further oxidation of the Pd surface, a bulk-like 3D oxide may form. The bulk PdO crystallizes in a tetragonal structure (a=b= 3.043 Å , c= 5.336 Å) [85] with all Pd atoms having an equivalent planar coordination to 4 O atoms and all O atoms are tetrahedrally surrounded by 4 Pd atoms (Fig. 3.11 (a)). It has been reported that a bulk oxide forms on the Pd(100) surface in oxygen excess atmosphere above 600 K with a Stranski-Krastanov growth mode [83, 86] where the islands of PdO are formed on top of the surface oxide resulting in a quite rough surface. PdO(101) has been shown to be the most favorable orientation of the PdO on Pd(100) due to the low misfit of the film and the substrate [87]. This is the only low index

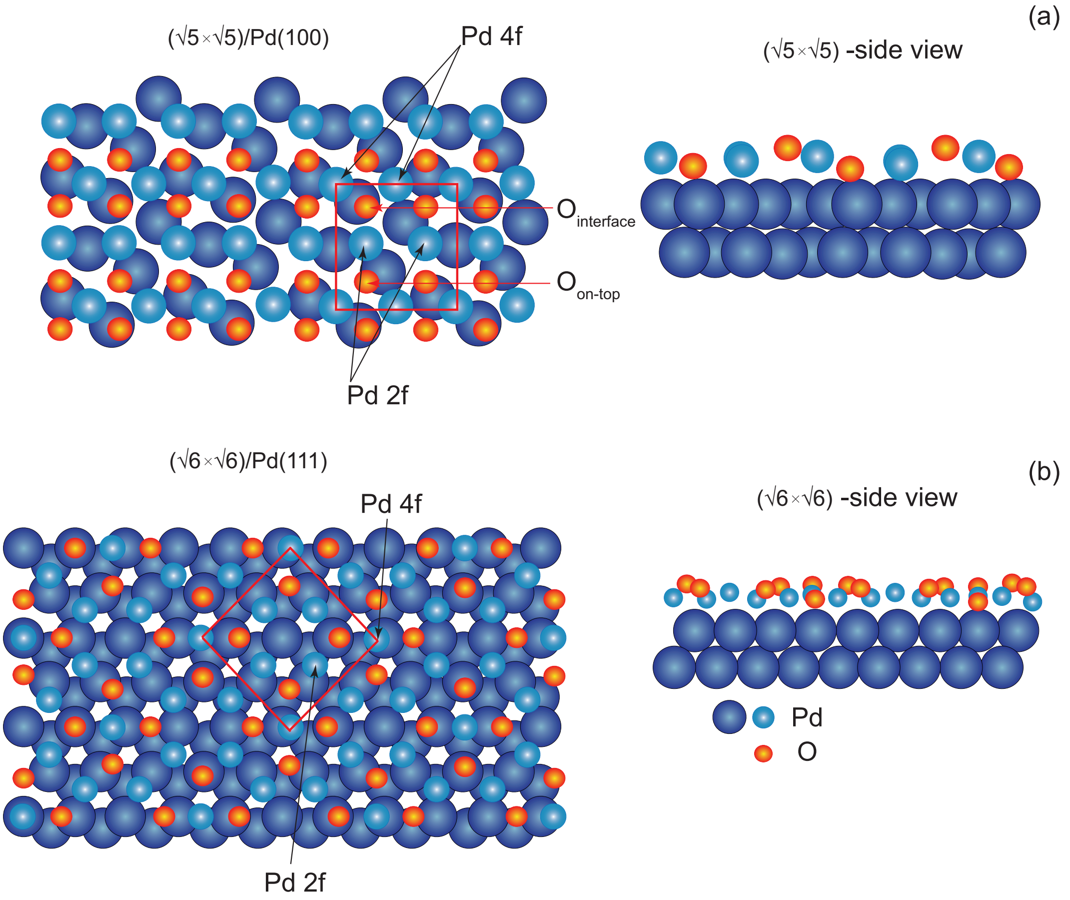

Figure 3.10: Schematic representation of the ($\sqrt{5} \times \sqrt{5}$)R27° (a) and ($\sqrt{6} \times \sqrt{6}$) (b) surface oxides on Pd(100) and Pd(111), respectively. The unit cells are indicated by the red squares. The blue spheres represent Pd atoms while the small red spheres are O atoms. The Pd atoms at the surface are lightened.

surface termination of bulk PdO that has undercoordinated metal atoms at the surface. The stoichiometric PdO(101) surface consists of alternating rows of Pd or O atoms with different coordinations (3- or 4-fold coordinated) with half of the surface O and Pd atoms coordinatively unsaturated (undercoordinated). In Paper VII we have confirmed previous investigations [88, 89] and by using spectroscopy techniques we have found strong indications that a PdO(101) also form on the Pd(111) surface.

3.5 Phase stability

Different adsorbate-substrate structures may be formed during the adsorption of gases. The stability of these structures is determined by the total surface free energy, which should be minimized. The system with the lowest surface free energy is the most stable one.

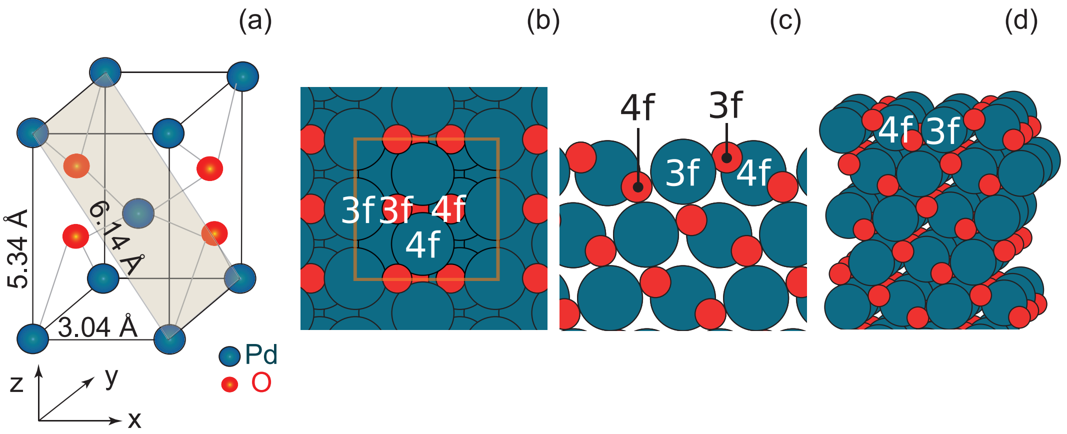

Figure 3.11: The tetragonal unit cell of bulk PdO (a) with the (101) plane indicated. Model structure of PdO(101) showing both top (b) and side views (c-d). Pd and O atoms are indicated by the green and red colours, respectively.

A useful method that has also been used throughout this work to complement the experimental data and predict the stability of different adsorbate-substrate structures is *ab initio* thermodynamics which is described in more detail in Chapter 6 (section 6.7.2).

Surface free energy

The internal energy of a system, E, depends on the entropy, S, the volume, V and the number of particles N in the system. It costs energy to form a surface and the internal energy of a system will increase by a value proportional to the area of the surface formed, A, and the proportionality constant is called the surface free energy, γ:

$$E^{surf} = TS - pV + \mu N + \gamma A, \tag{3.2}$$

where T is the temperature, p is the gas pressure and μ is the chemical potential of the system. The surface free energy plays a very important role in the determination of the equilibrium structure of a surface. Introducing the Gibbs free energy of the surface ($G^{surf} = E^{surf} - TS + pV$), the surface free energy can be written as:

$$\gamma = \frac{1}{A}[G^{surf} - N\mu], \tag{3.3}$$

For a multicomponent system in equilibrium with a gas reservoir, the surface free energy is written as:

$$\gamma(T, p_i) = \frac{1}{A}\left[G^{surf} - \sum_i N_i \mu_i(T, p_i)\right], \tag{3.4}$$

where i refers to the various species present in the system and the chemical potential depends on the pressure and temperature conditions of the surrounding gas phase. Surfaces will always tend to minimize the surface free energy.

3.6 Thin films

3.6.1 Growth modes

The adsorption process may result in the creation of a thin film/overlayer on the exposed surface. The growth of thin films have previously been described in the literature [90]. In general three different growth modes can be distinguished and are illustrated in Fig. 3.12 [91]: Frank-van-der Merwe (FM), Vollmer-Weber (VW)and Stransky- Krastanov (SK) growth.

The FM growth mode is usually encountered for overlayers with surface energy lower than the substrate ($\gamma_{substrate} > \gamma_{inerface} + \gamma_{film}$, where γ_x represents the surface free energy of material X) and no strain resulting in a complete wetting of the substrate, i.e. layer-by layer growth. When the interaction between the layer atoms is greater than the film-substrate interaction, a 3D island growth is observed (VW) ($\gamma_{substrate} < \gamma_{interface} + \gamma_{film}$). Sometimes, the layer-by-layer growth at a given thickness may be replaced by a 3D growth, generally referred to as a SK mode.

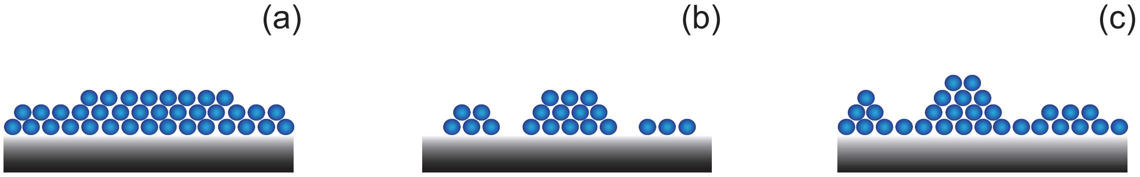

Figure 3.12: Different modes of film growth: (a) Frank-van-der Merwe, (b) Vollmer-Weber and (c) Stranski-Krastanov growth modes.

3.6.2 Wulff construction

Wulff construction is a method to determine the thermodynamically most stable shape of a crystal (particle) by assuming minimal surface free energy. The construction is based on Wulff's assumption that the distance from the center of the particle (crystallite) to the surface of a particular plane is proportional to the surface free energy. The particle shape is thought of as a polyhedron with several possible different faces i, which have a specific surface free energy γ_i. The surface plane with the smallest free energy will dominate over the others. The closed packed surfaces have in general the smallest surface free energies and dominate on small particles as for example the (111) surfaces for the *fcc* and *hcp* metals and (110) for the *bcc* metals [92, 93]. When a face of the crystal makes contact to the substrate, the interfacial energy should also be considered. A large interface energy leads to wetting of the surface. It is important to note that the surface free energy of a particle may change depending on the surrounding gas pressure, which in turn affects the surface structure, changing its equilibrium shape.

4

Gas-surface Interaction

As described previously in Chapter 2, the aim of the surface science approach to catalysis is to obtain an atomic scale understanding of catalytic reactions. On a molecular level this means understanding the adsorption and desorption of molecules on the nanoparticles, the breaking of bonds in the reactant molecules and the formation of bonds in the products. One of the most important reactions in heterogenous catalysis is the reaction between the gas molecules with the metal surface [94]. The interaction of gases with NiAl(110), Ag(111), Pd(111) and Pd(100) surfaces has been studied in this work. This chapter contains the main concepts involved when gases adsorb and dissociate on a metallic surface. For this, knowledge of the adsorption process and adsorbate geometries are important.

Adsorption is the process where molecules from the gas phase (adsorbates) bind on a solid/ liquid surface (adsorbent, substrate). In 1932, Lenard-Jones presented a theory of adsorption [95]. The opposite process, in which the molecules are removed from the surface, is called desorption. It is important to note that the adsorption of a gas onto a solid is different from the absorption of a gas into a solid, the latter referring to the process in which the gas molecules dissolves into the bulk of the material [96]. Depending on the bonding energy between the surface atom and the gas molecule/atom, the adsorption process can be divided into two classes: a weak interaction between adsorbate and the substrate (physisorption) with a small adsorption energy (< 0.3 eV) and a stronger interaction (> 1 eV) with the formation of a chemical bond between the adsorbate and the surface (chemisorption) [97]. Chemisorption involves a rearrangement of the valence electrons of the substrate and adsorbate and electrons are shared or exchanged. If the interaction modifies the molecular structure of the adsorbate, the molecule may dissociate and the process is referred to as dissociative adsorption.

Fig. 4.1 shows the potential energy curves for a molecule X_2 approaching a surface. When the molecule approaches the metal surface it will first encounter a weak Van der Waals interaction and can be physisorbed on the surface if no chemical bonds are formed. At closer distances, the wave function of the electrons in the molecule and in the surface atoms start to overlap leading to a repulsion. Because of repulsive forces, the potential energy increases as the molecule approaches the metal surface. If the molecule can interact with the *sp* and

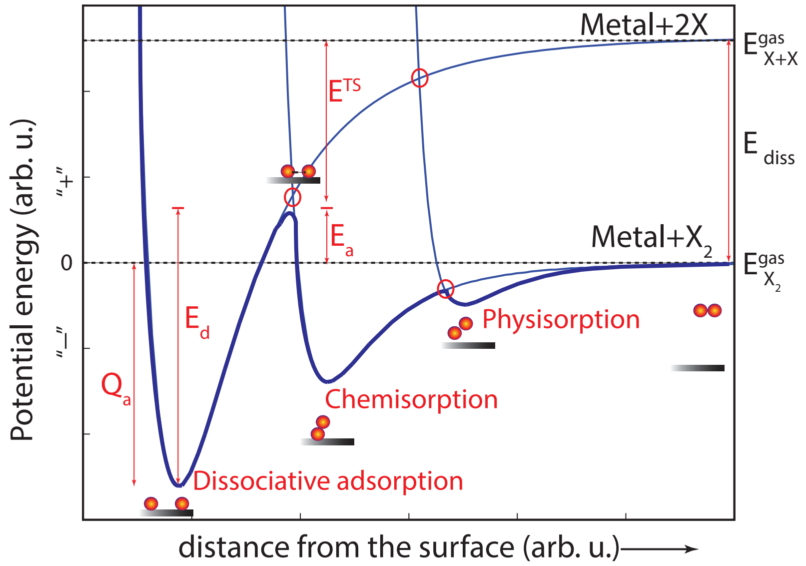

Figure 4.1: Lenard-Jones potential energy curves for a molecule X_2 approaching a metal surface illustrating the different adsorption states. The position of the cross points between the three curves is only representative. E_a is the activation energy for the dissociative adsorption, Q_a represents the heat of adsorption (chemisorption) and E_d is the activation energy for the desorption of the atoms. E_{diss} represents the dissociation energy of the molecule in the gas phase and E^{TS} represents the transition state energy.

d bands of the metal atoms (chemical interaction, see section 4.1 below) it may become chemisorbed and a shallow minimum is reached. If the molecule has enough energy to overcome the energy barrier E_a then it may dissociate into two chemisorbed atoms (dissociative chemisorption) and the energy of the adsorbed atoms is Q_a. As it will be presented later, the stronger the bond of the constituent atoms to the surface, the lower the dissociation barrier will be. The chemisorption of $2X$ atoms is associated with a strong bond formation and the crossing point between the two curves marks the activation energy for dissociative chemisorption. The desorption of the chemisorbed atoms has an activation energy $E_d = -Q_a + E_a$.

The main concepts behind adsorbate surface interactions are given below. For a more detailed description the reader is referred to, for example, references [10, 98, 99, 100].

4.1 Chemical bonding

4.1.1 Bonding in molecules and metals

When two atoms A and B interact their wavefunctions overlap, electrons are shared and a bond is formed. The molecular orbitals are formed as linear combinations of atomic orbitals. Each atomic orbital has an electron energy and for a molecular orbital there are two energy levels where the electron can reside: bonding and antibonding levels. Molecular orbital energy diagram for CO and O_2, two of the most used molecules in the present work, are given in Fig. 4.2. For the CO molecule, the *s* and *p* atomic orbitals are so close in energy that some additional mixing takes place (*sp* hybridization) [101].

For a metal, the metallic bond can be understood by making use of the tight binding model and describing the system as a linear combination of the different participating orbitals, similar to the orbital picture of molecular bond discussed above. The metallic bond is formed by the interaction of *s*, *p* and *d* orbitals from many atoms. The *s* and *p* orbitals are shared among all the other atoms in the crystal while the *d* orbitals are more localized. There is a large overlap between the *sp* orbitals (strong interaction) giving rise to a continuous (broad) band of levels, while there is little overlap (weak interaction) between the *d* orbitals forming a narrow band [102, 103]. A band can be viewed as a collection of many molecular orbitals and each energy level in a band is called a state. The density of states (DOS) represents the number of states at a given energy. The bands are filled with electrons up to the Fermi level. Almost all of the samples used in the work presented in this thesis are single crystal transition metals. A transition metal has partially filled *sp*-band and a *d*-band filled to a certain degree. Fig. 4.3 shows a typical DOS for a transition metal.

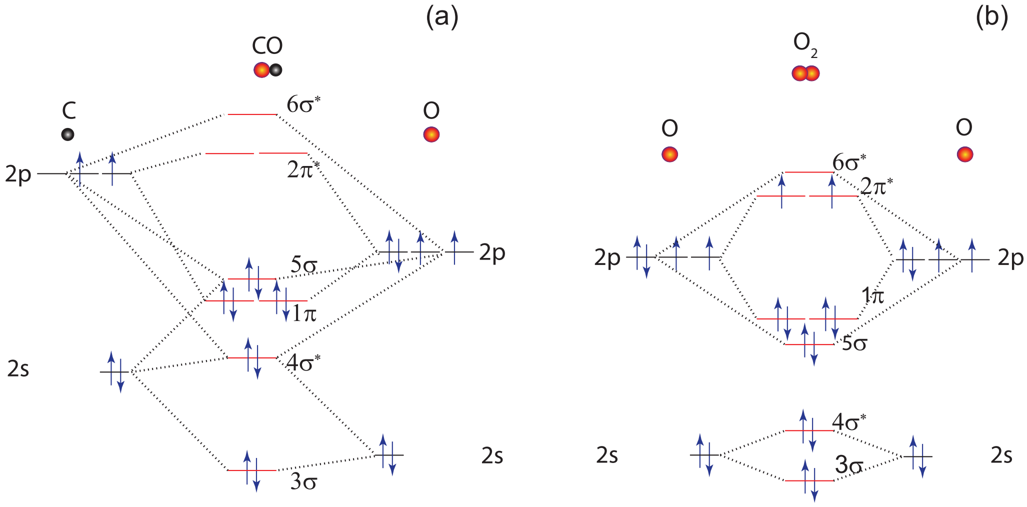

Figure 4.2: Molecular orbital energy level diagram for the CO (a) and O_2 (b) molecules.

4.2 Newns-Anderson model

The Newns-Anderson model describes the main features involved when an adsorbate approaches the surface of a metal and the interaction between the electronic levels of the metal and adsorbate [104, 105]. The product formed when an atom or a molecule from the gas

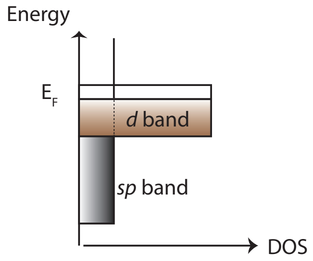

Figure 4.3: Schematic illustration of the density of states (DOS) of a transition metal.

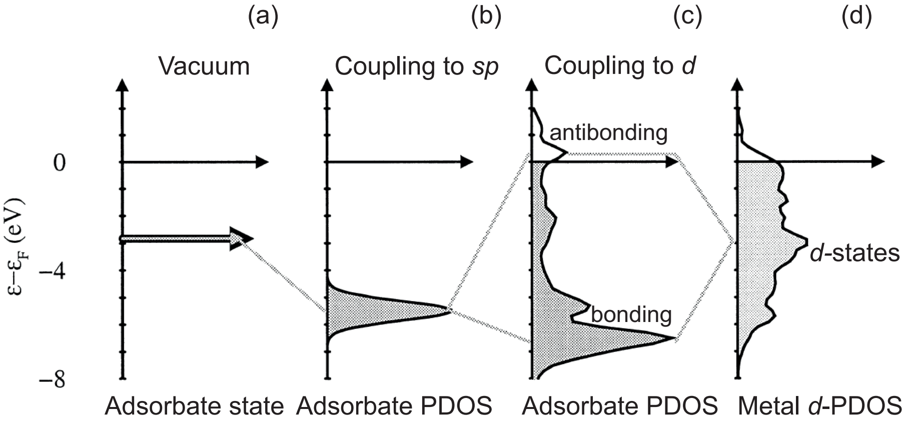

Figure 4.4: Schematic illustration of the formation of a chemical bond when an adsorbate state (a) interacts with *sp* (b) and *d* (c) states of a transition metal. The DOS is projected onto the adsorbate state and the metal PDOS is shown for comparison in (d). Recreated from [103].

phase adsorbs and forms a bond on the surface is called adsorbate. The adsorbate-surface interaction is considered as a two step process. First the adsorbate (Fig. 4.4 (a)) interacts with the *sp* states and secondly with the *d*-band of the metal [98]. By interaction with the *sp*-band the energy levels of the adsorbate broaden and shift down in energy as shown in Fig. 4.4 (b). In practice, due to the large number of electronic states, it is convenient to project the DOS of the interacting metal-adsorbate system on the adsorbate levels. The interaction with the *d*-band will give rise to a two level situation with bonding and antibonding states, located below and above the metal *d*-band, respectively, as shown in Fig. 4.4 (c). In the case of a molecule adsorbed on a surface, both the bonding and antibonding orbitals of the molecule contribute to the chemisorption bond by interaction with the *sp* states and *d*-band of the surface as it will be described below for CO chemisorption (section 4.4). It is the number of the metal-adsorbate antibonding states that strengthens the adsorbates bonding to the surface. When these antibonding states are located above the Fermi level they are empty and therefore a stronger bonding of the molecule to the substrate may take place.

The above discussion considers only the hybridization between the overlapping adsorbate-

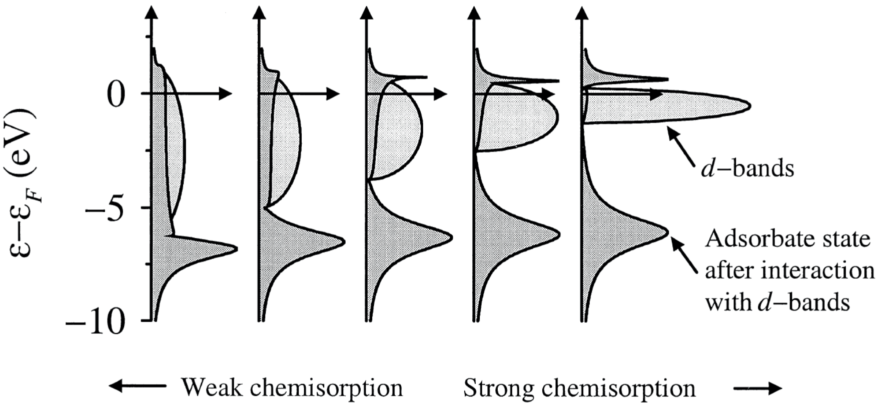

Figure 4.5: The influence of the position of the *d*-band centre in determining the strength of the metal-adsorbate interaction. Adapted from [103].

metal states, which will lead to an attraction as long as the antibonding metal-adsorbate states are not completely filled. In addition, according to quantum mechanics, when the electronic states overlap, they shall be orthogonal, which leads to a Pauli repulsion between the adsorbate and the metal states. This repulsion will counteract the attractive effect when the antibonding metal-adsorbate states are completely filled [106].

4.3 *d*-band and surface reactivity

The adsorbate interaction with the *sp*-band of the metal can not explain the difference in bonding for the different transition metals as they have similar *sp*-bands. It is the filling of the *d*-band that differs among the transition metals. Most of the transition metals have a partially filled *d*-band. Moving to the right in the periodic table the filling of the *d*-band increases, the width of the band decreases because the overlap between the *d* states decreases, and the *d*-band center shifts down. The position of the metal *d*-band center influences the antibonding filling of the metal-adsorbate system. Stronger bonding will take place for metals that have a *d*-band closer to the Fermi level (e.g. Pd) as illustrated in Fig. 4.5. A continued filling of the *d*-band towards the right in the periodic table will result in a graduate weakening of the adsorbate-metal bond strength [107]. Therefore, a weaker bond is expected for metals with a deeper (low) lying *d*-band like Ag or Au.

This is illustrated in Paper III where we have compared the interaction between atomic oxygen and the Pd(111) and Ag(111) surfaces. Fig. 4.6 shows the projected density of states (PDOS) of O $2p$ on the Pd(111) and Ag(111) *d*-bands (red line). The Pd(111) *d*-band is high lying and upon interaction of the O $2p$ with the *d*-band of Pd, the O $2p$-metal states are observed to split into bonding and antibonding components, with antibonding states above

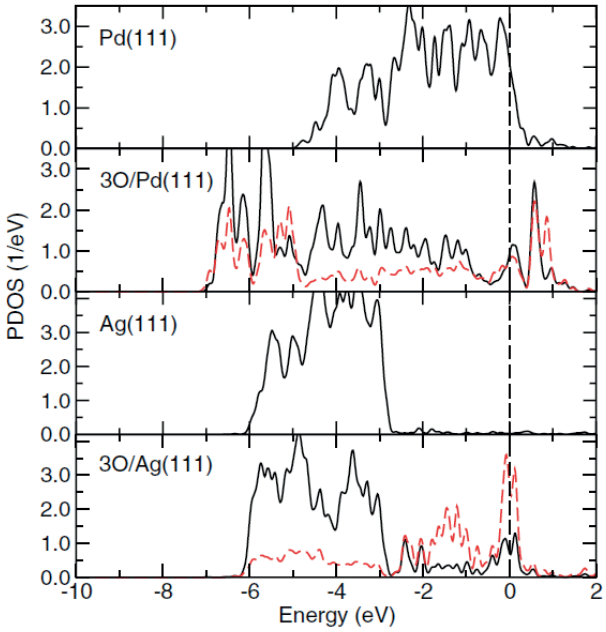

Figure 4.6: PDOS of Pd(111), O/Pd(111), Ag(111) and O/Ag(111). The red line represents the projection on O 2*p*. Adapted from Paper III.

the Fermi level. In contrast, Ag has a filled *d*-band and the interaction of O 2*p* with the low lying, narrow *d*-band of Ag has a much lower contribution to the bonding of oxygen due to the fact that the antibonding states are located below the Fermi level and are filled. Therefore oxygen adsorbs weaker on Ag as compared to Pd.

A narrowing of the *d*-band at the surface of a metal as compared to the bulk is often observed and is due to the reduced coordination of the surface atoms [103]. In order to retain the same number of electrons the *d*-band shifts upwards. The same applies to the undercoordinated sites on a surface. The *d*-band of the undercoordinated atoms will be narrower and shifts upwards. This results in a stronger bonding with the adsorbate molecules, which increases the transition state energy and therefore lowers the dissociation barrier of the molecule, $E_a = E_{diss} - E^{TS}$ (see Fig. 4.1). The fact that the undercoordinated atoms show an increased adsorption energy for different gas molecules has been observed in Papers VII-IX.

Further, the *d*-band model can be applied to understand ligand field effects, where the properties of an atom are modified by its neighbors. As discussed in Papers XI-XII, the undercoordinated metal (Pd) atoms with an oxygen atom below were observed to facilitate methane oxidation over Pd. The presence of the oxygen atom underneath reduces the repulsive interaction between the undercoordinated Pd atoms and methane which allows for methane dissociation. An obvious conclusion can be drawn from the points discussed above: in order to enhance the reactivity one shall find ways to shift the metals *d*-band upwards.

4.4 Molecular chemisorption: examples

An example of a simple diatomic molecule adsorption on a metal surface is given in this section to illustrate how the surface bond formation takes place for a molecule. CO adsorption has been studied in detail experimentally and in several theoretical investigations [108, 109, 110]. CO is known to adsorb molecularly in an upright orientation with the oxygen atom pointing upwards on the late transition metals. This is due to the fact that the highest occupied molecular orbital (HOMO) is localized on the C atom making it the most reactive part of the molecule [111].

The molecular orbital-energy level diagram for the CO molecule is shown in Fig. 4.2 (a). In a simplified picture suggested by Blyholder, bonding between CO and a metal or metal oxide surface occurs through electron donation from the CO 5σ (HOMO) molecular orbital to unoccupied metal states, accompanied by back-donation from the surface to the CO 2π^* lowest uncoccupied molecular orbital (LUMO) [112]. The interaction of CO with a metal *sp* states gives rise to a broadening and a downshift of the 2π^* and 5σ states, while the interaction with the *d*-band gives rise to bonding and antibonding states as illustrated in Fig. 4.7 for CO adsorption on Pt(111). The antibonding part of the 5σ orbital is located above the Fermi level and is therefore empty indicating a depletion of charge from the 5σ orbital. Before adsorption, the 2π^* orbital is empty and upon interaction with the *d*-band of Pt the bonding part of this orbital becomes filled due to charge transfer from the metal to CO strengthening the bonding to the surface. In some cases the back donation from the metal *d*-band to the 2π^* level of CO is suppressed if the metal *d*-band is low lying (i.e. Ag, Au) giving rise to a weak CO-metal bond. Only associative CO adsorption has been observed in my work (Papers IV, VIII, IX).

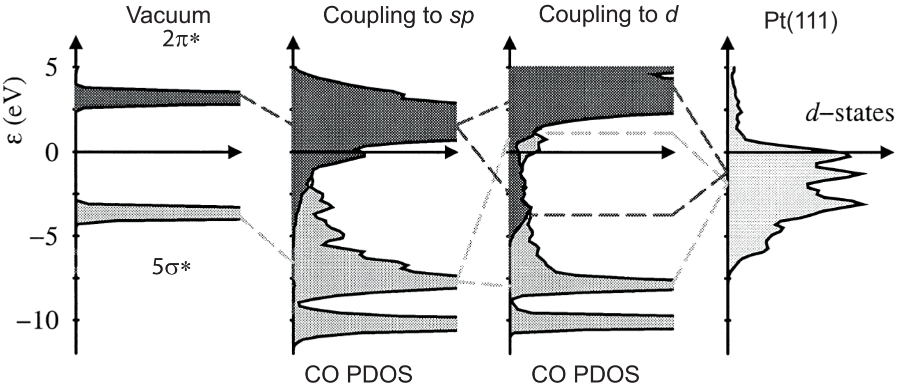

Figure 4.7: The PDOS onto the 5σ and 2π^* orbitals of CO in vacuum and on Pt(111) *sp* and *d* states. Recreated from [103].

Because NO has a similar molecular orbital structure to that of CO it is expected that NO adsorption will be similar to CO adsorption. Still, because NO has one extra valence electron compared to CO, located in the antibonding orbital, the NO molecule is expected to dissociate more easily than the CO as the bond to the substrate is increased upon adsorption. This was also observed experimentally for the Rh case, where it was observed that CO does not dissociate while NO does [113]. In Paper V we have investigated the NO adsorption on an oxidized Ag surface and observed the dissociation of NO at room temperature (RT) conditions with the formation of nitrates (NO_3) and even more complex NO_x species.

A similar interaction as described above for the CO chemisorption takes place during the oxygen interaction with a metal surface. O_2 is a diatomic molecule that has been shown to adsorb differently on different metal surfaces. For example, it has been observed to adsorb dissociatively on Cu(100) [114] and molecularly on Pt(111) at 77 K [115]. The molecular energy diagram for O_2 is shown in Fig. 4.2 (b). The position of the metal d-band will influence the adsorption process of O_2 on different transition metals. The donation of electrons from the metal atoms to the antibonding $2\pi^*$ orbital of oxygen leads to a weakening of the internal O_2 bond and has as a consequence the dissociation of the oxygen molecule.

5

Surface Chemical Reactions

One of the aims of surface science, as discussed in Chapter 1, is to explain surface chemical reactions. A chemical reaction (transformation) involves breaking of bonds between atoms and formation of new ones. Most catalytic reactions rely on chemisorption of the reactant on the surface so that significant electron transfer can take place [116].

To understand a chemical reaction, two basic questions are to be answered:

- Is the reaction energetically favorable? This is the subject of chemical thermodynamics (describes the system energy);
- If yes, how fast will it proceed? This is the subject of chemical kinetics (describes the rate at which a chemical reaction occurs).

An interesting example is the transformation of diamond to graphite. Diamond and graphite are both forms of carbon, but graphite is thermodynamically more stable at environmental temperature and pressure conditions since it has a lower free energy. Therefore, from a thermodynamic point of view, diamond should transform to graphite under ambient conditions. A huge amount of energy is, however, needed to break the C-C bonds in diamond and therefore there is a high activation energy for the transformation to proceed [117]. A schematic representation of the transformation of diamond to graphite is shown in Fig. 5.1. The activation energy represents the height of the energy barrier that has to be surmounted for the reaction to proceed (see Fig. 1.1). Thus thermodynamics, that only tells us that a reaction will happen if the products are more stable than the reactants, is not the whole story of chemical reactions. We also have to know whether the reaction can or will occur at a reasonable rate. A brief theoretical approach to chemical kinetics is given below.

5.1 Reaction kinetics

5.1.1 Reaction rates and power rate laws

A general reaction between molecules A and B to give product molecules C and D can be described by:

$$aA + bB \rightleftharpoons cC + dD, \tag{5.1}$$

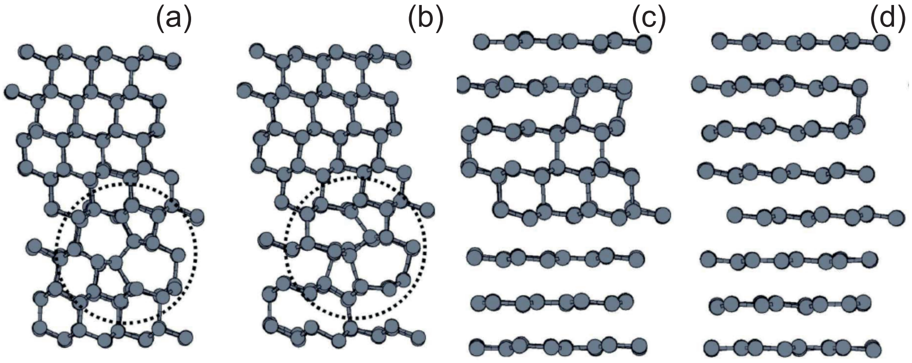

Figure 5.1: Schematic representation of the transformation of diamond to graphite (a-d). The bonds strength that hold the C atoms together in diamond (a) are weaker than those in graphite (d) where the atoms are strongly bonded into sheets that can slide over each other. Recreated from [118].

where *a, b, c, d* are the stoichiometric coefficients for the reaction. The frequency of collisions between A and B will be proportional to the concentration of each. One can follow the progress of a reaction by monitoring either the decrease in concentration of the reactants or the increase in concentration of the products. The reaction rate can be expressed in terms of the change in concentration with time:

$$Rate = -\frac{1}{a}\frac{d[A]}{dt} = -\frac{1}{b}\frac{d[B]}{dt} = \frac{1}{c}\frac{d[C]}{dt} = \frac{1}{d}\frac{d[D]}{dt}, \tag{5.2}$$

where $d[X]$, is the change in concentration of substance X over a time period *dt*. The minus sign in front accounts for reactants that are being consumed. The rate of a reaction is related to the concentration of reactants through a proportionality constant called the rate constant, k, which describes the speed of the reaction. Then the rate can be written as:

$$Rate = k[A]^x[B]^y, \tag{5.3}$$

where the sum $x + y$ is called the "order" of the reaction. This equation is also called the rate law. The reaction order gives information of how the reaction rate changes with the concentration of the reactants. In order to understand how the concentrations of the species in a chemical reaction change with time it is necessary to integrate the rate law. This can easily be done for the first order reactions, where the reaction rate is limited by the concentration of one of the reactants, but things get more complicated for higher order reactions. For first order reactions one gets:

$$Rate = -\frac{1}{a}\frac{d[A]}{dt} = -k[A], [A] = [A]_0 e^{-kta}, \tag{5.4}$$

i.e. an exponential decay, where $[A]_0$ is the initial concentration of A.

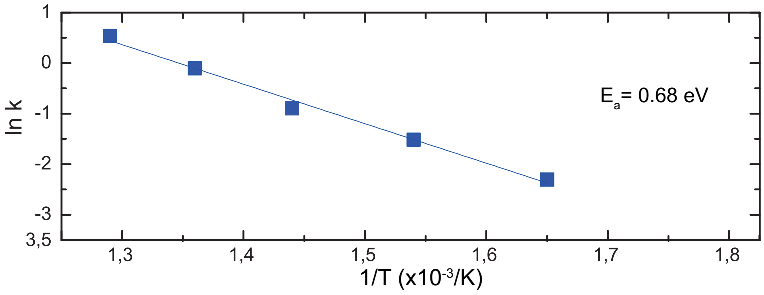

Figure 5.2: Arrhenius plot example for the CO_2 formation rate over Pd(100) at a total pressures of O_2+CH_4 of 0.7 mbar. The ratio between O_2 and CH_4 was kept constant (5:2).

5.1.2 Temperature dependence of the rate: Arrhenius equation

The dependence of the rate constant of a reaction on temperature can be expressed by the following equation, known as the Arrhenius equation:

$$k(T) = Ae^{-E_a/RT}, \tag{5.5}$$

Where E_a is the activation energy (kJ/mol) of the reaction, R is the gas constant, A is the collision frequency and T is the temperature. The preexponential factor, $A = A(T)$, is also a function of temperature but the temperature dependence is much weaker and therefore can be considered as constant in the above equation. This implies that the rate of a specific reaction will increase drastically as the energy barrier is reduced and even a small reduction of the activation energy can improve a catalyst significantly.

Equation (5.5) can also be expressed as:

$$\ln(k) = \ln(A) - E_a/RT. \tag{5.6}$$

By plotting the logarithm of the rate constant against the reciprocal temperature ($1/T$), a straight line is obtained as illustrated in Fig. 5.2. The slope of the line is equal to $-E_a/R$ and the intercept with the y axis is A. The activation energy can be obtained from the slope of the curve. It is interesting to note that the activation energy does not depend on an absolute number for the change in activity, but a relative change is fine. Therefore, the change in the gas concentration may be used instead of calculating the rate constant as, according to equation 5.4, the rate constant is proportional to the change in concentration/pressure. This has been employed in Paper XII where the mass spectrometry signal was used for the Arrhenius plots.

5.2 Catalytic reactions

The aim of the work in this thesis is to help developing new catalysts by providing a molecular (atomic scale) picture of the way surfaces catalyze chemical transformations. Catalytic reactions are often more complex than presented in the balanced equation. In most cases, they do not occur as a single step from initial state to final state as illustrated by eq. (5.1). The reactions that occur in a single step are called elementary reactions. The complex reactions consist of a series of elementary reactions, which have individual rate constants describing the speed of that specific step. The total reaction rate is almost completely determined by the elementary step with the highest energy barrier (= the rate determining step (RDS)). It is the height of the highest barrier and not the number of steps that determines the overall rate of the reaction.

Understanding catalytic reactions at the atomic level means unraveling the catalytic mechanisms and determine the kinetic parameters of all elementary steps. These include adsorption of reactants on the surface, diffusion on the surface, formation of product molecules and finally desorption from the surface. The sites where reacting molecules adsorb and later react are called active sites. Catalysts usually react with one or more reactants to form intermediates that subsequently give the final reaction product, and the catalyst is regenerated at the end of the reaction, as illustrated in the following typical reaction scheme:

$$X + Cat \rightarrow XCat \tag{5.7}$$

$$Y + XCat \rightarrow XYCat \tag{5.8}$$

$$XYCat \rightarrow ZCat \tag{5.9}$$

$$ZCat \rightarrow Z + Cat, \tag{5.10}$$

where Cat refers to the catalyst surface. Each of the steps involved are called elementary steps. The overall reaction can simply be written as:

$$X + Y \rightarrow Z. \tag{5.11}$$

Apart from accelerating chemical reactions catalysts can also influence their selectivity by decreasing the energy barrier for one particular reaction, which without the catalyst might be kinetically unfavored. This means that the same reactants can result in different products if different catalysts are used.

In this thesis the interaction of different molecules with solid surfaces, as well as subsequent reactions between the molecules have been studied and therefore this will be the focus of the remaining part of this chapter. The theory of gas adsorption on surfaces at equilibrium can be described by the Langmuir adsorption isotherms that give the relationship between the coverage of a particular gas and its pressure above the surface [52, 119]. For associative adsorption the coverage will be given by :

$$\theta = \frac{kP_A}{1 + kP_A}, \tag{5.12}$$

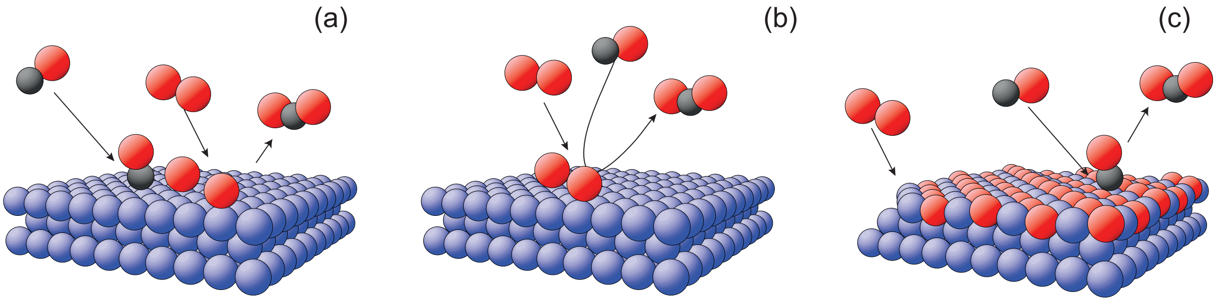

Figure 5.3: (a) Langmuir-Hinshelwood, (b) Eley-Rideal and (c) Mars-van Krevelen mechanisms.

(Langmuir adsorption isotherm for associative adsorption) where k is the adsorption equilibrium constant. There are cases when the adsorbate molecule splits into individual atoms when bonded to the surface (for example O_2 or H_2 usually dissociate upon adsorption). In this case the relation for the coverage becomes:

$$\theta = \sqrt{\frac{kP_{A2}}{1+kP_{A2}}}. \tag{5.13}$$

(Langmuir adsorption isotherm for dissociative adsorption). As k decreases exponentially with T, increasing T will result in a lower coverage and most of the reactants will be driven back to the gas phase.

5.2.1 Reaction mechanisms

Depending on how the gas molecules react with and on the catalytically active surface, various reaction mechanisms have been observed and they are schematically illustrated in Fig. 5.3 for the CO oxidation reaction.

The **Langmuir-Hinshelwood mechanism** is shown in Fig. 5.3 (a). In this mechanism both reactants are adsorbed on the surface where they diffuse and may react and form the product with a probability k [120]. If we assume that the reaction between the two adsorbed molecules is the RDS then the reaction rate will be given by:

$$Rate = k\theta_A\theta_B \tag{5.14}$$

where θ_A, θ_B are the coverages of species A and B, respectively and k is the rate constant given by relation (5.5). Using the Langmuir adsorption isotherms one can write expressions for the coverages of the two molecules and translate them into pressures of the gases above the surface. This was, however, not the focus of my work and therefore I will not give further details.

The **Eley-Rideal** mechanism is shown in Fig. 5.3(b) and is based on the assumption that only one of the reactant species is adsorbed on the surface and the other is in the gas phase when the reaction occurs [121]. There is no competition of the different species for the adsorption sites and the reaction rate will be given by:

$$Rate = k\theta_A P_B \tag{5.15}$$

This mechanism has only rarely been observed. An example is the carbon dioxide hydrogenation over Ni catalyst ($CO_2 + H_{2(a)} \rightarrow H_2O + CO$) [122].

Finally the **Mars-van Krevelen** mechanism is shown in Fig. 5.3 (c). In this mechanism one of the reactants is stored on the surface forming a layer of metal-reactant (MR), such as a surface oxide, and the other reactant adsorbs on the surface and can react with it reducing the surface [123]. It is also called the red-ox (reduction-oxidation) mechanism. A vacancy is formed on the surface when the reaction product desorbs and this can be filled again by one of the reactants. Below I will illustrate how these mechanisms can be applied to the reactions studied in this thesis.

5.3 Oxidation reactions: Pd surfaces in semi-realistic conditions

When it comes to catalytic reactions, it is still an open question whether the surface oxides are catalytically active for oxidation processes or inactive. It has been argued that oxides may deactivate the catalyst by blocking the active sites for the gas molecules to adsorb. In order to obtain an understanding of the molecules-oxide interaction, one can study the reduction or oxidation on preformed oxides. Therefore, a large part of the work presented in this thesis deals with the oxidation of Pd and Ag and the interaction with simple molecules such as CO, NO, and H_2.

Our measurements reveal that CO does adsorb on the undercoordinated metal sites at the surface of the PdO(101) where it may react with oxygen and form CO_2. Thus, an oxide may present active sites that are different from the sites on the clean metal surface and can therefore be promising for catalytic reactions.

CO oxidation reaction

After many years of research, the reaction mechanism for one of the simplest catalytic reaction, CO oxidation over Pt- group metals, is still not known. Early research indicated that the reaction occurs via a Langmuir Hinshelwood mechanism, where both CO and oxygen adsorb on the metallic surface and react to form CO_2. More recent research indicates that, at high oxygen pressures, the reaction proceeds via a Mars-van Krevelen mechanism over Ru(0001) when a $RuO_2(110)$ forms on the surface [124]. It has been reported that in particular the undercoordinated Ru atoms at the surface of the oxide are responsible for the increased activity of the RuO_2.

A particular surface orientation of bulk PdO, the PdO(101) is very similar to the $RuO_2(110)$, because both contain undercoordinated metal atoms that are expected to be reactive, and therefore a similar situation is also expected for CO oxidation over Pd. In paper XIII we have studied the CO oxidation over Pd(100) under high pressure conditions (0.5 Torr total pressure) at different partial pressures of O_2 and CO. The results show that the metal with chemisorbed oxygen is the active phase for low oxygen partial pressures. As the oxygen partial pressure was increased, the surface oxide $(\sqrt{5} \times \sqrt{5})R27°$ was observed to be highly active for CO oxidation. Thus the CO oxidation mechanism can be interpreted as both Langmuir Hinshelwood or Eley-Rideal mechanisms at low oxygen pressure as previously reported [125], or a Mars-van Krevelen mechanism at high oxygen pressures.

CH_4 oxidation reaction

The mechanism for methane oxidation over Pd catalyst is complex and has extensively been studied over the past 25 years due to its attractive potential for catalytic combustion applications. As methane is a very stable molecule, dissociative methane adsorption on metal surfaces shows a very low probability. In Papers XI-XII we have studied the total methane oxidation reaction over Pd(100) under oxygen excess. The results show that the PdO(101) has an increased activity for methane oxidation, suggesting a Mars-van Krevelen reaction mechanism. Our measurements also show that a single PdO(101) plane (the $(\sqrt{5} \times \sqrt{5})R27°$) is much worse than two layers of PdO(101) to dissociate CH_4. Interestingly, the activation barrier for the methane molecule to dissociate was found to drop from 4.5 eV in the gas phase to below 0.7 eV over the PdO(101) surface. This is a lower activation energy compared to the calculated value for a single layer PdO(101) (E_a=1.2 eV).

6

Techniques for Studying Surfaces

This chapter describes the methods that have been used in the present work to enable surface investigations on the atomic scale. The surface sensitivity of electron based methods can be understood from the short mean free path of low energy electrons, as described below. Most of the experiments were performed at synchrotrons, therefore a brief introduction to synchrotron radiation is given in the first part of this chapter.

6.1 Low energy electrons and surface sensitivity

Standard surface science techniques, such as X-ray Photoelectron Spectroscopy or Low Energy Electron Diffraction, employ low energy electrons as a probe to study surfaces. When electrons are emitted from a metal at low kinetic energies, they originate mostly from the surface atoms due to their short mean free path. The mean free path is the distance that the electron travels in the solid before it experiences the first event of inelastic scattering (energy loss process) [126] and it depends on the electrons kinetic energy. In Fig. 6.1 is shown the inelastic mean free path in different materials as a function of the kinetic energy [127]. As it depends to a less extent on the specific material, the curve shown in Fig. 6.1 is also called the universal curve for the electron mean free path. It can be observed that in the energy range of 10 to 1000 eV the mean free path of electrons is about 10 Å providing the surface sensitivity of electron based methods using electrons of these energies.

6.2 Synchrotron radiation

X-rays were discovered by W.C. Röntgen in 1895 and enabled scientists to probe crystalline structures at the atomic level. Since their discovery, X-rays have become an extremely important tool in the physical, chemical and biological sciences and in the fields of medicine and engineering.

X-ray sources have continuously been developed. Usually the X-rays are generated by bombarding a metal (anode) with high-energy electrons. X-ray sources can also be based on electron accelerators where the electrons are accelerated to very high speeds ($v \approx c$) and when

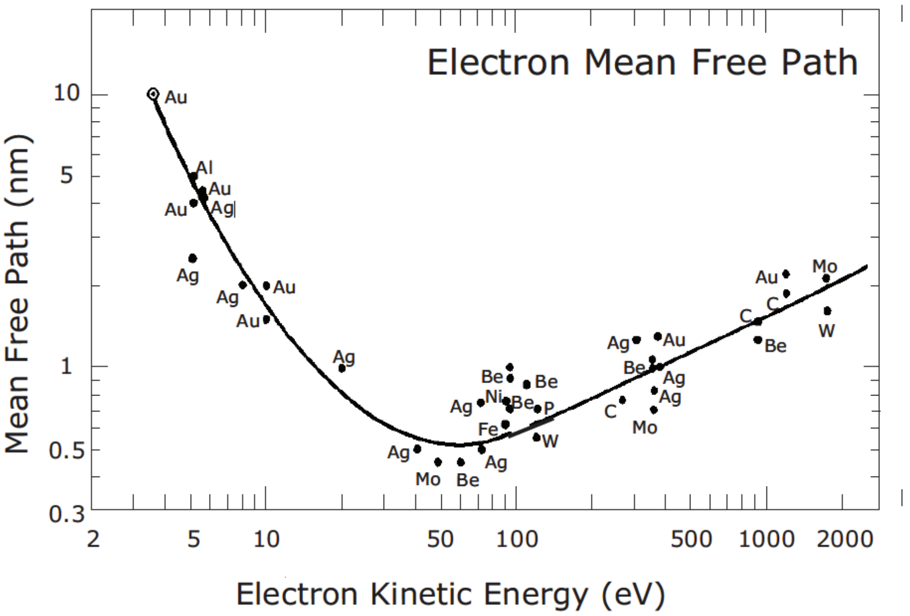

Figure 6.1: The universal curve for the electron mean free path as a function of the kinetic energy of the electrons. The surface sensitivity of electron based methods can be understood from the short mean free path of electrons with kinetic energy in the energy range 10-1000 eV. Image adapted from [127].

forced to turn they emit intense X-ray beams called synchrotron radiation. The synchrotron radiation is emitted along the curved orbit of a bending magnet and at those velocities the angular distribution of the radiation is mainly in the forward direction [128]. Synchrotron radiation has several advantages compared to the conventional laboratory X-ray sources. Higher intensity, brilliance (the number of photons per unit time and solid angle) and tunability (from IR to hard X-rays), high degree of polarization, time resolution (radiation is emitted in short pulses with high frequency) are the most important benefits. By the use of insertion devices such as wigglers and undulators, the light intensity can be increased and better performance can be achieved, leading to the so-called third generation synchrotron radiation sources.

6.3 X-ray Photoelectron Spectroscopy

One of the most widely used techniques to investigate the chemical composition of surfaces is X-ray Photoelectron Spectroscopy (XPS). It is based on the photoelectric effect, where light ionizes the atoms in the sample, detected by Hertz in 1887 [129] and explained by A. Einstein in 1905 [130]. Professor K. Sigbahn and his collaborators from Uppsala developed the technique in 1950s for which he was awarded the Nobel Prize in 1981 [131].

A schematic representation of the principle is shown in Fig. 6.2. It can be seen as a three step process:

- Absorption of X-rays and ionization;
- Response of the atom and creation of a photoelectron;
- Transport of the photoelectron to the surface.

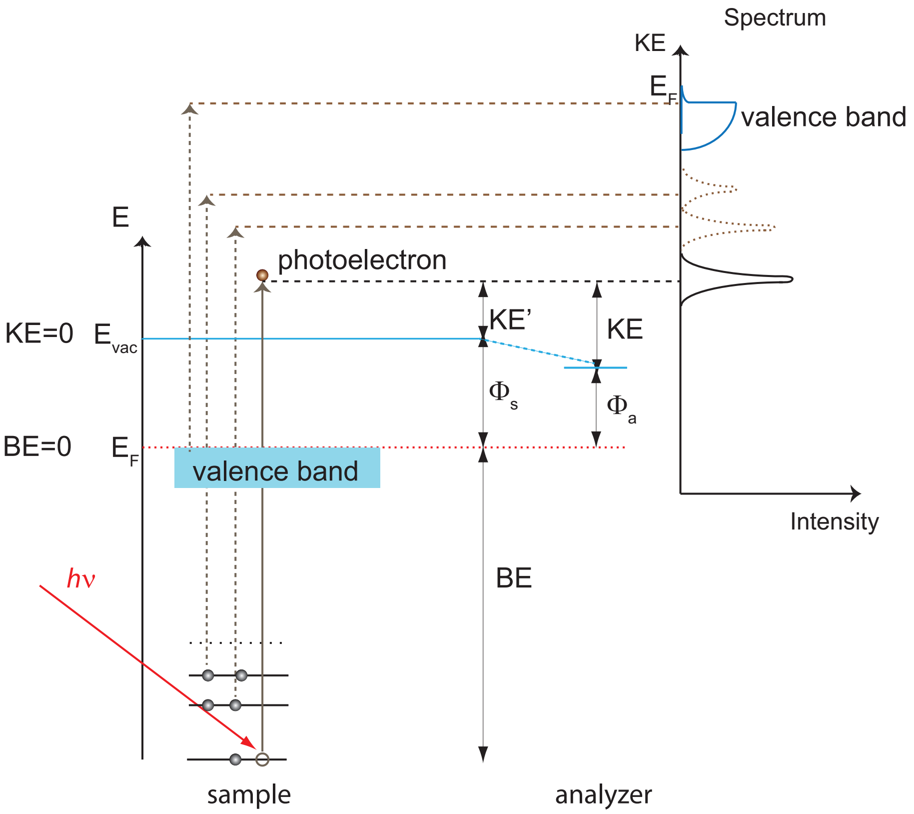

Figure 6.2: Relation between the energy levels in a solid and the electron energy distribution produced by photons of energy $h\nu$. The irradiation of the sample by photons leads to the emission of core and valence electrons into the vacuum. The sample is in electrical contact with the analyzer and their Fermi levels are aligned. A XP spectrum is produced by plotting the number of collected electrons as a function of their kinetic energy. Narrow peaks are produced by the core-levels due to their localized nature.

The emitted photoelectrons are collected and their kinetic energy (*KE*) is analyzed to produce a spectrum of emission intensity versus binding energy (*BE*). Each element has a characteristic electron binding energy that will give rise to a characteristic set of peaks in the photoelectron spectrum [132]. Tabulated values can be found for the binding energies for different elements [133, 134]. When core-levels are investigated with high energy resolution, the technique is often referred to as High Resolution Core-Level Spectroscopy (HRCLS).

Using the energy conservation principle the kinetic energy of the emitted photoelectrons can be written as:

$$KE' = h\nu - (BE + \Phi_s), \tag{6.1}$$

where BE is the binding energy of the electron measured with respect to the Fermi level, and Φ_s is the work function of the sample. The work function represents the minimum energy that is necessary to remove an electron from the material. As discussed below, an electron energy analyzer is used to measure the kinetic energy of the emitted photoelectrons. The sample (conducting) and the spectrometer are in electrical contact so their Fermi levels will align (see Fig. 6.2). Then, the work function of the analyzer, Φ_a, replaces the work function of the sample in equation (6.1) above and the total kinetic energy of the photoelectrons measured by the analyzer will be:

$$KE = h\nu - (BE + \Phi_a). \tag{6.2}$$

When the photoelectrons have left the sample they are collected with a hemispherical electron energy analyzer consisting of an electrostatic lens system, two hemispheres, a microchannel plate detector and a phosphorous screen as illustrated in Fig. 6.3 [135, 136, 137]. The function of the electrostatic lens system is to to accelerate/decelerate electrons to a chosen pass energy (E_p) and to focus the electrons to the entrance slit of the hemispherical system. After the electrostatic lens system, the electrons pass through two concentric conducting hemispheres with a potential difference between them (a positive potential on the inner hemisphere thus attracting the electrons and a negative, repulsive potential on the outer one) [132]. This potential difference separates electrons allowing only the electrons with approximately E_p to pass through to the micro channel plate (MCP) detector and the electric field in between the hemispheres bends the electron trajectory. Electrons with kinetic energy less than E_p are attracted by the inner positive hemisphere and are neutralized. Electrons with kinetic energy higher than E_p hit the outer hemisphere and are also lost. The signal is multiplied in the MCP detector and is converted into visible light on the phosphorus screen and later recorded by a charge-coupled device (CCD) camera. During an experiment the value for the pass energy is kept constant and the acceleration-retardation voltage is swept over the desired range which allows electrons of different kinetic energies to reach the detector.

As not only electrons with energy E_p will reach to the detector, but rather a broader energy interval $E_p \pm \Delta E$ (due to the finite size of the entrance slit width), it is useful to introduce the energy resolution of energy analyzer, which is given by:

$$\Delta E(eV) = \frac{E_p s}{2R} + \frac{\alpha^2 E_p}{4}, \tag{6.3}$$

where s is the analyzer slit width, α the average angular electron distribution, and R is the analyzer mean radius (200 mm for the Scienta SES200 used at beamline I311 at MAX IV). The energy resolution can therefore be increased by either increasing the hemisphere radius or

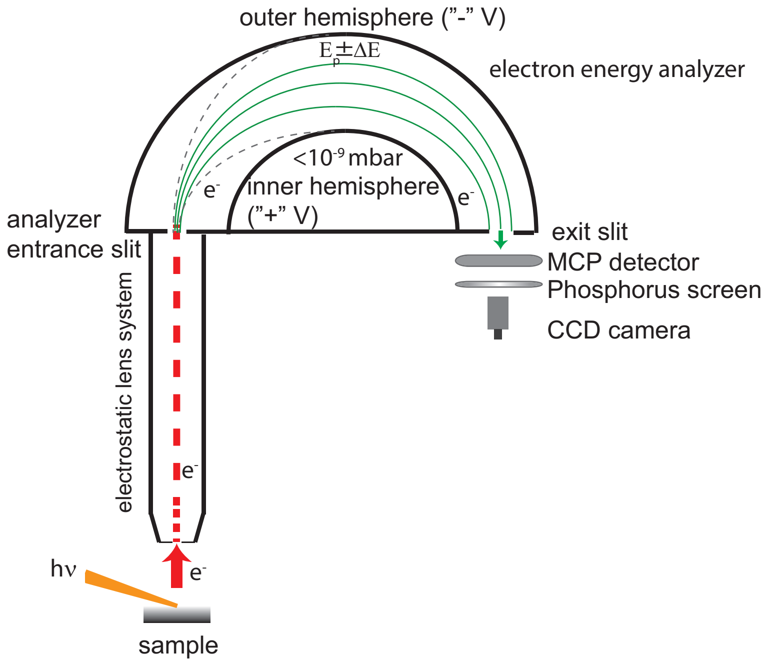

Figure 6.3: Schematic representation of the hemispherical energy analyzer. The electrostatic lens system accelerates/decelerates the electrons to the pass energy E_p and focuses them onto the entrance slit. After passing through the gap between the two hemisphere, the electrons are detected with the MCP detector and the signal intensity is measured by the phosphorus screen and a CCD camera.

decreasing the pass energy. Still low pass energy values decreases the electron transmission as it is considerable more difficult to focus the low energy electrons on the entrance slit of the analyzer and therefore a reasonable balance between the pass energy and the count rate should be chosen during the experiments.

6.3.1 Line Shape Decomposition

In order to obtain quantitative details from a core-level spectrum, a decomposition is often required as important information is contained in the shape of a spectrum. There are various factors that contribute to the shape of a core-level photoemission peak. For solids, a Gaussian distribution accounts for the broadening of the line due to the experimental resolution (such as monochromator and analyzer), excitations of quantized vibrations in the solid lattice (phonons) and disorder [138], while the lifetime broadening has a Lorentzian shape [139]. Each core-level has an intrinsic width due to the finite lifetime of the hole state according to Heisenberg's uncertainty principle $\Delta E = \hbar/\Delta t$. The relation between the intensity and the energy is given by the following relations:

$$I_L(E) = I_0 \frac{(\gamma/2)^2}{(E_0 - E)^2 + \gamma^2/4} \tag{6.4}$$

$$I_G(E) = I_0 exp\left(-\frac{\ln 2(E_0 - E)^2}{\sigma^2/4}\right), \tag{6.5}$$

where the indices L and G refer to Lorentzian and Gaussian, respectively, γ is the Lorentzian full width at half maximum (fwhm), σ the Gaussian fwhm, E is the kinetic energy of the photoelectrons and E_0 the energy position for the maximum intensity I_0 of the peak. In metals, an asymmetric tail to the main peak on the high binding energy side is often observed due to the fact that the conduction band is situated directly above the Fermi level, therefore different final states are easily populated with small energy difference [140].

Doniach and Šunijć [141] performed an analysis for the photoemission line shapes resulting in a profile given by the expression:

$$f(E) = \frac{\Gamma(1-\alpha)}{(\gamma^2 + E^2)^{(1-\alpha)/2}}\cos\left(\frac{\pi\alpha}{2} + \theta(E)\right), \tag{6.6}$$

with

$$\theta(E) = (1-\alpha)\arctan(E/\gamma), \tag{6.7}$$

where α is the asymmetry parameter, Γ is the Gamma function, 2γ is the FWHM of the Lorentzian and the cosine term approximates a step function as α increases. The Doniach Šunijć line shape has a Lorentzian shape and at the same time takes the asymmetry on the high binding energy side into account. In this work, the Doniach Šunijć line shape is convoluted with a Gaussian to account for the instrumental resolution, vibrations and disorder.

The decomposition of spectra in this work was performed using the FitXPS program by David Adams [142]. For the analysis of the recorded photoemission spectra a deconvolution procedure involving a Doniach-Šunijć line shape convoluted with a Gaussian was used.

During the photoemission process different electron energy loss processes may occur which will be observed as broad features and higher background on the high binding energy side of the peak [143]. The photoelectron is likely to experience scattering due to electron-electron or electron-phonon interaction. The inelastically scattered electrons experience an energy loss process and will contribute to the increased background on the high binding energy side of the main peak and are called secondary electrons. The overall signal from the background can be quite complicated as will be discussed more below and it has to be taken into account for correct analysis of the photoemission peaks. When the XPS is used for qualitative purposes, i.e. if one is only interested in the line positions, the background subtraction is not very important. For quantitative purposes, the background shape could have a significant importance. Advanced models exist for background subtraction [144, 145], but in this work, simple models such as linear or polynomial backgrounds have given satisfactory results.

The peak area can also be used to determine the concentration of a specific element in a sample. As different factors contribute to the area of a core-level peak a more easy task is to determine the relative concentrations of the constituents in a sample by comparing the relative peak areas.

Some important concepts of XPS that were encounted in the present work are described below. It is beyond the scope of this thesis to describe XPS in detail and for further reading the reader is referred to for example reference [140].

6.3.2 Chemical shifts in core-levels

The core-level binding energy can be slightly altered by the chemical state of the emitting atom producing a so-called "chemical shift" which can be used to fingerprint different species present on the surface. The number of components in a core-level spectrum corresponds to the number of chemically different atoms (see the example below on the photoemission spectrum from oxidized Ag). Therefore the name ESCA (Electron Spectroscopy for Chemical Analysis) is also used for this technique [146]. The binding energy shifts are often correlated to the charge on an atom; the higher the positive charge on an ion in a molecule is, the higher the binding energy shift.

A special case of a chemical shift is the surface core-level shift. XPS probes mostly the electrons near the surface since the escape depth of the electrons is small and it can therefore be used to analyse the adsorbed species on the surface [147]. The surface layer has a different environment as compared to the bulk leading to a shift in the binding energy. Surface core-level shifts have been observed for different transition metals such as Rh(111), Rh(110), Pd(111), Pd(110), Ag(111) [148]. As an example, the deconvolution of the Al 2p core-level spectrum from the clean NiAl(110) surface is shown in Fig. 6.4. The spectrum is decomposed into two components, each of them split by the spin-orbit [140] by 0.4 eV and with an intensity ratio of 1:2. A peak is observed at lower binding energy relative to the bulk Al 2p component at 72.5 eV (and 72.9 eV, respectively). The surface Al atoms have a different chemical surrounding as compared to the bulk Al atoms. By performing energy dependent measurements to vary the kinetic energy of the photoelectrons, the lower binding energy component can be assigned to the surface Al atoms [48].

The surface core-level shifts can also be verified by gas adsorption, which decreases and shifts the intensity of the surface core-level components while leaving the bulk component largely unaltered. This has been used in the gas adsorption on PdO(101) studies presented in Papers VII-IX.

Because of its sensitivity to the chemical surroundings of the photoelectron emitting atoms, XPS is suitable for studying the oxidation of metals. When oxides are formed, electrons are transferred from the metal atoms to the oxygen atoms. This will create an excess of positive

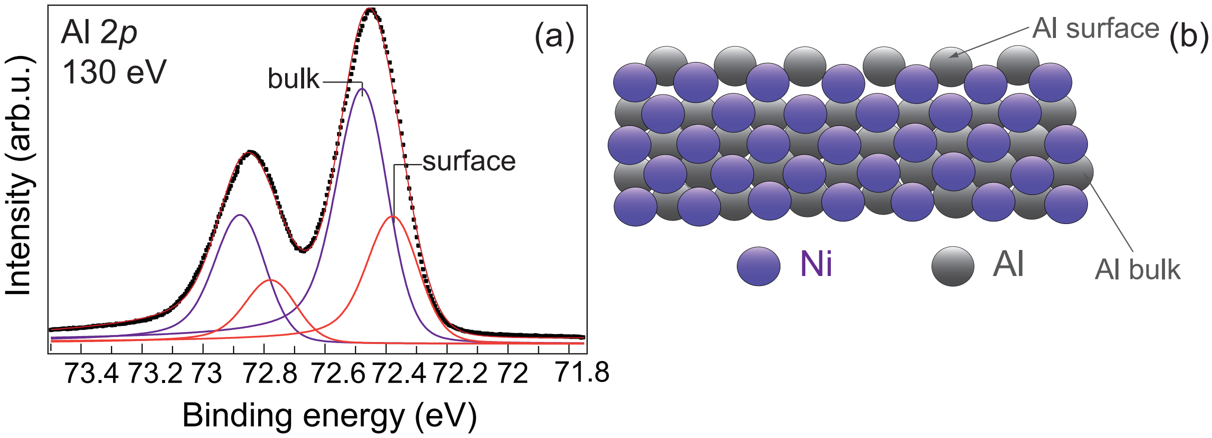

Figure 6.4: (a) The Al 2p spectrum from the clean NiAl(110) surface showing a surface core-level shift for the Al atoms in NiAl(110) of -0.1 eV (red components). (b) A side view of the NiAl(110) showing the surface and the bulk atoms.

charges on the metal atoms in the oxide as compared to the metal atoms in the bulk and therefore the remaining electrons are more strongly bonded in the atom. Therefore, more energy will be required to remove an electron from the metal core-level in the oxide as compared to in the metallic bulk. That is why we usually see the oxide components shifted to higher binding energy. An example is shown in Fig. 6.5 (b), where the X-ray photoelectron spectrum for the Al 2p from an oxidized NiAl(110) surface is shown. Upon oxidation, a broad feature appears on the high binding energy side of the Al 2p level and is assigned to electron emission from the oxidized aluminum atoms (Paper I).

The above purely electrostatic argumentation when Al is oxidized is not entirely true, since the binding energy is defined as the difference between the initial and the final state. Thus, the effect on the kinetic energy of the photoelectron due to the presence of the core hole is not taken into account. It is therefore important to distinguish between initial state effects (like charge transfer) and final state effects (like electron screening) when making an interpretation of a core-level binding energy shift [143]. After the photoemission process the remaining electrons will rearrange in order to lower the total energy of the whole system by screening the positive core hole. In a metal, a large amount of free electrons is available to screen the core hole. Although most shifts may be understood as the above initial state argument, a proper interpretation should be done using *ab initio* calculations which includes a final state with a core hole. In this thesis, all calculations are including a final state with a core hole. The DFT calculations indicate that although core-level shifts can give important information on surface reactivity changes, final state contributions can be significant.

A good example of the importance of proper theoretical support is the oxidation of Ag. It can be observed that the core-levels of the oxidized Ag are shifted to lower binding energies

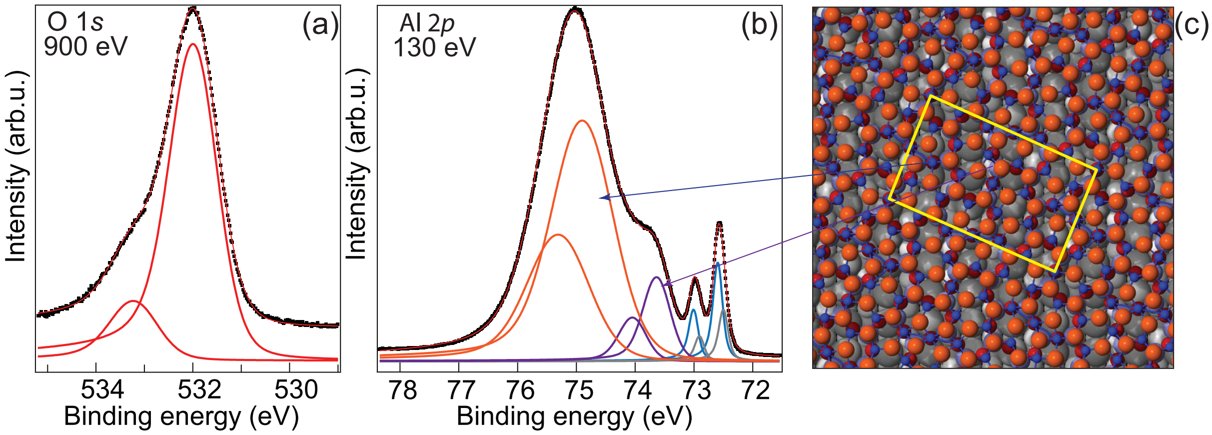

Figure 6.5: High resolution core-level spectra from the ultrathin aluminum oxide on NiAl(110). The O 1s spectrum (a) is recorded at 900 eV and the emission is broad with a shoulder on the high binding energy side. The Al 2p spectrum (b) recorded at 130 eV is decomposed into 4 components, each with 0.4 eV spin-orbit split and with a ratio of 1:2. The structural model of the ultrathin aluminum oxide grown on NiAl(110) is presented in (c). The Al (O) atoms are indicated by the blue (orange) spheres and the unit cell is indicated by the yellow rectangle.

(see Fig. 6.6) relative to the Ag 3d bulk binding energy in contrast to other transition metals (Pd, Pt, Rh) [148]. In the case of Ag, although a clear charge transfer from the metal to the oxygen is observed theoretically, the core-level binding energy is not affected, and the shift towards lower binding energy can instead be described by the details of the screening of the core hole, explaining the anomalous Ag 3d shift as discussed in Paper III .

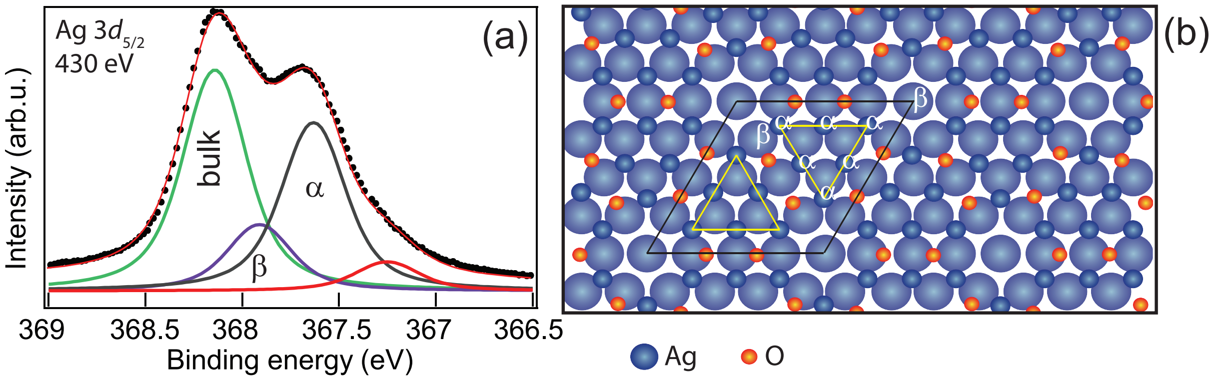

Figure 6.6: (a) High resolution core-level spectrum from the $p(4\times4)$ grown on Ag(111). The Ag 3$d_{5/2}$ spectrum recorded at normal emission with hν=430 eV is decomposed into four components assigned as indicated in the figure. (b) The structural model of the $p(4\times4)$-O/Ag(111). The Ag (O) atoms are represented by the blue (red) spheres. The lighter blue atoms represent the Ag atoms in the topmost Ag(111) layer.

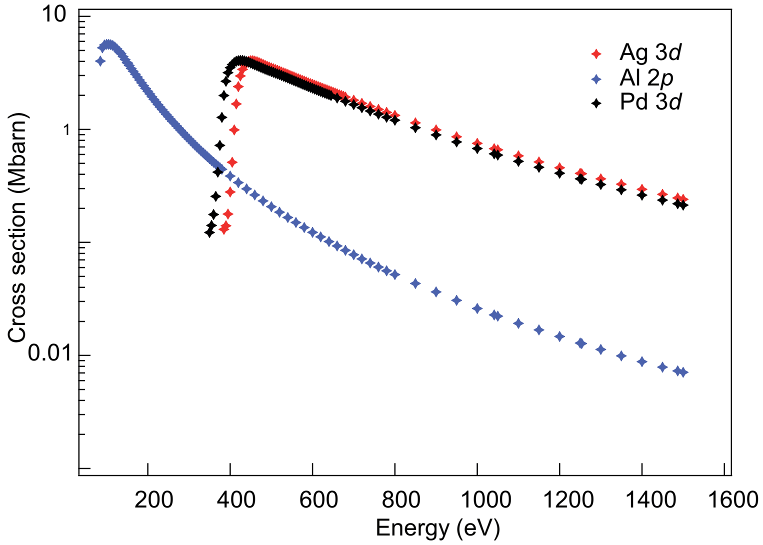

Figure 6.7: The cross section for Ag 3*d* (red), Al 2*p* (blue) and Pd 3*d* (black) levels at different photon energies. Recreated from [150].

6.3.3 Photoionization Cross Sections

The cross section represents the probability of the electron to be emitted from its electronic state by a photon. When choosing the photon energy for an experiment one should choose a photon energy which will generate a high cross section to produce a high intensity in the recorded spectrum. Tabulated values for the photoionization cross section for different elements can be found for example in references [149, 150]. The cross section for Al 2*p*, Ag 3*d* and Pd 3*d* levels are shown in Fig. 6.7.

6.3.4 Vibrational effects

The photoemission process may lead to the excitation of vibrational modes in the final state of, for example, a chemisorbed molecule (see Paper IX). The charge transfer between the substrate and adsorbate leads to changes in the internal molecular bonds, as well as formation of bonds between the molecule and the surface that can induce some variation of the bond strength and the nuclei will have to find new equilibrium positions, inducing some vibrations. Due to the vibrations in the final (excited) state, a vibrational structure can arise in the photoemission spectra. The study in detail of the vibrational effects with XPS was not the scope of this thesis and for further reading the interested reader is referred to for example references [151, 152].

6.3.5 Photoelectron Diffraction

The photoelectron may be elastically scattered by other atoms or molecules leading to intensity modulations as a function of electron wavelength and/or crystal orientation [153]. If the wavelength of these electrons is of the order of atomic distances, the elastically scattered beams can interfere with each other and with the primary beam giving rise to interference patterns. The interference of the scattered and directly emitted parts of the electron waves is determined by the position of the emitting atoms relative to the surrounding atoms. At certain directions in space and/or for certain kinetic energies constructive interference between the electron wavefunctions enhances the photoemission intensity, whereas in other directions the interference lowers it. Therefore the photoelectron diffraction produces core-level intensity variations as a function of detection angle and photon energy. Photoelectron diffraction effects implies that it is not always straightforward to use the core-level intensity to measure the adsorbate coverage [154].

6.3.6 MAX-lab and beamline I311

The XPS measurements presented in this work were performed at beamline I311 at the MAX IV Laboratory in Lund [155]. At the moment the MAX IV Laboratory comprises both MAX-lab and the MAX IV project [156]. MAX-lab contains three particle accelerators, The MAX I, MAX II and MAX III rings with energies of 550 MeV, 1500 MeV and 700 MeV, respectively.

Beamline I311, at the MAX II ring is described in detail in reference [157]. The lay-out of the beamline I311 is shown in Fig. 6.8. The main components are mirrors used to direct and focus the light and a monochromator, which is used to extract one wavelength from the incident light resulting in X-rays with a defined energy. The light originating from an undulator with a 54.4 mm period and a minimum gap of 17 mm has energies ranging from 43 to 1500 eV (soft X-rays) [158]. The undulator radiation spectrum consists of a series of sharp peaks (harmonics) and by tuning the undulator gap one can change the position of the maximum intensity for a particular harmonic. The photons produced by the undulator are then collected by a focusing mirror and directed into the monochromator, which houses 3 gratings where the first two are used for the spectroscopy station allowing to select the photon energy. The monochromator's function is to extract a single wavelength from the continuous spectrum by the use of a grating. A mirror is then used to focus the light on the exit slit. The monochromator exit slit is very important for the photon energy resolution as it selects only a part of the photon bandwidth. After a specific wavelength for the light is chosen, the light is further focused on the sample. The spot size of the light on the sample is 500 μm(h)×100μm(v). Two experimental end-stations are attached to beamline I311: the Spectroscopy station (XPS) and the Photo-Emission Electron Microscopy (PEEM) station. The photon energy resolution of beamline I311 depends on the photon energy, monochromator

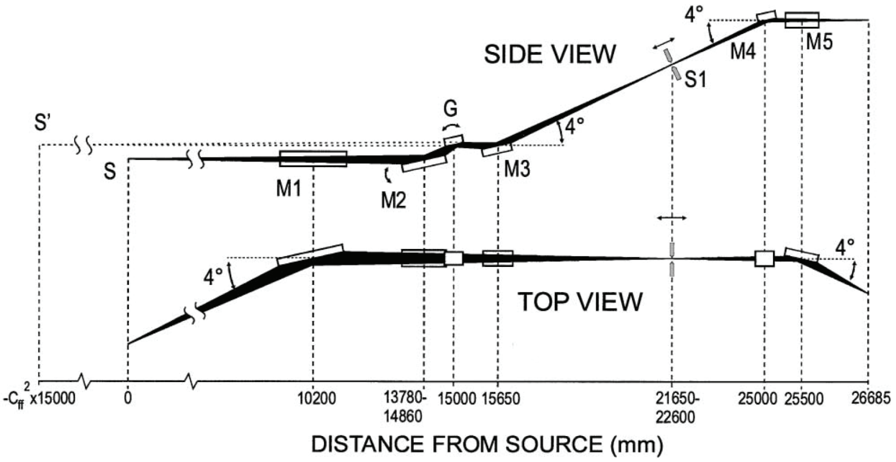

Figure 6.8: Schematic representation of beamline I311 at MAX-lab. *S* represents the electrons source, *G* the monochromator grating, *S*1 the adjustable monochromator exit slit and *M1-M5* represent the mirrors used to direct/focus the light. Adapted from [157].

slit and undulator gap and it usually has values of a few tens of meV, hence the high resolution of this beamline.

6.4 High Pressure X-ray Photoelectron Spectroscopy

In order to understand the interaction of a catalyst surface with the reactants under conditions close to real working conditions, *in situ* measurements are desired. Because the electrons are highly scattered by gas molecules, XPS is usually performed in UHV. To perform XPS measurements at higher pressures than UHV, the attenuation of the electrons has to be kept at minimum by reducing the path of the electrons in the high pressure region. This can be achieved by placing the sample close to a differentially pumped aperture, behind which the pressure drops by several orders of magnitude. This basic concept was developed by Siegbahn *et al.* in the 1960s [159] and later by other groups [160, 161, 162, 163]. The new generation of High Pressure X-ray Photoelectron Spectroscopy (HP-XPS) enhance the transmission by focusing the electrons in each differential pumping stage, allowing for XPS to be used at pressures up to about 10 mbar [35, 36].

A schematic representation is shown in Fig. 6.9. The sample is placed in a high-pressure chamber equipped with a X-ray transparent window to allow X-rays to pass through. To enhance transmission, a differential pumping system is used in close proximity of the sample. The photoelectrons emitted from the surface of the sample, where the pressure can be a few mbar, will travel along the differential pumping system situated only a few mm from the sample surface. In practice it has been observed that the optimum sample distance is a few times the aperture diameter ($x \approx 2d$ in our experiments, where d is the aperture diameter).

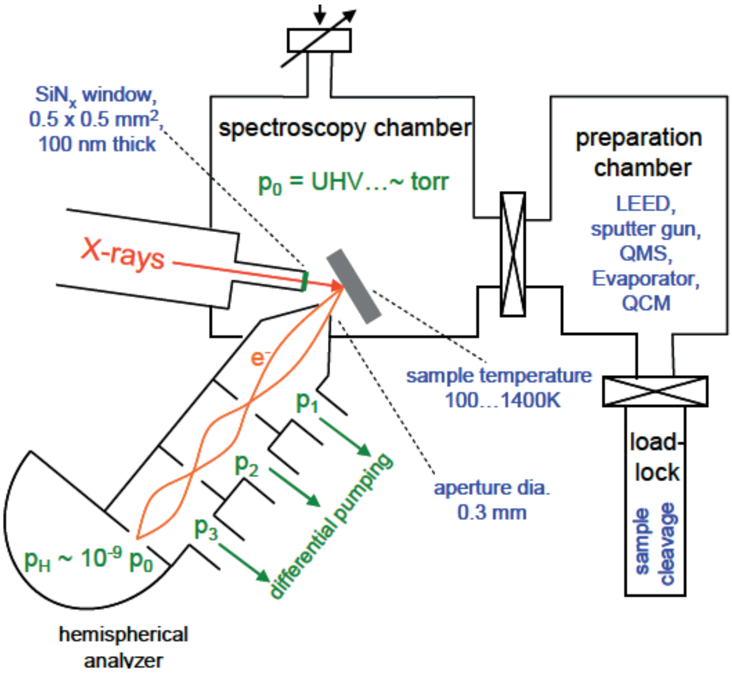

Figure 6.9: Schematic representation of a HP-XPS setup. Adapted from [164].

Several additional pumping stages are necessary to decrease the pressure from 10 mbar to UHV in the electron detector where the pressure decreases to about 10^{-9} mbar. With the use of electrostatic lenses the electrons can be focused into the different apertures, enhancing transmission.

In some experiments, it is useful to correlate the chemical nature of the catalyst surface with its catalytic activity. This can be achieved either by the use of a mass spectrometer or, when the gas pressure is above approximately 0.05 mbar (depends on the cross-section of the element), by direct determination of the gas-phase composition from the XPS spectra. Since the incident X-rays penetrate also part of the gas in front of the sample and can ionize the molecules located close to the sample, gas-phase XPS peaks are observed together with the surface peaks with a few eV shift in BE [159].

A general problem with the gas phase peaks is to determine their absolute binding energies. As the gas phase molecules do not have a Fermi level, they should be calibrated to the vacuum level of the gas. The measurement of the vacuum level is difficult as the vacuum level will continuously change with the distance to the sample and therefore the calibration of the gas phase peaks is done to the Fermi level of the sample. This implies that a change in the sample work function will shift the binding energy of the gas phase peaks.

An example to illustrate HP-XPS is shown in Fig. 6.10. In this figure, a continuous set of O 1*s* scans recorded during the CH_4 oxidation reaction over a Pd(100) surface in the presence of

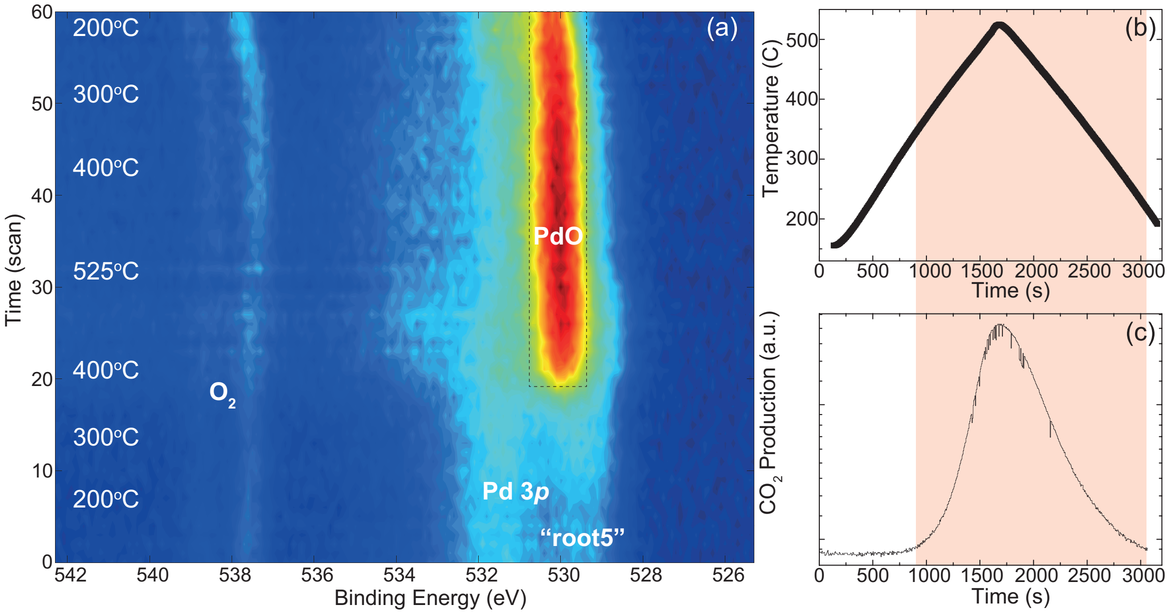

Figure 6.10: (a) O 1*s* region during methane oxidation in a gas mixture of 0.5 mbar O_2 and 0.2 mbar CH_4. The temperature of the Pd(100) sample was ramped up to 525° C and down to 170° C during the experiment as illustrated in (b). The CO_2 production as a function of time is also shown.

0.5 mbar O_2 and 0.2 mbar CH_4 is shown. The O 1*s* region reveals the surface adsorbates and the composition of the gas containing oxygen above the surface. A mass spectrometer was used to record the composition of the gases in the chamber. The reaction rate is observed to correlate with the surface oxidation states. The reaction is further described in Paper XII.

6.4.1 ALS and beamline 9.3.2

Most of the HP-XPS measurements presented in this thesis were performed at beamline 9.3.2 at the Advanced Light Source in Berkeley, CA [165]. During operation the beam current in the ring has a constant value of 500 mA and energy of 1.9 GeV. The X-rays originating from a bending magnet with photon energies between 30-850 eV, will hit the sample and the emitted photoelectrons will be detected by a Scienta 4000R-Hipp analyzer. The spot size on the sample is rather large (about 1mm×1mm) therefore a general information from a large surface area is obtained. A small cone aperture (0.8 mm) minimizes the pumping in front of the sample and a 100 nm thick SiN window separates the X-rays source from the high pressure cell.

6.5 Diffraction

Diffraction is the most important method for structure determinations at the atomic level in many fields of science [166, 167, 168]. In surface science, Low Energy Electron Diffraction (LEED) is mainly used, where electrons with low kinetic energy (20-300 eV) are used to study the surface structure of crystalline materials [132]. It is a surface sensitive technique due to the strong interaction of electrons with matter as illustrated in Fig. 6.1. LEED is based on the fact that electrons can be described as waves and they will be scattered by a regular array of atoms due to the periodic crystal structure. To perform an *in situ* diffraction experiment, the use of electrons is not a good choice as they will be highly scattered by the gas molecules surrounding the sample. Due to the low interaction of X-rays with matter, the X-rays are almost unaffected by a gas atmosphere surrounding a sample and, therefore, can be used to study the structure of a material at atmospheric ambient conditions. When a surface is studied with the help of X-ray diffraction the technique is referred to as Surface X-ray Diffraction (SXRD). However, since X-rays penetrate deeply inside the crystal, a large contribution to the XRD signal comes from the bulk. The surface sensitivity can be enhanced using grazing incidence for the incident X-ray beam and the penetration of the X-rays can be reduced from several μm to about 50 Å. Since the refractive index of X-rays in solids is less than unity, the X-ray beam will be totally reflected for small glancing angles (0.1- 0.5°) [169]. The use of synchrotron radiation as an X-ray source gives increased intensity of the otherwise weak surface scattering signals.

One of the fundamental properties of waves is that two waves can interfere with each other if they are in the same spatial region. If the two waves are in phase they interfere constructively and if they are out of phase they will interfere destructively. When a wave interacts with a set of periodically arranged objects, it may be scattered in different directions and the scattered waves can interfere with each other. This process of interference caused by a set of objects in the path of a beam is called diffraction and it will occur when the wavelength of the incident beam is shorter than the distance between the objects. By analyzing the scattered beams information can be obtained on the spacing between the objects and the periodic arrangement of the objects.

During a typical diffraction experiment a crystal is illuminated by some kind of waves (X-rays or electrons in this work), which are then scattered by the atoms in the crystal lattice. In certain directions, the beams scattered from different atoms will be in phase and interfere constructively. As the atoms are arranged in a periodic array, the scattered beams will create an interference pattern. There are two major ways to describe the condition for constructive interference, introduced by Laue and Bragg, respectively. Fig. 6.11 illustrates the Bragg formulation, where two beams are reflected, according to the usual law of reflection, by two different atomic planes. The beam reflected by the lower plane takes a longer path than

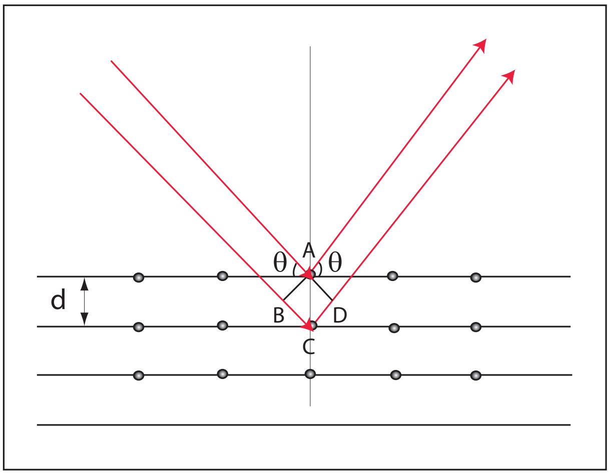

Figure 6.11: Bragg diffraction geometry. When two beams of the same wavelength are incident on a crystalline solid they will be scattered by the atoms. The lower beam will travel $2d\sin(\theta)$ more than the one above and constructive interference will occur when this extra length is equal to an integer multiple of wavelength.

the beam reflected by the outer plane. If this path difference equals an integer number of wavelengths, the outgoing beams are in phase and the interference is constructive. The path difference can be expressed as $PD = 2d\sin(\theta)$ and the condition for constructive interference as given by Bragg's law becomes:

$$n\lambda = 2d\sin(\theta), \tag{6.8}$$

where n is an integer, the order of the reflection, λ is the wavelength of the incident beam, d is the distance between parallel planes of atoms (the d-spacing), and θ is the angle of incidence of the beam.

The equivalent Laue formulation is illustrated in Fig. 6.12. A beam with wavelength λ and wavevector $\mathbf{k}$ ($|\mathbf{k}|=k=2\pi/\lambda$) is incident on two scatterers separated by a vector $\mathbf{R}$, that will scatter the beam in all directions. A scattered beam $\mathbf{k'}$ ($|\mathbf{k'}|=|\mathbf{k}|=k$ due to elastic scattering) will be observed along a certain direction if the beams scattered by different atoms interfere constructively. The condition for constructive interference is that the path difference between the rays scattered by each of the two ions is an integral number of wavelengths. The path difference can then be written as:

$$PD = s' + s = R\cos(\theta') + R\cos(\theta) = \frac{\mathbf{R}\cdot\mathbf{k'}}{k} - \frac{\mathbf{R}\cdot\mathbf{k}}{k} = \frac{\mathbf{R}\cdot\Delta\mathbf{k}}{k}, \tag{6.9}$$

where $\Delta\mathbf{k} = \mathbf{k'} - \mathbf{k}$ is the scattering vector, i.e., it expresses the change in direction due to the scattering. Another common notation for $\Delta\mathbf{k}$ is $\mathbf{q}$. The condition for constructive interference can be written as:

$$PD = n\lambda = \frac{n2\pi}{k}, \tag{6.10}$$

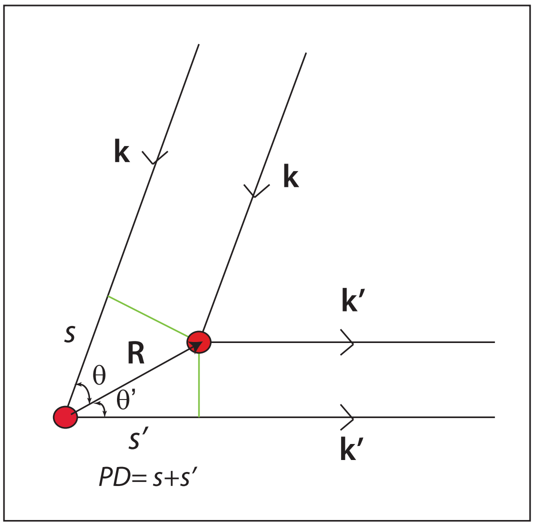

Figure 6.12: Scattering of a wave by two scatterers separated by a vector **R**. The two scattered beams may interfere constructively if the path difference between the two beams is a multiple of the wavelength.

or,

$$\mathbf{R}\cdot\Delta\mathbf{k} = 2\pi n. \tag{6.11}$$

where n is an integer. If we now consider an array of scatterers, with the lattice sites displaced by the Bravais lattice vectors $\mathbf{R}$=m$\mathbf{a}_1$+n$\mathbf{a}_2$+o$\mathbf{a}_3$, then the same condition for constructive interference should be fulfilled for all lattice vectors.

Reciprocal lattice

For every real lattice there is an equivalent reciprocal lattice, which is the Fourier transform of the real lattice. The reciprocal basis vectors ($\mathbf{b}_i$) may be written in terms of real space vectors ($\mathbf{a}_j$) as:

$$\mathbf{b}_i\cdot\mathbf{a}_j = \delta_{ij}2\pi, \tag{6.12}$$

where i, j=1,2,3. This implies that $\mathbf{b}_i$ is perpendicular to $\mathbf{a}_j$ if i≠j , and the length of $\mathbf{b}_i$ is $2\pi/|\mathbf{a}_i|$. Hence, a large distance in real space corresponds to a small distance in reciprocal space and vice versa. An arbitrary reciprocal lattice vector can be written as: $\mathbf{q}=r\mathbf{b}_1+s\mathbf{b}_2+t\mathbf{b}_3$, where r, s, t are integers. Returning to relation (6.12) and inserting $\Delta\mathbf{k}=(h\mathbf{b}_1+k\mathbf{b}_2+l\mathbf{b}_3)$ one obtains:

$$\mathbf{R}\cdot\Delta\mathbf{k} = (m_1\mathbf{a}_1+m_2\mathbf{a}_2+m_3\mathbf{a}_3)\cdot(h\mathbf{b}_1+k\mathbf{b}_2+l\mathbf{b}_3) = 2\pi(m_1h+m_2k+m_3l) = 2\pi n \tag{6.13}$$

Therefore, if h, k, l are integers, $\Delta\mathbf{k}$ is a reciprocal lattice vector. This gives the Laue condition that constructive interference will occur if the change in the wave vector $\Delta\mathbf{k}$ is a vector of the reciprocal lattice. Consequently, a diffraction experiment will give an image of the reciprocal lattice, which can be translated into the real lattice using relation (6.12).

The above discussion is valid for crystal structures with a single atom per lattice point, such as a simple cubic structure. For other structures, the internal structure of the unit cell will give rise to a variation of the peak intensity and some peaks will be completely cancelled. The intensity of the *(hkl)* peak will be proportional to the square of the so-called crystal structure factor F(hkl), which is given by the following formula:

$$F(hkl) = \sum_{\mathbf{m}} f_{\mathbf{m}} e^{(2\pi i (u_{\mathbf{m}} h + v_{\mathbf{m}} k + w_{\mathbf{m}} l))} \tag{6.14}$$

where $f_{\mathbf{m}}$ is the atomic scattering factor and *u, v, w* are the coefficients for the basis vectors of the atoms in the unit cell of the crystal structure and we are summing over all atoms **m** in the unit cell. Often some combinations of *h, k, l* will result in $F = 0$. For example in the case of an *fcc* structure, the values of *h, k* and *l* that will give a non-zero structure factor are all even or all odd.

6.5.1 Surface Diffraction

As mentioned above, in a diffraction experiment a map of the reciprocal lattice is produced that can later be translated into real lattice using relation (6.12). Returning to the Laue conditions $\mathbf{R} \cdot \Delta\mathbf{k} = 2\pi n$, where **R** a real space vector and n an integer, constructive interference is obtained when $\Delta\mathbf{k}$ is a reciprocal lattice vector. One can write a reciprocal lattice vector $\mathbf{q}=h\mathbf{b}_1 + k\mathbf{b}_2 + l\mathbf{b}_3$ being normal to the lattice plane *(hkl)*. For an infinite crystal the Laue conditions will be fulfilled for integer values of *h, k, l* and the scattered intensity will be maximum at $\mathbf{q}=h\mathbf{b}_1 + k\mathbf{b}_2 + l\mathbf{b}_3$. Therefore, the diffraction pattern will consist of a 3D reciprocal lattice of points with maximum intensity at the Bragg points (see Fig. 6.13 (a)). It is common to define the positions in reciprocal space by the values of *h, k, l,* which also define the axes of the reciprocal space.

For an isolated surface layer, the Laue conditions will only apply to the in-plane component of $\Delta\mathbf{k}$ parallel to the surface plane ($\Delta\mathbf{k}_{\parallel}$) and the conditions for constructive interference will be: $\Delta\mathbf{k}_{\parallel}=h\mathbf{b}_1 + k\mathbf{b}_2$, i.e. $\Delta\mathbf{k}_{\parallel}$ must be a reciprocal surface lattice vector. The diffraction conditions do not depend on *l* and the reciprocal lattice will consist of rods going through each *(hk)* point perpendicular to the surface (see Fig. 6.13 (b)), the so-called crystal truncation rods (CTRs). Adding layers to a single surface layer will result in the appearance of maxima at the bulk reflection positions along the CTRs. The more layers there are the stronger the bulk reflections will be. A truncated crystal can be seen as a half infinite crystal terminated by a surface layer. Therefore, when X-rays are employed, the diffraction intensity for a truncated crystal is still maximum at integer values of *l* but it will be smeared out in the direction perpendicular to the surface (=CTRs) as ilustrated in Fig. 6.13 (c). The measured intensity of these CTRs between the Bragg peaks contain information about atomic structure at the surface [39, 170].

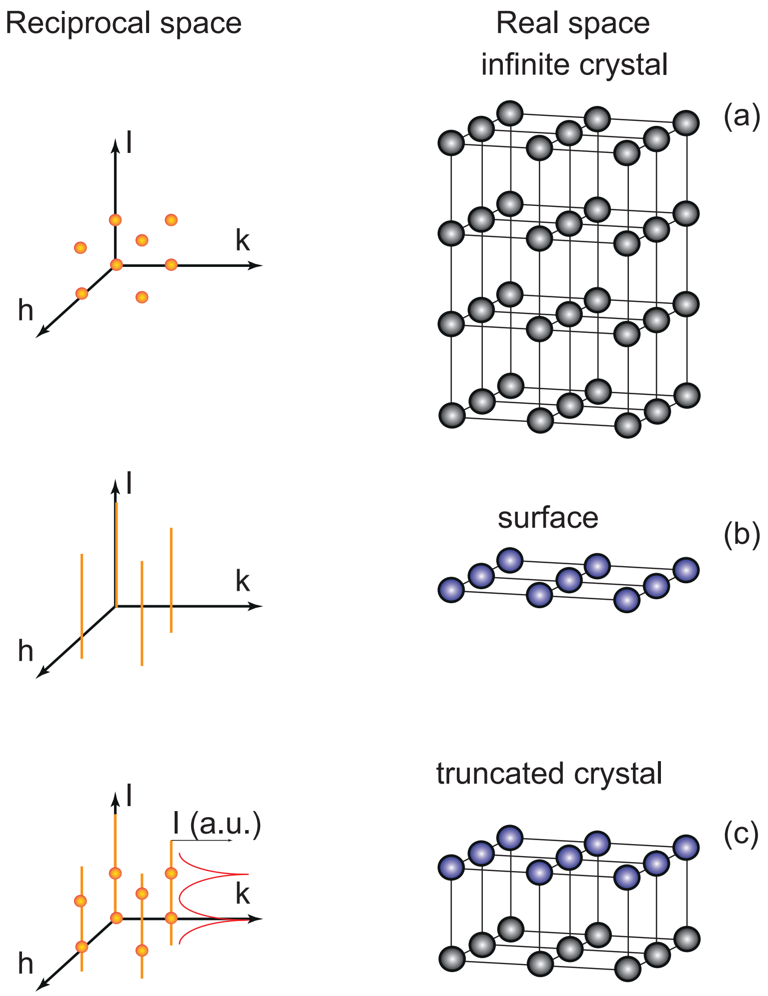

Figure 6.13: Representation of diffraction from (a) an infinite crystal, (b) an isolated surface layer and (c) a truncated crystal.

During surface reconstructions (see Chapter 3), the size of the unit cell in the surface plane will change. Therefore additional rods of scattered intensity will appear at non-integer values of h and k along the l direction, which are called superstructure rods.

6.5.2 Low energy electron diffraction

Diffraction of electrons was first observed in 1927 by Davisson and Germer [171]. The wavelength of electrons is related to their energy by:

$$\lambda = \frac{h}{\sqrt{2m_e E}}, \tag{6.15}$$

where h is the Planck constant, m_e is the electron mass and E is the kinetic energy of the electrons. Substituting the values for these parameters gives:

$$\lambda = \sqrt{\frac{150.4}{E}}, \tag{6.16}$$

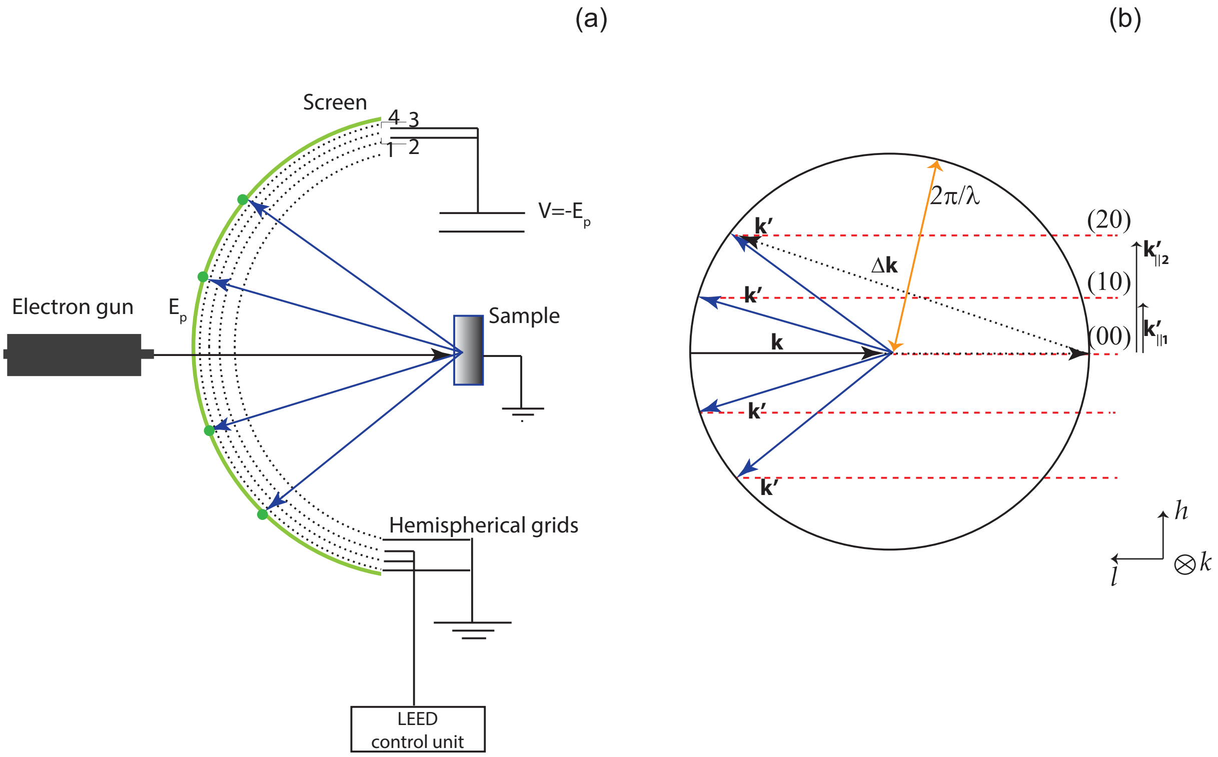

Figure 6.14: (a) Schematic representation of a four-grid LEED instrument. The incident electrons are scattered in different directions defined by **k'** and the elastically scattered electrons that undergo constructive interference will produce an intensity spot on the fluorescent screen representing a map of the reciprocal space as shown in (b). Diffraction will only occur for these directions of **k'** where the scattering vector Δ**k** is a reciprocal lattice vector.

where λ and E are measured in Å and eV respectively. Low energy electrons with a kinetic energy of 100 eV will give wavelengths in the order of 1 Å, comparable with the distance between atoms in a lattice.

Experimentally, a monoenergetic beam of electrons from an electron gun impinges on a sample surface, usually at normal incidence, as shown in Fig. 6.14 (a), where a commonly used LEED instrument is shown. The elastically scattered electrons create a diffraction pattern, which is collected on a fluorescent screen. The backscattered electrons will travel through a series of grids (1-4). The first and the fourth grid are grounded while the inner grids 2 and 3 serve as a cut-off filter and are set to a negative potential (V=-E_p), so that only elastically scattered electrons can pass. The screen is biased at a high positive voltage (about 3-5 kV) that accelerates the electrons to a sufficient kinetic energy to give rise to light emission from the coated fluorescent glass screen.

Returning to the reciprocal space, during a LEED experiment a wave vector **k** is coming in perpendicular to the surface and there may be different scattered waves **k'** going out of the surface. If one considers all possible directions the scattered electrons may have, a sphere may be constructed (Ewald sphere) with the radius $r = k = k'$ (Fig. 6.14 (b)). Since the incident wave vector is normal to the surface ($\mathbf{k}_{\parallel}$=0), the change in direction due to the scattering will be $\Delta\,\mathbf{k}_{\parallel}$=$\mathbf{k'}_{\parallel}$ and constructive interference will be obtained in directions where the projection of the scattered wave vector on the surface is a reciprocal lattice vector (Laue conditions). The higher the energy of the incoming electrons, the smaller the Ewald sphere will be and the closer the reflections to the (00) reflection.

LEED can be used to determine the structure of different crystalline substrates as well as structures induced by adsorbates. The spot positions are used to extract information about the periodicity of the adsorbate unit cell with respect to the substrate unit cell. By using relation (6.12), which relates the real space to the reciprocal space vectors, real space lattice distances may be obtained. It is important to note that the LEED pattern is an average over the area hit by the electrons, usually a few atomic layers. Therefore, defects in the surface layer and/or a specific layer can not be observed although the size of the spots often reflects the ordering on the surface.

As an example, Fig. 6.15 (a-b) shows the LEED patterns from a clean Pd(100) and the surface oxide $(\sqrt{5}\times\sqrt{5})$R27° grown on Pd(100) described in Chapter 3. As the surface lattice of Pd(100) is squared, so is the reciprocal lattice as indicated by the yellow lines in Fig. 6.15 (a). The model of the Pd(100) surface in (d) shows the basis vectors in real space. Pd has a *fcc* lattice structure with a cell parameter of a=3.89 Å. In the (100) orientation, the lattice unit cell is given by $a_1 = a_2 = a\sqrt{2}$=2.75 Å. Using relation (6.12) one can construct the reciprocal lattice of Pd(100) as illustrated in Fig. 6.15 (c) (squares). The length of the reciprocal lattice vectors will be b_1=b_2=$2\pi/a_1$. The $(\sqrt{5}\times\sqrt{5})$R27° spots are indicated by the small circles. The unit cell of the $(\sqrt{5}\times\sqrt{5})$R27° adsorbate structure in Fig. 6.15 (e-f) is $\sqrt{5}$ times as large in both directions as the unit cell of the substrate ($a_{s1} = a_{s2} = a_1\sqrt{5}$=6.149 Å). In the reciprocal lattice, and therefore in the LEED image, the unit cell of the $(\sqrt{5}\times\sqrt{5})$R27° structure will be $\sqrt{5}$ times smaller. In reciprocal space, the unit vectors of the surface oxide have directions as indicated in Fig. 6.15 (c) and have lengths of b_{s1}=b_{s2}=$2\pi/a_{s1}$. Since the rotation of the overlayer structure can be either +27° and -27° with respect to the substrate, different domains are formed. Fig. 6.15 (e-f) show two domains which are indicated in the LEED pattern by the orange and blue squares.

One can distinguish between qualitative and quantitative analysis in a LEED experiment. The qualitative analysis will, as described above, give the overall symmetry of the structure while the quantitative analysis can give the exact atomic positions of a surface. This is done by measuring the intensities of the diffraction beams as a function of the incident electron energy (I-V curves) and compare to theoretical curves calculated from proposed geometrical model. In this way, the exact geometrical structure can be obtained. Because of the strong

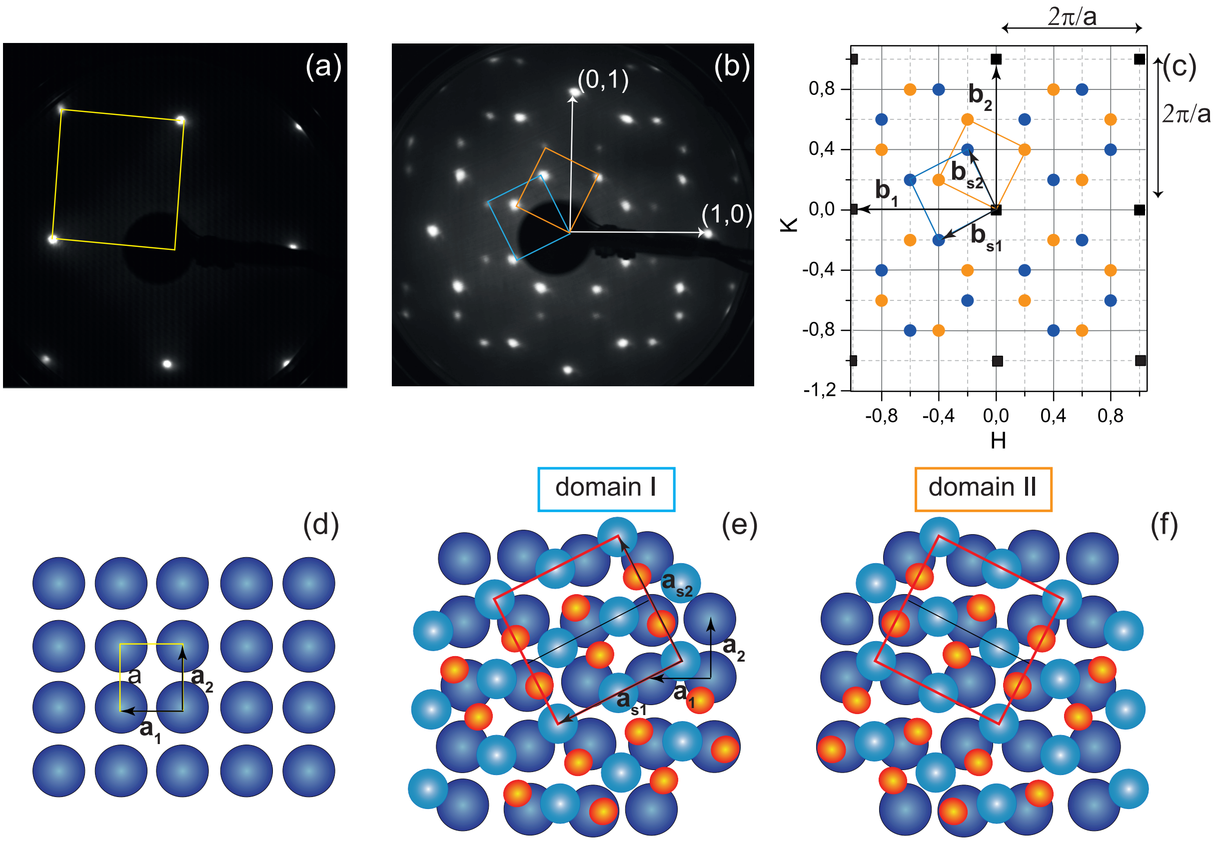

Figure 6.15: The LEED images of the Pd(100) (a) and the $(\sqrt{5} \times \sqrt{5})$R27° surface oxide (b) taken with an electron energy of 60 eV. The in-plane reciprocal space map of Pd(100) (squares) and $(\sqrt{5} \times \sqrt{5})$R27° (circles) is shown in (c). Structural model of the clean and the surface oxide with two different domains are illustrated in (d-f).

interaction of electrons with matter multiple scattering has to be included when performing quantitative LEED analysis. Only qualitative LEED measurements have been performed in the present work.

6.5.3 Surface X-ray Diffraction

As mentioned in section (6.5) the surface sensitivity in XRD can be enhanced using grazing incidence for the incident X-ray beam. Most importantly, however, SXRD gains surface sensitivity by scanning parts of the reciprocal space where surface signal is as high as possible and the bulk signal as low as possible, i.e. along the CTRs and superstructure rods. As the signal from the surface rods is only induced by scattering from atoms within the reconstructed part of the surface they are ideally suited for structural analysis of the surface.

One can also probe the growth of the surface ad-layers as illustrated by the oxidation of Pd(100) shown in Fig. 6.16. When the surface oxide grows thicker new points will appear in the out of plane direction (l). For the surface oxide some diffraction will occur at h=0.4

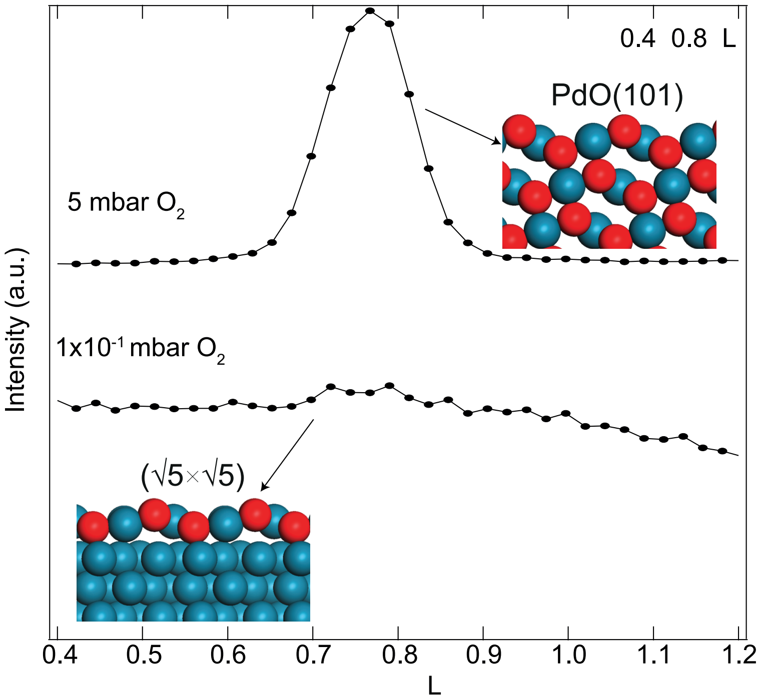

Figure 6.16: The out-of-plane diffraction from the (0.4, 0.8, l) with increasing l for the ($\sqrt{5} \times \sqrt{5}$)R27° (bottom line) and the PdO (upper line). The pattern from ($\sqrt{5} \times \sqrt{5}$)R27° reveals only a smooth change in the diffraction, while the thicker PdO results in a peak at l=0.74. Such difference allow us to separate between the two structures.

and k=0.8 as illustrated in Fig. 6.15 (b-c). Fig. 6.16 shows the out of plane CTRs (0.4, 0.8, l) with increasing l when the Pd(100) sample was exposed to 1×10^{-1} mbar O_2 (bottom) and 5 mbar O_2 at 550 K. The diffuse scattering from the ($\sqrt{5} \times \sqrt{5}$)R27° (bottom line) indicates one PdO layer, without peaks in l. As the oxide grows thicker the shape of the (0.4, 0.8, l) rod changes and a peak at l=0.74 is observed. This peak corresponds to a lattice constant of 0.526 Å, close to the c lattice constant of PdO (=5.34 Å) (see Chapter 3). This illustrates how SXRD can be used to distinguish between different structures. Recent improvements have made the distinction even faster by the use of a 2D detector that is able to take an image of the reciprocal space around a given h, k and l value instead of a scan [172].

The measured CTR and superstructure rod data can be compared to calculated structure factors using the software package ROD [173]. For this an initial guess of the surface structure is required, which may be obtained by other methods.

6.5.4 ESRF and beamline ID03

The surface X-ray diffraction measurements presented in this thesis were performed at the European Synchrotron Radiation Facility (ESRF) in Grenoble, France [174]. It is a third generation storage ring with a energy of 6 GeV. The beamline ID03 is an undulator beamline providing a uniform photon flux in the 5 to 30 keV energy range. The minimum beam size on the sample is $3\times2\ \mu m^2$. The beamline is dedicated to surface and interface structural studies [175, 176] allowing measurements under close to realistic operating conditions. Three different reactors are available for the users with pressure range from UHV to 3 bar and a 2D detector allowing for increased area detection of the reciprocal lattice for short exposure times (<1s/image).

6.6 Scanning Tunneling Microscopy

Scanning Tunneling Microscopy (STM) was developed in 1982 by Binning and Rohrer. For this they were awarded the Nobel Prize in 1986 [177]. Since then STM has attracted interest from researchers all over the world due to its ability to achieve atomic resolution. It is used to study the structure and topography of surfaces at the atomic level [178] by making electrons tunnel between a surface and a probe (tip).

The principle of STM is simple: an atomically-sharp probe (tip) is brought close (about 1 nm) to a conducting surface (sample) (see Fig. 6.17). The tip and the sample are in electrical contact and their Fermi levels are aligned. If a bias voltage (V) is applied between sample and tip, electrons will tunnel across the vacuum barrier giving rise to a tunneling current (I) which can be measured. Depending on the sign of the bias voltage, the current will flow either from the filled states in the sample to the empty states in the tip (negative bias voltage), or from the filled states in the tip to the empty states in the sample (positive bias voltage). In a quantum mechanical treatment the tunneling current is given as a function of distance d between the tip and the surface as [179]:

$$I(d) \propto e^{-ad\sqrt{\phi}} \tag{6.17}$$

where a is a constant and ϕ is the tunnel barrier height between the tip and the sample. The current is measured, and due to the exponential dependence, the tunneling current is very sensitive on the tip-sample separation. The tip is mounted on a piezoelectric tube (or a piezo-tripod, depending on the setup) which can expand or contract (about 1 Å per mV) in x, y, z directions by applying a voltage at its electrodes. Therefore, the position of the tip over the surface can be controlled with extremely high precision. As tunneling occurs when empty electron states of the surface overlap with filled states at the tip (or vice versa), an STM image reflects the electronic structure and not the atoms directly.

Two modes of operation can be employed during STM operation: the constant current and constant height mode. In the most commonly used mode, the constant current mode, the current is kept constant by varying the tip-sample separation with high precision in a feedback loop (using the z piezo). The tip is scanned over the surface using the xy piezoelectric

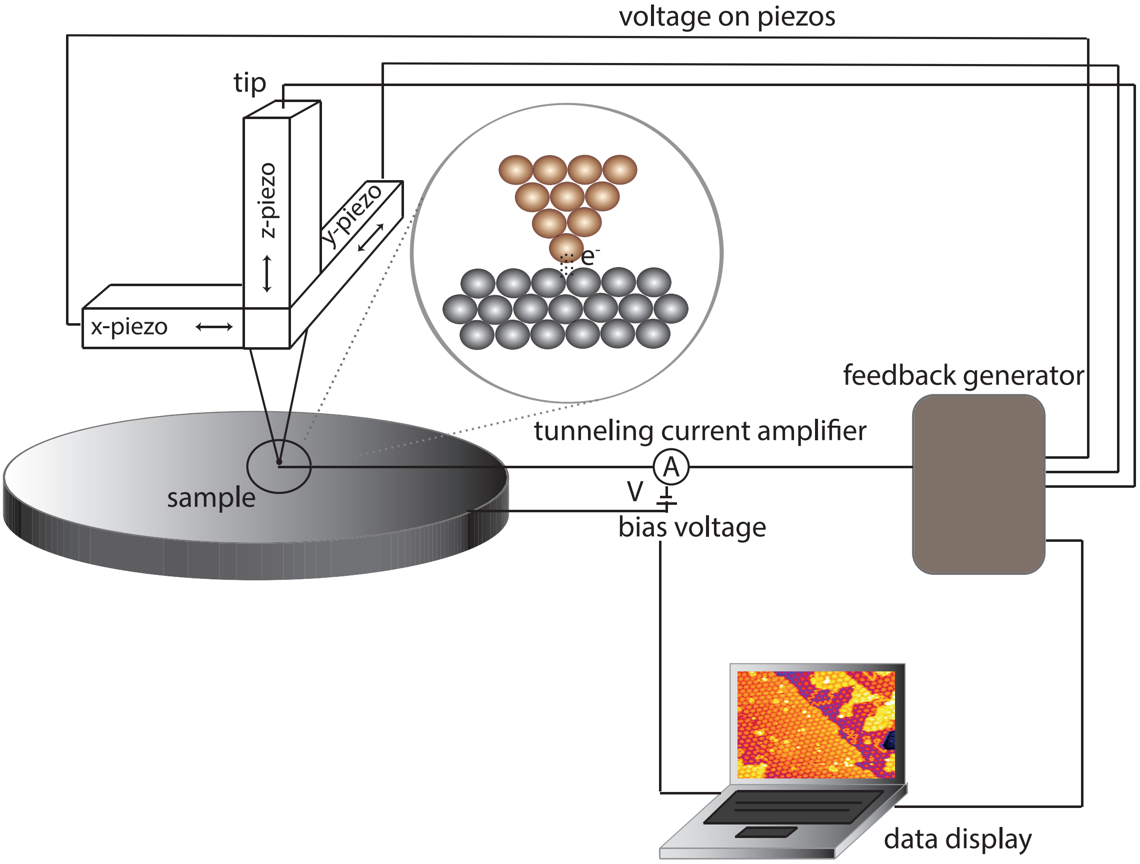

Figure 6.17: Schematic drawing of a STM setup. When a bias voltage is applied to the sample the electrons can travel between the sample and the tip giving rise to a current which depends on the separation between the sample and the tip. If the current is kept fixed a topographic image of the surface may be obtained.

elements and a topography of the surface electron density is obtained by plotting the z-piezo voltage versus the lateral tip position. In the constant height mode, the distance between the tip and the sample is held constant while the current is adjusted all the time to maintain the distance. A topographic image is obtained by plotting the tunneling current as a function of lateral tip position on the surface. As this mode of operation has an increased risk of crashing the tip into the surface, it is mostly used for atomically flat surfaces.

The resolution of a recorded STM image is strongly dependent on the shape of the tip; atomic resolution is more likely when a single atom of the tip is closer to the sample than all other tip atoms. STM has an important limitation: as the operation requires a current between the tip to the sample or vice versa, a conducting sample is needed. Insulating samples, like oxides, which are important for catalysis, can therefore not be investigated using STM. Often this problem can be circumvented to some extent by using thin oxide films grown on metallic substrates. This has been done in the present work, where a thin alumina film was grown on NiAl(110), and examples of STM images from this system are shown in Fig. 6.18. Because the oxides have a wide band gap, high voltages are required to image the oxide film,

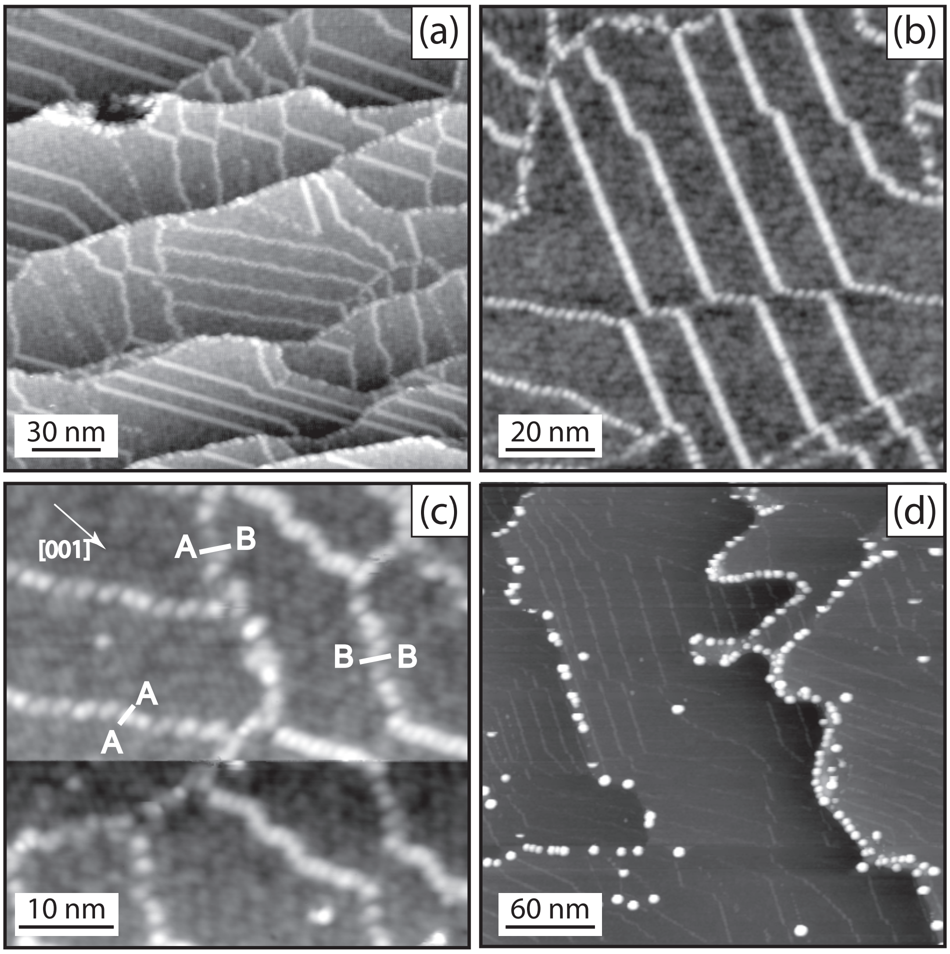

Figure 6.18: The morphology of the ultrathin aluminum oxide film grown on NiAl(110) imaged with positive bias voltage. (a) Large scale image showing the film morphology ($200 \times 200\ nm^2$) (3 V, 0.2 nA); Close-up images of the line defect structure ($100 \times 100\ nm^2$) (3 V, 0.4 nA)(b), ($50 \times 50\ nm^2$) (2.7 V, 0.4 nA) (c). The domain boundaries are clearly visible: 1. Antiphase domain boundaries: within a given reflection domain (A-A; B-B); 2. Reflection domain boundaries: boundaries between domains of type A and B [180]. (d) Ag deposited on the aluminum oxide film (30 sec) ($300 \times 300\ nm^2$) (1.8 V, 0.045 nA). The clusters nucleate at the step edges and domain boundaries.

while for the metallic substrate, lower voltages are used for imaging. At low bias voltages the electronic states of the oxide are not accessible, the electrons can only tunnel between tip and the metal support. If high enough bias voltage is used, the electrons can tunnel directly into or out of the oxide states.

The interpretation of STM images is not always straightforward. Often, theoretical simulations are important for a correct interpretation of the experimental images. Below I will briefly summarized some formulas that may be used for the calculation of the tunneling current.

6.6.1 STM theory

The Tersoff-Hamann theory provides a quantitative theory of the tunneling current in STM [181]. The tunneling current between the tip and the sample is written as:

$$I = \frac{2\pi e}{\hbar} \sum_{ts} f(E_t)[1 - f(E_s + eV)] \times |M_{ts}|^2 \delta(E_t - E_s), \tag{6.18}$$

where the s and t indices refers to the surface and tip, respectively, $f(E)$ is the Fermi function, V is the applied voltage, M_{ts} is the tunneling matrix element between states ψ_t of the probe and ψ_s of the surface, and E_t is the energy of the state ψ_t in the absence of tunneling. In the case of metals, the experiments are usually performed at RT or below and at low voltages (about 10 meV). In the limit of small voltages and temperature only the states at the Fermi level (E_F) contribute to the tunneling current:

$$I = \frac{2\pi}{\hbar} e^2 V \sum_{ts} |M_{ts}|^2 \delta(E_s - E_F)\delta(E_t - E_F), \tag{6.19}$$

The Matrix element was calculated by Bardeen and is expressed as a integral over any surface S lying within the vacuum region between the sample and the tip [182] :

$$M_{ts} = \frac{-\hbar^2}{2m} \int d\mathbf{S} \cdot (\psi_t^* \nabla \psi_s - \psi_s \nabla \psi_t^*), \tag{6.20}$$

where ψ_t and ψ_s are wave functions of the tip and sample in the case of no interaction between the two subsystems. In order to be able to calculate the tunneling current the wave functions of both the tip and the sample shall be known, which is not a straightforward task since the atomic structure of the tip is not usually known. Therefore some assumptions have to be made.

In 1983, Tersoff and Hamann [181] evaluated the matrix elements by modeling the electronic wave functions of the tip by spherical s-type wave functions with a curvature radius $\mathbf{r}_0$. M was found as:

$$M \propto \psi_s(\mathbf{r}_0) \tag{6.21}$$

With this the tunneling current was found to be given by the local DOS (LDOS) of the sample at the Fermi level:

$$I \propto |\psi_s(\mathbf{r}_0)|^2 \delta(E_s - E_F) = \rho(\mathbf{r}_0, E_F), \tag{6.22}$$

where $\rho(\mathbf{r}_0, E_F)$ is the local density of sample states at the center of the tip and at the Fermi level. It has been proved that the s-type tip approximation provides reliable simulation of STM images in most of the cases.

6.7 Theoretical Methods

6.7.1 Density functional theory calculations

Density Functional Theory (DFT) is a widely spread theoretical tool for structure determination due to its good accuracy for many systems [183]. It has successfully been applied to different scientific areas such as catalysis, nanomaterials, and biomaterials [184]. DFT has been used to simulate many of the experimental results in this thesis. As I have not participated in performing the simulations, I will only give a very brief introduction to DFT. For further reading I refer the interested reader to references [183, 185, 186].

DFT is a theoretical technique used to investigate the electronic structure of many-body systems consisting of interacting electrons and nuclei. As the Hamiltonian contains information about the fundamental interactions present in a system under study, all physical and chemical properties of a system can be derived from the Hamiltonian. Therefore quantum mechanics plays an important role in DFT. The main idea beyond the DFT is to solve the Schrödinger equation of a many-body system:

$$H\Psi = E\Psi \tag{6.23}$$

where H is the Hamiltonian, Ψ the many-body wavefunction and E the total energy of the system.

However, because of the high number of particles, it becomes practically impossible to find the exact solutions to the Schrödinger equation and some approximations have to be done. One approximation is to consider the nuclei as fixed and only the electrons moving, the Born-Oppenheimer approximation. The total wavefunction is then separated in an electronic and a nuclear part and the Schrödinger equation can be written as:

$$H_e \Psi_e(r_i) = E_e \Psi_e(r_i) \tag{6.24}$$

with H_e=T_e+ V_{e-e}+ V_{ext}, where T_e is the kinetic energy term, V_{e-e} is the electron-electron repulsion potential and V_{ext} is an external potential experienced by the electrons due to the nuclei [185]. This is still a many-body system.

In 1964 Hohenberg and Kohn offered a solution turning the problem into a single particle problem by the so-called Hohenberg- Kohn theorems [187]. They showed that the electronic structure of a system of interacting electrons in the ground state are determined by the electronic charge density. When the ground state charge density is known the ground state energy can also be determined. Therefore in order to calculate the ground state properties of the system, the many-body electron wave function is replaced by the electron charge density. Later, Kohn and Sham showed how DFT can be applied to total energy calculations considering a non-interacting system in an external potential [188]. The total energy of a system can then be expressed as a functional of the electron density. Since the electron density of a system can be computed far more easily than the many electron wave function, DFT made total energy calculations of larger systems computationally feasible.

Photoemission Core-Level Shifts

In this thesis DFT has be used to determine stable geometries and to calculate the binding energy shifts in XP spectra. The core-level shifts are usually calculated with respect to a reference, usually a bulk atom, and are defined as the difference between the binding energy of a core-level electron in a surface atom and one in the bulk:

$$\Delta_{cls} = E_{surf} - E_{bulk} \tag{6.25}$$

where E$_{bulk}$ and E$_{surf}$ are the binding energies of two different systems with a core hole in the bulk or a surface atom. As described in section (6.3.2), it is important to include the final state when calculating core-level shifts. The final state contribution to the core-level shift originates from the different response of the bulk and surface electrons to the creation of a core hole. All calculated core-level shifts in this thesis include the final state effects.

6.7.2 *Ab initio* Thermodynamics

Ab initio Thermodynamics is a theoretical approach which extends the DFT calculations (T= 0 K, no gas pressure) to ambient conditions [189, 190, 191]. The general idea behind it is the combination of thermodynamics and DFT to calculate the equilibrium geometry of a surface structure in contact with a given environment under conditions of defined temperature (T) and pressure (P) [192]. The most stable surface structure will be the one that has the lowest surface free energy, γ, under the given (T, P) conditions. This is achieved by changing the number of atoms of the reference gas until the lowest surface free energy is obtained. Therefore when the number of particles of a given system changes, the chemical potential (μ) needs to be taken into account. The surface free energy will be given by:

$$\gamma(T, p_i) = \frac{1}{A}\left[G(T, p_i) - \sum_i \mu_i(T, p_i) N_i\right], \tag{6.26}$$

where G is the Gibbs free energy of the crystal, A is the surface area and μ_i, N_i are the chemical potential and the number of the species of the same type. The Gibbs free energy is defined as: $G = U + pV - TS$, where U is the internal energy, V the volume, and S the entropy of the system. Thus the surface free energy is a function of the chemical potentials of all species in the system. An approximation used in *ab initio* thermodynamics to obtain the lowest surface free energy is that the Gibbs free energy is equal to the ground state total energy of the system, which can be obtained from DFT. For a given coverage, the structure of the most stable geometry is usually chosen from a number of trial geometries.

The chemical potential of a particular molecule i represents the change in free energy as the number of particles of that type changes by one and is given by:

$$\mu_i(T,P) = E_i + \mu_i^o + k_B T \ln \frac{P_i}{P^o}, \tag{6.27}$$

where E_i is the total energy of particle i, μ_i^o is a reference chemical potential taken from thermodynamic tables, k_B is the Boltzmann constant (=8.617×10^{-5} eV/K) and P^o is a reference pressure. From this relation it is observed that μ_i is negative ($P_i < P^o$) and, therefore, the lower μ_i is the highest the surface free energy will be. Increasing the pressure will result in a lower surface free energy. A similar effect of the chemical potential to the surface free energy can be obtained by decreasing the temperature. This means that in terms of thermodynamics the situation of low (T,P) is equivalent to high (T,P). But the kinetical barriers are significant at low temperatures and therefore the system observed in an experiment will not reach thermodynamical equilibrium, within a reasonable time.

An example of the application of *ab initio* thermodynamics to stability calculations of oxides is given in Paper II. Fig. 6.19 shows the phase diagram (surface free energy versus oxygen chemical potential) of the different oxygen-induced surface structures that were observed to form on Ag(111). At each particular value of the oxygen chemical potential the most stable phase is the one with the lowest surface free energy. For low values of oxygen chemical potential the clean surface was found to be the the most stable surface. As the oxygen pressure increase the chemical potential increases and the surface oxide is found to be more stable, while at even higher oxygen pressures the bulk oxide is more stable.

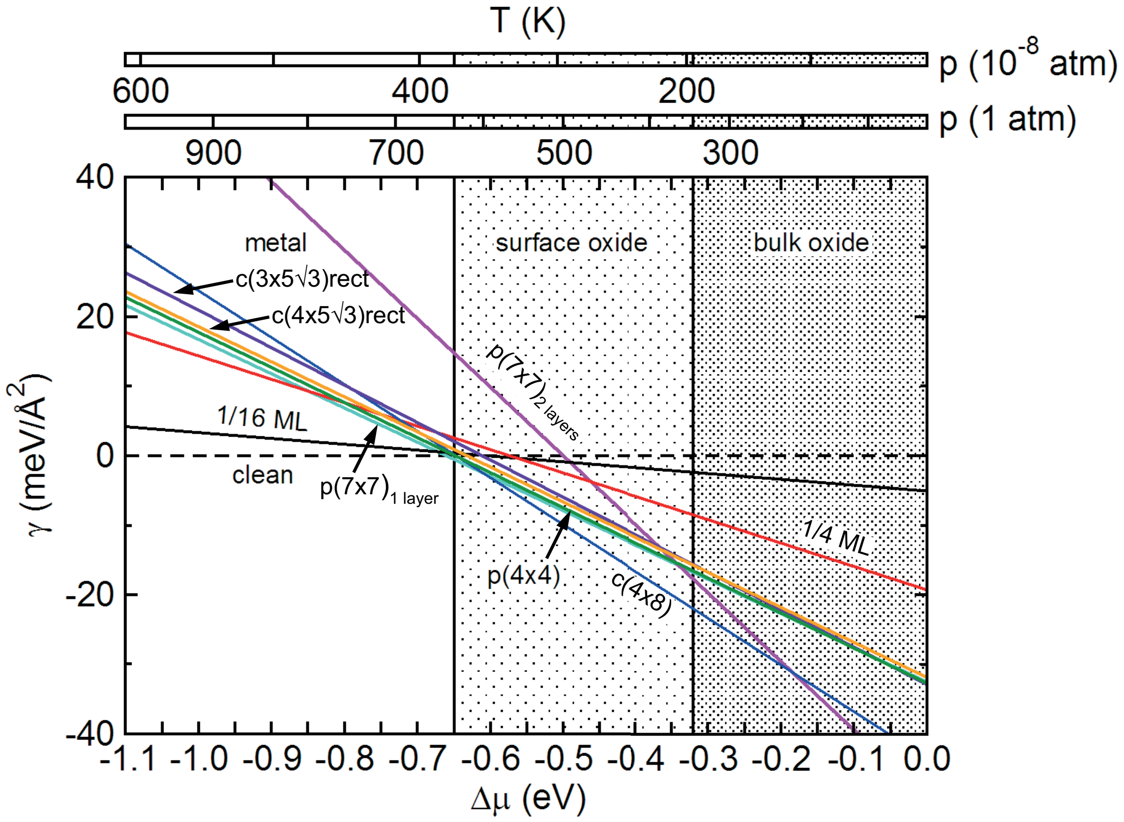

Figure 6.19: Surface free energies for different oxygen-induced surface structures on Ag(111) as a function of oxygen chemical potential. Adapted from Paper II.

7

Summary of Papers

This chapter summarizes the papers, which are included in the second part of this thesis.

7.1 Silver-alumina system

Paper I: High-resolution core-level spectroscopy study of the ultrathin aluminum oxide film on NiAl (110)

This paper reports on the electronic structure of the ultrathin aluminum oxide film grown on NiAl(110). The oxide film, generally known as Al_2O_3, has been extensively studied in the literature but its structure has only recently been solved [193], and so far no independent experimental study in the literature supports the proposed model, in its entire complexity. We have studied the oxide film by a combination of XPS and DFT. Previously recorded XPS spectra for ultrathin oxide films on NiAl alloys, both from the Al 2*p* as well as from the O1s have not been fully understood. Energy dependent core-level data from the O 1*s* and Al 2*p* levels allow for a distinction between oxygen and aluminum atoms residing at the surface or inside the aluminum oxide film. The calculated binding energies using the proposed model are in good agreement with our experimental findings. The XPS results support the model by Kresse *et al.* [193] and allow for a correct assignment of the different XP components to specific atomic sites. In particular, a shifted component in the O 1*s* spectrum, which has previously been assigned to all the surface oxygen atoms, can be assigned to surface oxygen atoms which do not reside very close to another oxygen atom corresponding to only 30% of the surface oxygen atoms.

Paper II: High-coverage oxygen-induced surface structures on Ag(111)

The article presents a combined XPS, STM and DFT study on the oxidation of Ag(111) with atomic oxygen, with a focus on the higher oxygen coverage structures. The results show the formation of more oxidized silver surfaces as compared to the $p(4 \times 4)$ phase for higher oxygen exposure, namely the $c(4 \times 8)$ structure and Ag_2O like phase with a (7×7) periodicity. Based on DFT calculations, a stable structure is proposed for the $c(4 \times 8)$ structure with a coverage of 0.5 ML. Above 0.5 ML coverage, bulk-like Ag_2O islands start to form on the Ag(111) surface. The different oxides ($p(4 \times 4)$, $c(4 \times 8)$ and 1-layer (7×7) structures) are found to co-exist on the surface with ratios depending on the amount of oxygen exposed to the surface.

Paper III: Mechanism for reversed photoemission core-level shifts of oxidized Ag

We have used a combination of DFT and XPS to investigate the origin of the negative shift of Ag 3*d* upon Ag oxidation. Comparative measurements and calculations are performed for Pd which shows normal positive shifts upon oxidation that can be explained by the electrostatic potential model. The calculations suggest that the core-level shifts for Pd can be related to initial-state effects, while the negative shifts for Ag should be related to final-state effects where the screening of the core hole takes place in bonding states of *s*-type.

Paper IV: Carbonate formation on p(4×4)-O/Ag(111)

In this paper we have studied the reaction of Ag(111) and Ag-O with CO at liquid nitrogen and RT conditions using a combination of XPS and DFT. Whereas CO does not adsorb on the Ag(111) surface at 100 K, our results reveals that CO adsorbs on the Ag(111)-$p(4 \times 4)$-O structure. In particular, the almost complete removal of the clean Ag(111)-$p(4 \times 4)$-O O 1*s* component indicates the formation of carbonate species on the surface. At 450 K the complete removal of the C 1*s* component indicates carbonate decomposition. Carbonate leaves the surface as CO_2(g) and the remaining O atoms form the silver oxide.

Paper V: Facile NO_x interconversion over preoxidized Ag(111)

In this paper the NO adsorption over oxidized Ag was investigated using a combination of XPS and DFT. The measurements show that NO adsorption over Ag(111)-$p(4 \times 4)$-O at low temperature results in NO dimerization, while at RT nitrate (NO_3) formation was observed. By increasing the NO pressure a complex interconversion between the adsorbed NO_x species was observed in the experimental data and was explained by partial decomposition of nitrates to nitrites and physisorbed NO in N_2O_3 structures.

Paper VI: Toward a silver-alumina model system for NO_x reduction catalysis

In this work we have tried to increase the understanding of the silver-alumina catalyst using a well defined model system, consisting of a NiAl(110) surface covered with a thin, well-ordered Al_2O_3 film on which Ag is deposited. STM and HRCLS were used to characterize the system. The STM images show that the Ag clusters nucleate and grow at the step edges and at domain boundaries on the substrate. The growth mode of Ag on clean NiAl(110) is completely different (Frank-van der Merwe growth, i.e. layer-by-layer growth): the Ag wets the surface and forms 2D islands and no shift of the Ag 3*d* as a function of coverage is observed.

The NO adsorption on Ag deposited on alumina was investigated at 100 K and the results show that NO dissociates in the presence of the Ag particles.

7.2 Pd and PdO(101)

Paper VII: Dissociative adsorption of hydrogen on PdO(101) studied by HRCLS and DFT

In this study we have investigated the adsorption of hydrogen on a PdO(101) film grown on Pd(111) in UHV at both 100 K and RT conditions by a combination of XPS and DFT. Our measurements provide resolution to separate between the 3- or 4-fold coordinated Pd atoms at the surface of the PdO(101) resulting in a fingerprint for the undercoordinated Pd atoms. Changes in the O 1*s* and Pd 3*d* spectra observed upon dosing 10 L of hydrogen reveal that hydrogen adsorbs dissociatively on PdO(101) at 110 K. The calculated core-level shifts for the dissociation of hydrogen on PdO(101) and formation of Pd-H and O-H groups supports this interpretation. Dosing 1×10^{-8} mbar hydrogen at 300 K on the PdO(101) results in extensive reduction of the oxide. The DFT calculations suggest a possible mechanism together with activation energies for the formation and desorption of water. The information reported in our study may be useful for understanding the dehydrogenation of hydrocarbons and other organic molecules over Pd.

Paper VIII: Oxidation and reduction of Pd(100) and aerosol-deposited Pd nanoparticles

HP-XPS was used to study the *in situ* oxidation and reduction with CO of Pd(100) and Pd nanoparticles on SiO_x. The results show similar results for the single crystal and the nanoparticles during oxidation with the formation of a surface oxide prior to bulk PdO. A lower temperature for PdO formation was observed for the the nanoparticles as compared to the single crystal. During the CO reduction, the bulk oxide was slowly reduced and a CO induced component was observed from the PdO surface suggesting that the bulk oxide exposes the (101) orientation. After oxide reduction the Pd(100) was found in a metallic phase with CO on the surface while carbon have incorporated into nanoparticles and formed a palladium carbide (PdC_x).

Paper IX: CO adsorption on clean and oxidized Pd(111)

In this study we have investigated the interaction of CO with clean as well as oxidized Pd(111) surfaces at 100 K using a combination of XPS, Infrared Spectroscopy and DFT calculations. The measurements show that CO adsorbs on all structures but has different coverages for the same CO exposures. In good agreement with previous studies, a $c(4\times2)$ structure was found to form upon CO adsorption on Pd(111) to a coverage of 0.5 ML. Upon exposing the Pd_5O_4 and PdO(101) surfaces to the same amount of CO, the binding energy of C 1*s* was found to be sensitive to the oxidation state of the surface and a shift of 0.3 eV and 2 eV was measured for the Pd_5O_4 and PdO(101) surface, respectively. The present study shows that the adsorption sites occupied by CO on the different surfaces change from the hollow and bridge sites on clean Pd(111) to bridge and atop sites on the oxidized Pd surfaces. Moreover, the CO coverage is found to decrease with increased oxidation state of Pd.

Paper X: Effects of non-local exchange on core-level shifts for gas-phase and adsorbed molecules

In this report we have investigated the large core-level shifts observed upon bulk oxidation of Pd (Pd 3*d* shift) and CO adsorption on PdO(101) (both the C 1*s* and O 1*s* shifts) which previously could not be explained by DFT. The results show that the comparison between experiments and calculation for the large shift in the Pd 3*d* binding energy for PdO(101) and the large shift in C 1*s* between CO/Pd(111) and CO/PdO(101) is improved when a hybrid functional (PBE0) is used instead of the PBE functional.

Paper XI: The active phase of Palladium during methane oxidation

We have studied the relation between surface structure and reactivity of Pd(100) for methane oxidation using a combination of SXRD, mass spectrometry and DFT. The results show an increased methane conversion as PdO(101) forms on the Pd(100). The calculations suggest that the oxygen undercoordinated Pd atoms at the surface of PdO(101) provide the lowest dissociation barrier for the extraction of the first hydrogen atom from methane that is also considered to be the rate determining step in the methane oxidation reaction.

Paper XII: Oxide thickness dependent ligand effect

The article presents a combined HP-XPS, mass spectrometry and DFT study of methane oxidation over Pd(100). The results show that although the resulting thin and thick PdO(101) oxide films expose the same surface atoms, their role as active sites during the reaction differs significantly due to differences in the layer below the top-most surface layer. The phenomenon can be explained by a ligand effect not previously reported to our knowledge for oxides, but similar to previously observed ligand effects in alloys. We argue that the observation may have implications on the atomistic design of new oxide based catalysts.

Paper XIII: *In situ* X-ray Photoelectron Spectroscopy of model catalysts: At the edge of the gap

The CO oxidation over Pd(100) was investigated by HP-XPS and first-principles Monte Carlo calculations. The results show an increased activity for CO oxidation in the near-ambient regime of the catalysts for both surface oxide and oxygen covered metallic surface without the presence of CO on the gas phase or on the surface due to the mass-transfer limitations. The calculations support the experimentally observed results.

8

Outlook

Silver-alumina is a catalyst, which is known to have high activities for the NO_x reduction, while Pd is a well known oxidation catalyst. In this work we have obtained a fundamental understanding of the Pd and Ag catalysts by studying the interaction of gas molecules such as O_2, CO, H_2, CH_4 and NO with the clean and oxidized Pd(100), Pd(111), Ag(111) and Ag nanoparticles on an oxidized NiAl(110) surface. Moreover, the CO and methane oxidation reactions over Pd were studied at high pressure conditions. For this purpose we have combined experimental techniques and theory and the results provide an understanding of the adsorption and reaction processes.

On the basis of the results presented several fundamental issues are clarified with respect to the Ag component and the reaction mechanism of silver-alumina system. The complexity of the model system were increased from single crystal surfaces to dispersed nanoparticles on a thin aluminum oxide support, bridging the materials gap. The NO_x reduction was not yet investigated in the present work but the results from Paper VI suggest that NO dissociates on Ag nanoparticles. Further work is needed to understand the complex reaction mechanism of NO_x reduction over silver-alumina. Additional experiments are necessary to investigate the role of hydrogen or water and Ag particles size effects in the silver-alumina system for the NO_x reduction. Since the Ag nanoparticles may expose different facets, the study of other low index surface orientations of Ag may be usefull to see the effects on reactivity towards NO_x reduction. As the $p(7 \times 7)$ was observed to form at higher oxygen coverages, it will be interesting to look into more detail into the structure of thicker films, at their interaction with gas molecules and how they might influence reactivity.

By combining traditional surface science techniques with novel *in situ* probes we have moved a step further towards real catalyst by bridging the pressure gap, especially in the second part of this work. Attempts have been made to bridge the materials gap and the results show similar behaviour for Pd nanoparticles and single crystal surfaces during the oxidation/reduction processes. Still more work is to be done to fully understand the oxidation reactions over Pd. As mentioned above the active metal nanoparticles may expose different facets and, therefore, it will be interesting to investigate the oxidation reactions (CO, methane) over different surface orientations of Pd, or even vicinal surfaces. More complex studies may be to investigate the effect of water and the influence of the support on the reactivity, or to look into the partial oxidation of methane.

9

Acknowledgements

In this last chapter I would like to show my appreciation to all these people who have contributed to this work, in one way or another. First of all, I would like to express my deep appreciation and gratitude to my supervisors Edvin Lundgren and Johan Gustafson. I am trully fortunate to have had the opportunity to work with you! Thank you Edvin for your patient guidance, encouragement and advice you have provided me during these years. I've been extremely lucky to have a supervisor who cared so much about my work and has also given me the freedom to take decisions by myself. Thank you for helping out with different problems and taking the time whenever there was something to discuss. I am specially grateful for giving me the opportunity to travel to various synchrotrons around the world and to meet and work with different scientists. Johan, thank you for all your help and advices during these years, especially for all your constructive comments during the writing of this thesis. I appreciate the time you have taken all the time when I needed some help. Thank you for being supportive, especially for the help with developing the XRD lab and I shall also thank you for a large part of the diffraction I know today.

Big thanks to the people in our group for many successful projects and help during various beamtimes: Sara, Chu Chu, Mikhail, Lindsay. Travelling abroad for conferences would not have been as fun without great companions. Thank you Sara, Elin, Maria, Lars Erik, Olesia, Shilpi, Tripta, Ashley for for some of the best trips I've ever been on!

I will also thank Jan Knudsen for teaching me how to use the STM and the help and advices especially during my first year as a PhD.

Then, I would like to thank the beamline scientists of the different beamlines I have worked on for their support: Karina Thånell (I311 MAX IV), Zhi Liu (9.3.2 ALS), Oliver Balmes (Id03 ESRF), for their support during beamtimes. I would also like to thank Andreas Stierle for nice scientific discussions and great beamtimes at ANKA.

I would also like to extend my thanks to the present and former members at the Division of Synchrotron Radiation Research for great discussions and for taking the time to help me when I needed. Patrik, thank you for always taking care of my travelling expenses and other financial issues.

Special thanks to all co-authors, without who much of the work would not have been possible.

I also express my gratitude to the people who were part of the FUNCAT program. All our meeting were very inspiring and helped direct much of my work.

During my years as a phD student I had collaborations with a number of people who I would like to acknowledge.
Many thanks to Henrik Grönbeck, Anders Hellman, Simon Klacar, Maxime van der Waals, Adriana Trinchero from Competence Centre for Catalysis and Department of Applied Physics at Chalmers for theoretical calculations and for great help with the articles. This was one of the most fruitful collaboration which is clearly reflected in the number of our joint articles!

Many thanks to Magnus Skoglundh, Per-Anders Carlsson and Hanna Härelind Ingelsten at Competence Centre for Catalysis, Chalmers, for some great discussions about catalysis and for giving me the opportunity to visit KCK and perform some measurements on real catalysts.

I will like to thank Jason F. Weaver at the University of Florida for giving me the opportunity to visit UF and introducing me to TPD. Many thanks for always being so open for discussions and your prompt responses. Thank you very much for the fruitful cooperation on the papers.

I would also like to thank Can Hakanoglu, Juhee Choi, Feng Zhang, Abbin Antony, William Cartas at University of Florida for great collaboration, for the help in the Lab and for showing me around in Gainesville during my stay there. You really made my visit to Florida memorable!

To finish the "professional" acknowledgements, I would like to acknowledge financial support from the Swedish Research Council, the Foundation for strategic research (SSF), the Knut and Alice Wallenberg Foundation and the Anna and Edwin Berger Foundation, which made possible the work presented in this thesis .

Lastly, I would also like to thank my family and friends who always supported me and incented me to strive towards my goal. German, you have been a special person during these years. Thank you for always being there when I needed. A special thanks to my parents for their love and continuing support since I have moved far from home. I would never be where I am today without you.

Bibliography

[1] A. T. Bell, Science **299**, 1688 (2003).

[2] M. Bowker, *The basis and applications of heterogeneous catalysis*, Oxford Univ. Press (1998).

[3] J. Hagen, *Industrial Catalysis: A Practical Approach*, Second Edition, WILEY-VCH Verlag GmbH & Co. KGaA, Weinheim ISBN: 3-527-31144-0 (2006).

[4] J. J. Berzelius, Jber. Chem. **15**, 237 (1835).

[5] W. Ostwald, Phys. Z. **3**, 313 (1902); Ann. Naturphil. **9**, 1 (1910).

[6] F. Haber, Z. Elektrochem. **16**, 244 (1910).

[7] D. P. Woodruff, T. A. Delchar, *Modern Techniques of Surface Science*, Cambridge, UK, Cambridge University Press (1994).

[8] The Nobel Prize in Chemistry 2007. /http://www.nobelprize.org; G. Ertl, *Reactions at surfaces: from atoms to complexity*, Nobel lecture (2007).

[9] G. C. Bond, *Heterogeneous Catalysis*, Second Edition, Oxford University Press (1987).

[10] I. Chorkendroff, J. W. Niemantsverdriet, *Concepts of Modern Catalysis and Kinetics*, Wiley-VCH Verlag GmbH & Co, Weinheim (2007).

[11] R. Burch, Catal. Rev. **46**, 271 (2005).

[12] A. E. Van Diepen, M. Makee, J. A. Moulijn, in: F. J. J. G. Jenssen, R. A. van Santen(Ed.), Environmental Catalysis, Imperial College Press, London, 257-291 (1999).

[13] C. Howitt, V. Pitchon, F. Garin, G. Maire, A. Frennet, J. M. Bastin, Stud. Surf. Sci. Catal., Elsevier, 149-161 (1995).

[14] T. Miyadera, Appl. Catal. B: Environ. **2**, 199 (1993).

[15] K. A. Bethke and H. H. Kung, J. Catal. **172**, 93 (1997).

[16] M. Sterrer, H.-J. Freund, Catal. Lett. **143**, 375 (2013).

[17] I. Langmuir, Trans. Faraday Soc. **17**, 607 (1922).

[18] S. H. Kahn, G. A. Somorjai, J. Catal. **34**, 294 (1974).

[19] D. W. Goodman, J. Catal. **216**, 213 (2003).

[20] D. W. Goodman, Surf. Rev. Lett. **2**, 9 (1995).

[21] G. Ertl, Surf. Sci. **299**, 742 (1994).

[22] D. W. Goodman, Surf. Sci. **299-300**, 837 (1994).

[23] F. Zaera, Prog. Surf. Sci. **69**, 1 (2001).

[24] H.-J. Freund, H. Kuhlenbeck, J. Libuda, G. Rupprechter, M. Maumer, H. Hamann, Top. Catal. **15**, 201 (2001).

[25] H. J. Freund, Surf. Sci. **500**, 271 (2002).

[26] B. E. Nieuwenhuys, Adv. Catal **44**, 259 (2000).

[27] J. -C. Bertolini, Catalysis Today **138**, 271 (2002).

[28] M. Bowker, Chem. Sov. Rev. **37**, 2204 (2008).

[29] S. H. Kahn, G. A. Somorjai, J. Catal. **34**, 294 (1974).

[30] P. L. J. Gunter, J. W. Niemantsverdriet, F. H. Ribeiro and G. A. Somorjai, Catal. Rev. - Sci. Eng. **39**, 77 (1997).

[31] G. Ertl in J. R. Anderson, M. Boudart (Eds.), *Catalysis, Science and Technology*, Vol. **4**, Springer, Berlin (1983).

[32] R. Burch, Catal. Rev. Sci.-Eng. **46**, 271 (2004).

[33] D. W. Goodman, R. D. Kelley, T. E. Madey, J. T. Yates, J. Catal **63**, 226 (1980).

[34] C. T. Campbell, M. T. Paffett, Surf. Sci. **139**, 396 (1984).

[35] H. Bluhm, K. Andersson, T. Araki, K. Benzerara, G. E. Brown, J. J. Dynes, S. Ghosal, M. K. Gilles, H.-Ch. Hansen, J. C. Hemminger, A. P. Hitchcock, G. Ketteler, A. L. D. Kilcoyne, E. Kneedler, J. R. Lawrence, G. G. Leppard, J. Majzlam, B. S. Mun, S. C. B. Myneni, A. Nilsson, H. Ogasawara, D. F. Ogletree, K. Pecher, M. Salmeron, D. K. Shuh, B. Tonner, T. Tyliszczak, T. Warwick, T. H. Yoon, J. Electron Spectrosc. Relat. Phenom. **150**, 86 (2006).

[36] D. F. Ogletree, H. Bluhm, G. Lebedev, C. S. Fadley, Z. Hussain, M. Salmeron, Rev. Sci. Instrum. **73**, 3872 (2002).

[37] P. B. Rasmussen, B. L. M. Hendriksen, H. Zeijlemaker, H. G. Ficke, J. W. M. Frenken, Rev. Sci. Instr.**69**, 3879 (1998).

[38] R. Feidenhans'l, Surf. Sci. Rep. **10**, 105 (1989).

[39] I. K. Robinson and D. J. Tweet, Rep. Prog. Phys. **55**, 599 (1992).

[40] M. Bäumer, H.-J. Freund, Prog. Surf. Sci. **61**, 127 (1999).

[41] H.-J. Freund *et al.*, J. Mol. Catal. **82**, 143 (1993).

[42] A. Winkler, H. Borchert, K. Al-Shamery, Surf. Sci. **600**, 3036 (2006).

[43] C. J. Weststrate, A. Resta, R. Westerström, E. Lundgren, A. Mikkelsen, J. N. Andersen, J. Phys. Chem. C **112**, 6900 (2008).

[44] M. Mavrikakis [Ed.], *Surface Science: The first 30 years*, North Holland, Amsterdam (1994).

[45] N. W. Ashcroft and N. D. Mermin, *Solid State Physics*, Saunders College, Philadelphia (1976).

[46] WebElements: the periodic table on the web homepage: http://www.webelements.com

[47] M. Hanseb, K. Anderko, *Constitution of binary alloys*, McGraw-Hill Book Company, New York (1958) .

[48] A. Stierle, C. Tieg, H. Dosch, V. Formoso, E. Lundgren, J. N. Andersen, L. Köhler, G. Kresse, Surf. Sci. **569**, 263 (2003).

[49] J. Gustafson, A. Mikkelsen, M. Borg, J. N. Andersen, E. Lundgren, K. Klein, W. Hofer, M. Schmid, P. Varga, L. Köhler, G. Kresse, N. Kasper, A. Stierle, and H. Dosch, Phys. Rev. B **71**, 115442 (2005).

[50] A. Stierle, R. Streitel, P. Nolte, A. Vlad, I. Costina, M. Marsman, G. Kresse, E. Lundgren, J. N. Andersen, R. Franchy, and H. Dosch. New J. Phys. **9**, 331 (2007).

[51] D. R. Lide [Ed.], H. P. R. Frederikse [Ed.], *CRC Handbook of Chemistry and Physics: A Ready-reference Book of Chemical and Physical Data*, CRC Press, 76th ed. (1995).

[52] I. Langmuir, J. Am. Chem. Soc. **38**, 1221 (1916).

[53] A. Bradshaw and N. Richardson, Pure & App. Chem. **68**, 457 (1996).

[54] E. A. Wood, J. App. Phys. **35**, 1306 (1964).

[55] A. M Bradshaw, F. M. Hoffmann, Surf. Sci. **72**, 513 (1978).

[56] K. Reuter, M. V. Ganduglia-Pirovano, C. Stampfl, M. Scheffler, Phys. Rev. B **65**, 165403 (2002)

[57] T. A. Nijhuis, M. Makkee, J. A. Moulijn, B. M. Weckhysen, Ind. Eng. Chem. Res. **45**, 3447 (2006).

[58] M.-L. Bocquet, P. Sautet, J. Cerda, C. I. Carlisle, M. J. Webb, D.A. King, J. Am. Chem. Soc. **125**, 3119 (2003).

[59] I. E. Wachs, R. J. Madix, Surf. Sci. **76**, 531 (1978).

[60] X. Bao, M. Mühler, T. Schedel-Niedrig, R. Schlögl, Phys. Rev. B **54**, 2249 (1996).

[61] R. Burch, J. P. Breen, F. C. Meunier, Appl. Catal. B-Environ. **39**, 283 (2002).

[62] S. Günther, A. Reichelt, J. Wintterlin, A. Barinov, T. O. Mentes, M.Á. Nino, A. Locatelli, A.I.P (2008).

[63] G. Rovida, F. Pratesi, M. Maglietta, and E. Ferroni, J. Vac. Sci Technol. **9**, 796 (1972).

[64] J. Schnadt, J. Knudsen, X. L. Hu, A. Michaelides, R. T. Vang, K. Reuter, Z. Li, E. Lægsgaard, M. Scheffler, F. Besenbacher, Phys. Rev. B **80**, 075424 (2009).

[65] C. T. Campbell, Surf. Sci. **157**, 43 (1985).

[66] C. I. Carlisle, T. Fujimoto, W. S. Sim, and D. A. King, Surf Sci. **470**, 15 (2000).

[67] G. Rovida, F. Pratesi, M. Maglietta, and E. Ferroni, Surf. Sci. **43**, 230 (1974).

[68] R. B. Grant and R. M. Lambert, Surf. Sci. **146**, 256 (1984).

[69] S. R. Bare, K. Griffiths, W. N. Lennard and H. T. Tang, Surf. Sci. **342**, 185 (1995).

[70] V. I. Bukhtiyarov, V. V. Kaichev and I. P. Prosvirin, J. Chem. Phys. **111**, 2169 (1999).

[71] A. Reicho, *Ambient Pressure Oxidation of Ag(111) Surfaces: An in-situ X-ray Study*, PhD thesis, Max- Planck- Institut für Metallforschung, Stuttgart (2008).

[72] M. Schmid, A. Reico, A. Stierle, I. Costina, J. Klikovits, P. Kostelnik, O. Dubay, G. Kresse, J. Gustafson, E. Lundgren, J. N. Andersen, H. Dosch, P. Varga, Phys. Rev. Lett. **96**, 146102 (2006).

[73] J. Schnadt, A. Michaelides, J. Knudsen, R. T. Vang, K. Reuter, E. Læsgaard, M. Scheffler, F. Besenbacher, Phys. Rev. Lett. **96**, 146101 (2006).

[74] A. Reicho, A. Stierle, I. Costina, H. Dosch, Surf. Sci. **601**, L19 (2007).

[75] J. Klikovits, E. Napetschnig, M. Schmid, N. Seriani, O. Dubay, G. Kresse, P. Varga, Phys. Rev. B, **76**, 0454051 (2007).

[76] R. Westerström, *et al.*, Surf. Sci. **602**, 2440 (2008).

[77] R. Westerström, *et al.*, Phys. Rev. B **80**, 125431 (2009).

[78] M. Todorova, *et al.*, Surf. Sci. **541**, 101 (2003).

[79] G. Zheng, E.I. Altman, Surf. Sci. **462**, 151 (2000).

[80] E. Lundgren, G. Kresse, C. Klein, M. Borg, J. N. Andersen, M. De Santis, Y. Gauthier, C. Konvicka, M. Schmid, P. Varga, Phys. Rev. Lett. **88**, 246103 (2002).

[81] J. F. Weaver, Chem. Rev., **113**, 4164 (2013).

[82] E. Lundgren *et al.*, Phys. Rev. Lett. **92**, 046101 (2004).

[83] A. Stierle *et al.*, J. Chem. Phys. **122**, 044706 (2005).

[84] H. Conrad, G. Ertl, J. Küppers, E. E. Latta, Surf. Sci. **65**, 245 (1977).

[85] D. Rogers, R. Shannon, J. Gillson, J. Solid State Chem. **3**, 314 (1971).

[86] J. Han, D. Y. Zemlyanov, F. H. Ribeiro, Surf. Sci. **600**, 2730 (2006).

[87] N. Seriani, J. Harl, F. Mittendorfer, G. Kresse, J. Chem. Phys. **131**, 054701 (2009).

[88] H. H. Kan, J. F. Weaver, Surf. Sci. **602**, L53 (2008).

[89] H. H. Kan, J. F. Weaver, Surf. Sci. **603**, 2671 (2009).

[90] R. Franchy, Surf. Sci. Rep. **38**, 195 (2000).

[91] J.A. Rodriguez, Surf. Sci. Rep. **24**, 223 (1991).

[92] I. V. Markov, *Crystal growth for beginners, fundamentals of nucleation, crystal growth and epitaxy*, World Scientific Publishing Co Pte. Ltd., Singapore (2003).

[93] L. Vitos, A. Ruban, H. Shriver, J. Kollar, Surf. Sci. **411**, 186 (1998).

[94] R. Masel, *Principles of Adsorption and Reaction on Solid Surfaces*, Wiley Series in Chemical Engineering (1996).

[95] J. E. Lenard-Jones, Trans. Faraday Soc. **28**, 333 (1932).

[96] H. Kayser, Wiederman's Ann. Phys. Chem. **14**, 450 (1881).

[97] M. Scheffler, C. Stampfl, *Theory of Adsorption on Metal Substartes*, Handbook of Surface Science, Vol. 2 (2000).

[98] A. Nilsson *et al.*, Catal. Lett. **100**, 111 (2005).

[99] H. Wise and J. Oudar, *Material Concepts in Surface Reactivity and Catalysis*, San Diego: Academic Press (1990).

[100] G. A. Somorjai, Y. Li, *Surface Chemistry and Catalysis*, John Wiley & Sons, Inc, Hoboken, New Jersey, 2nd Ed. (2010).

[101] P. W. Atkins, *Molecular Quantum Mechanics*, Oxford University Press, Oxford (1983).

[102] B. Hammer and J. K. Nørskov, Surf. Sci. **343**, 211 (1995).

[103] B. Hammer and J. K. Nørskov, Adv. Catal. **45**, 71 (2000).

[104] D. M. Newns, Phys. Rev. **178**, 1123 (1969).

[105] P. W. Anderson, Phys. Rev. **124**, 41 (1961).

[106] B. Hammer, J. K. Nørskov, Nature **376**, 238 (1995).

[107] B. Hammer, J. K. Nørskov, *Theory of adsorption and surface reactions*, in NATO ASI Series, **331**, 285 (1997).

[108] M. B. Lee *et al.*, J. Chem. Phys. **87**, 723 (1987).

[109] Y. Iwasawa *et al.*, Top. Curr. Chem **71**, 149 (1977).

[110] M. Gajdos, A. Eichler, J. Hafner, J. Phys.: Cond. Mat. **16**, 1141 (2005).

[111] D. F. Shriver, P. W. Atkins, C. H. Langford, *Inorganic Chemistry*, Second Edition, Oxford University Press, Oxford New York (1994).

[112] G. Blyholder, J. Vac. Scie. Technol. **11**, 865 (1975).

[113] M. F. H. van Tol, B. E. Nieuwenhuys, Appl. Surf. Sci. **67**, 188 (1993).

[114] J. Hall *et al.*, Chem. Phys. Lett. **216**, 413 (1993).

[115] P. D. Nolan, B. R. Lutz, P. L. Tanaka, J. E. Davis, and C. B. Mullins , J. Chem. Phys. **111**, 3696 (1999).

[116] M. Bowker, J. Phys. Condens. Matter **22**, 263002 (2010).

[117] T. Gray, *Gone in a Flash*, Popular Science **70** (2009).

[118] S. E. Boulfelfel, A. R. Oganov, S. Leoni, Sci. Rep. **2**, 1 (2012).

[119] I. Langmuir, J. Am. Chem. Soc. **40**, 1361 (1918).

[120] F. Zaera, Prog. Surf. Sci. **69**, 1 (2001).

[121] D. Eley and E. Rideal, Nature **146**, 401 (1946).

[122] E. Vesselli, M. Rizzi, L. De Rogatis, X. Ding, A. Baraldi, G. Comelli, L. Savio, L. Vattuone, M. Rocca, P. Fornasiero, A. Baldereschi and M. Peressi, J. Phys. Chem. Lett. **1**, 402 (2010).

[123] P. Mars and D. W. Van Krevelen, Chem. Eng. Sci. Spec. Suppl. **3**, 41 (1954).

[124] H. Over, Y. D. Kim, A. P. Seitsonen, S. Wendt, E. Lundgren, M. Schmid, P. Varga, A. Morgante, G. Ertl, Science **287**, 1474 (2000).

[125] J. T. Hirvi, T.-J. J. Kimunnen, M. Suvanto, T. A. Pakkanen, J. K. Nørskov, J. Chem. Phys. **133**, 084704 (2010).

[126] M. P. Seah and W. A. Dench, *Quantitative Electron Spectroscopy of Surfaces: A Standard Data Base for Electron Inelastic Mean Free Paths in Solids*, Surf. Inter. Anal., 12 (1979).

[127] G. A. Somorjai, *Chemistry in Two Dimensions*, Surfaces, Cornell University Press, Ithaca (1981).

[128] D. H. Tomboulian, P. L. Hartmann, Phys. Rev. **102**, 1423 (1956).

[129] H. Hertz, Ann. Phys. Chem. **36** (1889).

[130] A. Einstein, Ann. Phys. **17**, 132 (1905).

[131] The Nobel Prize in Physics 1981, http://www.nobelprize.org, K. Siegbahn, *Electron Spectroscopy for atoms, molecules and condensed matter*, Nobel lecture (1981).

[132] G. Attard, C. Barnes, *Surfaces*, Oxford University Press, pp 37-43 (2011).

[133] http://www.nottingham.ac.uk/ ppzjno/pes1.htm

[134] C. D. Wanger, W. M. Riggs, L. E. Davis, J. F. Moulder and G. E.Muilenberg, *Handbook of X-ray Photoelectron Spectroscopy*, Perkin-Elmer Corp., Physical Electronics Division, Eden Prairie, Minnesota, USA (1979).

[135] N. Mårtensson, P. Baltzer, P. A. Brühwiler, J. O. Forsell, A. Nilsson, A. Stenborg, B. Wanneberg, J. Electron. Spectrosc. Relat. Phenom. **70**, 117 (1994).

[136] H. Bubert, H. Jenett, *Surface and Thin Film Analysis: Principles, Instrumentation, Applications*, Wiley-VCH, Weinheim- Germany (2002).

[137] D. Roy and D. Tremblay, Rep. Prog. Phys. **53**, 1621 (1990).

[138] A. Stenborg, J. N. Andersen, O. Björneholm, A. Nilsson, N. Mårtensson, J. Electron. Spectrosc. Relat. Phenom. **52**, 47 (1990).

[139] M. Hollas, *Modern Spectroscopy*, Forth Edition, John Wiley & Sons, Chichester (2004).

[140] S. Hufner, *Photoelectron Spectroscopy, Principles and Applications*, Springer-Verlag, Berlin-Heidelberg-New York, 3rd ed. (2003).

[141] S. Doniach and M. Šunijć, J. Phys. C. **3**, 285 (1970).

[142] www.sljus.lu.se

[143] W. F. Egelhoff, Surf. Sci. Rep. **6**, 253 (1986).

[144] D. A. Shirley, Phys. Rev. B **5**, 4709 (1972).

[145] S. Tougaard, SIA **25**, 137 (1997).

[146] K. Siegbahn, C. Nordling, A. Fahlman, R. Nordberg, K. Hamrin, J. Hedman, G. Johansson, T. Bergmark, S. E. Karlsson, J. Lindgren, B. Lindberg, Nova Acta Regiae Soc. Sci. Ups. **4**, 20 (1967).

[147] M. Scheffler, A. M. Bradshaw in *Chemical Physics of Solid Surfaces and Heterogeneous Catalysis*, ed. by D. A. King and D. P. Woodruff, Elsevier, Amsterdam (1983).

[148] J. N. Andersen, D. Hennig, E. Lundgren, M. Metghfessel, R. Nyholm, M. Scheffler, Phys. Rev. B **50**, 23 (1994).

[149] Elettra Synchrotron Light Laboratory in Trieste, Italy. Available at: http://ulisse.elettra.trieste.it

[150] J. J. Yeh and I. Lindau, *Atomic Data and Nuclear Data Tables* **32**, 1 (1985).

[151] A. Beutler, *Adsorption of Molecules on Metal Surfaces Studied by High Resolution Core Level Photoemission*, PhD thesis, Lund University (1998).

[152] M. Smedh, *Molecular overlayers on homogeneous and heterogeneous metal surfaces studied by core-level photoemission*, PhD thesis, Lund University (2001).

[153] C. S. Fadley, Synchrotron Radiation Research, **1**, 421 (1992).

[154] A. Beutler, E. Lundgren, R. Nyholm, J. N. Andersen, B. Setlik, D. Heskett, Surf. Sci. **396**, 117 (1998).

[155] http://www.maxlab.lu.se

[156] https://www.maxlab.lu.se/maxiv

[157] R. Nyholm, J. N. Andersen, U. Johansson, B. N. Jensen, I. Lindau, Nuclear Instruments and Methods in Physics Research A **467**, 520 (2001).

[158] https://www.maxlab.lu.se/node/787

[159] K. Siegbahn, C. Nordling, G. Johansson, J. Hedman, P. F. Heden, K. Hamrin, U. Gelius, T. Bergmark, L. O. Werme, R. Manne, Y. Baer, *ESCA Applied to Free Molecules*, North-Holland Publishing Company, Amsterdam (1969).

[160] R. E. Ballard, S. L. Barker, G. G. Gunnell, W. H. Hagan, S. J. Pearce, R. H. West, J. Electron Spectrosc. Rel. Phenom. **14**, 331 (1978).

[161] L. Nemec, H. J. Gaehrs, L. Chia, P. Delahay, J. Chem. Phys. **66**, 4450 (1977).

[162] R. W. Joyner, M. W. Roberts, K. Yates, Surf. Sci. **87**, 501 (1979).

[163] H. J. Ruppender, M. Grunze, C. W. Kong, M. Wilmers, Surf. Interface Anal. **15**, 245 (1990).

[164] D. F. Ogletree *et al.*, Nucl. Instrum. Meth. Phys. Res. A **601** 151 (2009).

[165] http://www-als.lbl.gov/index.php/contact/123-932.html

[166] D. E. Sands, *Introduction to crystallography*, Dover Publications, INC, New York (1993).

[167] A. Guinier, *X-ray Diffraction in crystals, Imperfect crystals and amorphous bodies*, Dover Publications, INC, New York (1994).

[168] B. E. Warren, *X-ray Diffraction*, Dover Publications, Inc., New York (1990).

[169] R. L. Johnson, Advances in Solid State Physics, **31**, 115 (1991).

[170] I. K Robinson, Phys. Rev. B. **33**, 3830 (1986).

[171] C. Davisson and L. H. Germer, Phys. Rev **30**, 705 (1927).

[172] J. Gustafson, M. Shipilin, C. Zhang, A. Stierle, U. Hejral, U. Ruett, O. Gutowski, P.-A. Carlsson, M. Skoglundh, E. Lundgren, Science, in press (2014).

[173] E. Vileg, J. Appl. Crystallogr. **33**, 401 (2000).

[174] http://www.esrf.eu

[175] S. Ferrer, F. Comin, Rev. Sci. Instrum. **66**, 1674 (1995).

[176] O. Balmes *et al.*, Catalysis Today **145**, 220 (2009).

[177] G. Binning, H. Rohrer, IBM J. of Research and Development **30**, 355 (1986).

[178] R. Wiesendager, *Scanning Probe Microscopy and Spectroscopy*, Cambridge University Press, Cambridge (1994).

[179] G. Binning, H. Rohrer, Ch. Gerber, E. Weibel, Phys. Rev. Lett. **49**, 57 (1982).

[180] J. Libuda, F. Winkelmann, M. Bäumer, H.-J. Freund, T. Bertams, H. Neddermeyer, and K. Muller, Surf. Sci. **318**, 61 (1994).

[181] J. Tersoff and D. R. Hamann, Phys. Rev. Lett. **50**, 1998 (1983).

[182] J. Bardeen, Phys. Rev. Lett. **6**, 57 (1961).

[183] N. Argaman and G. Makov, Am. J. Phys. **68**, 69 (2000).

[184] J. Hafner, C. Wolverton, G. Ceder, MRS Bulletin **31**, 659 (2006).

[185] A. Groβ, *Theoretical Surface Science*, Springer- Verlag Berlin Heidelberg (2003).

[186] H. Eschrig, *The Fundamentals of Density Functional Theory*, Edition am Gutenbergplatz (2003).

[187] P. Hohenberg, W. Kohn, Phys. Rev. **136**, 864 (1964).

[188] W. Kohn, L. J. Sham, Phys. Rev. **140**, A1133 (1965).

[189] K. Reuter, M. Scheffler, Phys. Rev. B **65**, 035406 (2002).

[190] K. Reuter, M. Scheffler, Phys. Rev. Lett. **90**, 046103 (2003).

[191] J. Rogal, K. Reuter, Educational Notes RTO-EN-AVT-142, Neuilly-sur-Seine, 2-1 (2007).

[192] K. Reuter, M. Scheffler, Phys. Rev. B **65**, 035406 (2001).

[193] G. Kresse, M. Schmid, E. Napetschnig, M. Shishkin, L. Köhler, P. Varga, Science **308**, 1440 (2005).